CHAPTER 3

EXPERIMENTAL EQUIPMENT AND LAYOUT

3.1 General Layout of Testing Equipment

3.1.1 Introduction

From an experimental point of view, the mechanical behaviour of unsaturated soils under isothermal conditions (ambient temperature) is relatively well known, but little has been studied concerning joined effects of unsaturation and temperature changes. There are a number of experimental studies concerning thermal effects on saturated soils, for instance Paaswell (1967), Campanella and Mitchell (1968), Plum and Esrig (1969), Sherif *et al.* (1982), Demars and Charles (1982), Zeuch (1983), Burghignoli and Paoliani (1985), Houston *et al.* (1985), Naik (1986), Agar *et al.* (1986), Agar *et al.* (1987), Horseman *et al.* (1987); and more recently, Baldi *et al.* (1988), Eriksson (1989), Tidfors and Sällfors (1989), Hueckel and Baldi (1990), Hueckel and Pellegrini (1991), Miliziano (1992), Burghignoli *et al.* (1992), De Bruyn and Thimus (1993, 1995, 1996), Lingnau (1993), Lingnau *et al.* (1993, 1995, 1996), Towhata *et al.* (1993), Boudali *et al.* (1994), Bergenstahl *et al.* (1994), Towhata and Kuntiwattanakul (1994), Jefferson (1994), Kuntiwattanakul *et al.* (1995), Akagi and Komiya (1995), Moritz (1995), Tanaka *et al.* (1995, 1997), Belanteur *et al.* (1997), Robinet *et al.* (1997), Komine and Ogata (1998) and Sultan *et al.* (1998). In contrast, the information available on thermal behaviour of unsaturated soils is very limited. To the author's knowledge, the only reported tests with simultaneous control of suction and temperature in an oedometer cell were those presented by Romero *et al.* (1995) and Romero *et al.* (1998a), and in a thermal triaxial cell those reported by Saix and Jouanna (1990, 1995), Saix (1991) and Romero *et al.* (1998c). Also Recordon (1993), Recordon and Gueye (1994) and Bovet *et al.* (1995) performed unsaturated soil deformability tests at varying temperatures. Graham *et al.* (1995) and Wiebe *et al.* (1998) accomplished 'UUU' triaxial tests at different degrees of saturation and temperatures.

This research is mainly focused on the volumetric behaviour of unsaturated clays (swelling, collapse and shrinkage behaviour) under suction and temperature changes. In this way, suction and temperature controlled oedometer cells have been the most utilised equipment, due to the following advantages: accurate direct volume change determinations (volumetric strain resolution between 0.013% and 0.025%), and that testing paths follow a K_0 condition similar to the static compaction process used in the fabrication of the samples and thus minimising effects due to the anisotropic loading imposed to the specimen during this process. On the other hand, stress state information is usually incomplete, unless lateral stress equipment is used, which could not be adapted to apply temperature paths. In order to investigate the volumetric behaviour under isotropic conditions two different cells (mini isotropic cell and modified triaxial cell) were used. This equipment offers an unquestionable advantage in knowing the stress state of the sample. However, the volume change measurement is usually subjected to calibrations and indirect procedures that do not offer so good resolution and accuracy compared to oedometer equipment, specially in the mini isotropic cell where volumetric strain resolution increases up to a relatively high value. In addition, testing results with isotropic cells are more influenced by the distortion of the sample, mainly during the first wetting path, caused by the anisotropic loading condition imposed to the specimen during K_0 static compaction.

3.1.2 General layout of air and water pressure systems

3.1.2.1 Axis translation technique. Operational techniques

Axis translation or air overpressure technique has been used to impose different matric suction steps. The procedure used in this research involved a translation of the reference pore air pressure to a constant gauge

pressure u_a, which can be considered as an artificial increase in the atmospheric pressure under which the test is performed. Consequently, the negative pore water pressure is also increased by an equal amount to a positive water pressure u_w in order to maintain a constant matric suction (u_a-u_w)(axis translation technique for measuring pore-water pressure; Hilf, 1956). Water gauge pressures of u_w = 0.05, 0.20, 0.30, 0.44 and 0.49 MPa have been selected to impose the different suction steps under a constant value of air gauge pressure of u_a = 0.50 MPa. A HAEV ceramic disc with an air-entry value greater than that of the maximum applied matric suction of 0.45 MPa is used as an interface between the unsaturated soil and the pore water pressure system, acting as a link between the pore water in the soil and the water in the measuring system and avoiding the passage of free air into the water compartment. Because of the ability of a ceramic disc to withstand the flow of free air results from surface tension, which is temperature dependent, the air-entry value can be affected at higher temperatures. In this sense, periodically checks have been carried out at temperatures of 80°C in order to know the possibility of sustaining a maximum air overpressure of 0.45 MPa. The selection of the ceramic discs was based upon the maximum applied matric suction, as well as for its water permeability and thickness. This information is of importance for assessing the time for pore water equalisation. It is desirable to have the highest possible coefficient of permeability and the thinnest ceramic disc to reduce time required for equilibration throughout the specimen and minimise impeded drainage of pore water. However, the use of thin discs results in a greater accumulation of diffused air in the water compartment (refer to Eq. (3.16)). Conventional ceramic discs of 0.5 μm pore size, 0.55 MPa air-entry value at 22°C (estimated in a bubbling pressure of 0.48 MPa at 80°C) and with a thickness of (7.40±0.05) mm were used in the conventional / thermal oedometer and isotropic cells. Ceramic discs of 0.16 μm pore size, 1.52 MPa bubbling pressure at 22°C and around 1.30 MPa at 80°C and with a thickness of (7.30±0.10) mm were utilised in the triaxial and lateral stress cells. Rigid bronze coarse porous stones of 350-500 μm grain size and around 85 μm pore size have been used in the different equipment, giving an air-entry value of approximately 3.4 kPa. This way, no water is held in these coarse porous stones when applying a minimum air overpressure of 10 kPa. However, stainless steel coarse porous stones of 15 μm pore size with an air-entry value of approximately 19 kPa or corundum ones (25-50 μm particle size) were used in the thermal oedometer cells in order not to have electrolysis problems in long term tests with different metallic electrodes. The axis translation technique has recently been applied by different researchers to impose low suction levels Gan *et al.* (1988), Balmaceda (1991), Sivakumar (1993), Yuk Gehling (1994), as well as at relatively high values in the order of 7 MPa by Lagny (1996).

Theoretical studies of this technique concerning its application for measuring soil suction suggest that it is best suited for soils with a continuos air phase (Olson and Langfelder, 1965; Bocking and Fredlund, 1980). Air overpressure was applied to soil samples dry of optimum with an initial degree of saturation of $Sr_o \approx 44\%$ for the high-porosity packing and 69% for the high-density fabric, therefore being all the pore-air interconnected to the surface of the samples in order to induce an equal pore-air pressure value throughout the specimens (usually over Sr = 85% air permeability of Boom clay decreases sharply; Volckaert *et al.*, 1996a). This air pressure tends to isotropically compress soil particles and water; however, since both are essentially incompressible because there is not much occluded air in the pore fluid, air pressure increase will not significantly change the curvature of air-water menisci and consequently will not generate an appreciable change of the initial soil matric suction, which is estimated around 2 MPa. Therefore, after application of an air pressure of 0.50 MPa, water pressure will be initially maintained at an estimate value of –1.5 MPa (matric suction is assumed to remain constant) before connecting the water pressure system at a starting value of 0.05 MPa (matric suction change of around 1.55 MPa). Conscious of certain limitation of axis translation technique at high degrees of saturation in fine soils, a constant air pressure of 0.50 MPa has been maintained throughout the tests varying solely the confinement and water pressures. This way, the effects of air-water interface bridging macrovoid space between aggregates, as well as the pore fluid volume changes associated with occluded air bubbles are avoided, phenomena that can induce certain irreversible arrangements in the skeleton due to pore fluid compression during the applications of axes translations by manipulating pore air pressure. In addition, the maintenance of a standard procedure of suction application would facilitate test reproducibility with other equipment. Recently, Mongiovi and

Tarantino (1998) have developed an apparatus to investigate the validity of axis translation technique in unsaturated soils ($Sr \approx 56\%$) by preventing sample deformation and water content changes. When air pressure was modified no variation of matric suction was detected within experimental error, measuring negative pore water pressures with Imperial College tensiometers (Ridley and Burland, 1993).

Continuity between soil water and water in the ceramic disc is assumed to correctly impose matric suction. This way, a thin film of water is left over the top of the filter during the setting up process, preventing the possibility of its drying mainly in the setup operation at high temperatures, where the disc is exposed to the atmosphere with a relative humidity of around 50%. If the specimen at an initial estimated pore water pressure of -2 MPa at 22°C is placed over the saturated ceramic disc at atmospheric pressure it will immediately tend to draw water up through the ceramic disc. This direct contact between the sample and the filter can result in cavitation of the meta-stable water in a closed system, as it possibly occurs in the measuring system even if it is deaired (because air is entrapped in microscopic crevices) and then enters the porous disc replacing the water which is drawn into the sample. However, cavitation may also occur inside the porous stone, since it is difficult to eliminate the cavitation nuclei proposed in the crevice model (Marinho and Chandler, 1995). Therefore, it is recommended to apply high pressures of deaired water to the ceramic disc before opening the drainage lines as suggested in section 4.4.1, in order to dissolve air trapped in crevices. When the high water pressure is then released to atmospheric level the dissolved air comes out of solution, maintaining air-water interfaces inside the crevices and making it possible to resist higher tensile stress (Ridley and Wray, 1996). However, even if there is the possibility of delaying cavitation in the closed measuring system or in the porous stone, the system will fail when the air-entry value of the disc is surpassed, and air at atmospheric pressure will be drawn through the disc and bubbles will form in the closed reservoir. This mechanism has been investigated with different air-entry pressure ceramic discs during direct suction measurement by Ridley and Burland (1995). This tension breakdown can be more important at higher temperatures, due to the reduction of the bubbling pressure of the disc. In order to avoid this problem during the setting up period the fuse wire technique has been proposed (Davies, 1975; Maswoswe, 1985; Sivakumar, 1993). However, in this research low setting up periods and an open water system with a small water backpressure of 15 kPa in the measuring system (header tank pressure) were applied. Further aspects of setting up procedures, as well as an estimation of water volume flowing into the specimen during this period and its consequence on the initial conditions, are discussed in section 4.4.2.2.2.

It is important to flush air bubbles periodically from below the high entry disc, specially at high temperatures, to avoid slow growth cavitation of the system and the consequence loss of continuity between the pore water and the water in the measuring system. This cavitation can cause an erroneous estimation of the imposed matric suction, because water of the measuring system is initially forced into the soil causing lower suction values and then evaporated from the soil mass originating higher suction values and shrinkage of the specimen. A diffused air volume indicator was therefore incorporated in the open water pressure system to allow periodic flushing and measurements.

Wetting front advance in one direction during imbibition with a bottom HAEV ceramic and a upper coarse porous stone ensures that air is not trapped and the possibility of achieving high degrees of saturation at low suctions. However, in the case of the mini isotropic cell which is described in section 3.3.1, even though the wetting front advances toward the upper part of the sample, there is no free air connection through this upper part and thus air can be trapped. If there are two wetting fronts advancing, which is the case of the triaxial cell with two opposite combined ceramic discs and coarse porous stones described in section 3.3.2, then there is also the possibility of trapping air and the difficulty of achieving full saturation under nearly zero suction condition.

In order to accurately determine water volume changes it is necessary to account for water volume losses due to evaporation in the open-air pressure chamber, mainly at high temperature testing. Evaporative fluxes originated in the difference in vapour pressure between soil voids and the overlying air (open system) are detected in the water volume change devices under steady-state conditions.

Measured evaporative fluxes following similar criteria to the diffused air flows (refer to section 3.2.5.1) are compared in section 4.5.2 to model predictions prescribing a constant relative humidity at the soil surface and solving coupled heat and mass transfer equations for the soil profile. A special salt solution reservoir shown in Fig. 4.37 and connected to the air pressure line needs to be provided in the triaxial cell to humidify the dry air before connecting it to the air chamber and to limit water vapour transfer at temperatures higher than 50°C.

3.1.2.2 Diaphragm, piston and cell air pressure systems. Water pressure system

Air pressure for diaphragm, piston and cell pressures is applied by a compressed air system with air regulators. Maximum air pressure supplied by the high-pressure compressor is limited to 4.0 MPa, with a usual working range of (2.8±0.2) MPa. The low-pressure compressor connected to another independent supply line ensures a pressure of (0.94±0.06) MPa. For higher pressures, as well as for electrical power shut off, dry nitrogen bottles at 20 MPa giving a maximum working pressure of 5.0 MPa have been connected to the air pressure line. If pressures lower than 2.5 MPa are detected, which is the case of an electrical power failure affecting the compressors, then the check valve connected to the nitrogen line is activated. Pneumatic pressure regulators have been installed in the high-pressure line to provide a uniform input pressure to the air pressure regulators connected to the testing layout. Air filters and water traps are connected in lines with pressures up to 1.20 MPa and provisions for collection and removal of condensation by means of drainage valves at low points and upward tee connections to regulators have been incorporated when possible in the high pressure lines. Two types of regulators have been used depending on the supply pressure: Bellofram type 70 for a supply pressure up to 1.8 MPa (working range: 14 kPa to 1.1 MPa) and Fairchild model 10 for a maximum supply pressure of 3.5 MPa (working range: 14 kPa to 1.1 MPa and 35 kPa to 2.8 MPa). The combination of regulators with pressure transducers allows the control of pressures within a resolution of 1kPa. The effect of this resolution on net vertical stress sensitivity depends on the testing equipment. For the thermal cell, which is the most sensitive, the net vertical stress resolution is approximately 5 kPa; for the conventional suction controlled cell approximately 2 kPa and for the lateral stress cell 4 kPa. These calculations are based on the diaphragm and piston pressure calibrations presented in section 3.2.4.1. In this way, if a relative error of 10% is accepted for the net vertical stress, minimum recommended values are around 50 kPa for the thermal cell, 20 kPa for the conventional suction controlled cell and around 40 kPa for the lateral stress cell. Nevertheless, minimum applied net vertical stress during high temperature testing was 26 kPa for the high-density packing. In this case special care has been taken by means of periodic controls of the diaphragm and air pressures applied to the cells.

Initially deaired and demineralised water with a typical electrical conductivity of 10 μS/cm is used in the plumbing system and is provided from a header tank connected to a vacuum pump. The pressurised water is regulated by a self-compensating mercury pot system or by an air-water interface. The double mercury pot system connected in series and operated by a winch ensures a maximum working pressure of 1.0 MPa, with a typical resolution in combination with the pressure transducer of 1 kPa. The latex bladder type air-water interface, which minimises air dissolution, ensures a similar maximum working water pressure limited by the perspex interchange cylinders. Typical connections of air and water pressure systems to different equipment are schemed in Fig. 3.3.

Diaphragm type pressure transducers, with an operating range up to 2.0 MPa, were used to measure pore water and pore air pressures, as well as diaphragm or piston pressures. The transducers, issued with a calibration certificate from the manufacturers, were verified by comparison technique with another certified pressure gauge guaranteed to an accuracy of within 0.25% of the scale range (0-1 MPa) at any point of the scale. This reference gauge was also periodically checked on a dead-weight pressure gauge tester at specified points. Calibration cycles of increasing and decreasing pressures up to 0.85 MPa have been carried out. Non-linearity and hysteresis errors given by the manufacturer are within 0.05%FS, i.e. around 1 kPa. Non-linearity under monotonous increasing pressures according to the different calibration tests is around 0.09%FS and hysteresis in a cycle is less than 0.12%FS

(obviously these values are also affected by the non-linearity and hysteresis of the reference pressure gauge). Typical sensitivity is around 2 mV/V ± 3% (10.0±0.3 mV/MPa at an electrical excitation of 10 Vdc). In order to maintain a systematic measuring procedure only a reference transducer was used throughout the different oedometer testing.

3.2 Development of Suction Controlled Oedometer Cells

3.2.1 Conventional suction controlled oedometer cell

Conventional cells similar to those described in Balmaceda (1991) and Yuk Gehling (1994) have been used at ambient temperature to investigate swelling, collapse and shrinkage behaviour under constant net vertical stress, as well as loading and unloading behaviour under constant matric suction. The general description of the cell with respect to load and suction application is similar to what is detailed in the next section for the thermal cell. In following sections the characteristics of the loading cap with its calibration for diaphragm pressure, as well as the deformability of the equipment under loading paths, are presented in detail. Maximum pressure difference between the loading chamber and the pore air pressure applied in the 101-mm diameter chamber is restricted to 2.0 MPa, due to the limited stretchable capacity of the diaphragm within the fixing elements. For an air pressure of u_a = 0.50 MPa, this last condition gives a maximum net vertical stress of about $(\sigma_v - u_a) \approx 1.7$ MPa.

3.2.2 Suction and temperature controlled oedometer cell

3.2.2.1 Description of the oedometer cell and heating system

Two suction and temperature controlled oedometer cells have been designed and built in stainless steel (AISI 316) according to the diagram shown in Fig. 3.1 (Romero *et al.*, 1995) to perform suction and temperature controlled tests. The basic equipment is similar to the conventional oedometer cell with some differences related to the high temperature chamber and the loading platen geometry. In order to minimise effects of side friction and reduce equalisation times, while ensuring an adequate height for accurate strain measurements, a minimum height to diameter ratio of 10mm / 50mm has been selected. Axial strain is determined using a certified dial gauge (dial reading 0.010-10 mm, readability: 2.5 µm, volumetric strain resolution: 0.025%) registering top platen displacement. Pore air pressure is supplied to the upper coarse porous stone through a conduit in the loading cap and the water pressure system is connected to the lower HAEV ceramic disc. Vertical load is applied by means of pressurised air acting on a loading platen and separated by a 1-mm thick rubber membrane from the pore air pressure chamber. Loading system ensures that no tilting of the platen occurs on stress path testing. Maximum diaphragm pressure applied in the upper chamber (ϕ 169 mm) is restricted to 1.6 MPa due to the limited loading capacity of the 6 ϕ 6 mm stainless steel screws (AISI 304 with elastic limit 210 MPa), which connect the upper part with the cell body. This limiting pressure is equivalent to a net vertical stress of $(\sigma_v - u_a)$ = 2.5 MPa at u_a = 0.50 MPa. For higher diaphragm pressures up to 2.1 MPa a special device of approximately 100 N capacity is used to block the upper chamber. Net vertical stress pressure versus cell deformability calibrations presented in section 3.2.4.1 have been performed with the original layout. Maximum pressure difference between the loading chamber and the air pressure chamber is limited to 1.5 MPa, due to the stretchable capacity of the diaphragm within the fixing elements. Special o-rings made of Viton® (fluorocarbon elastomer) are utilised due to their high resistance to chemicals and compression set with temperatures up to 200°C.

Special care has been taken in the installation of the HAEV ceramic disc into the portable base plate. The disc (d = 53.0 mm, h = 7.4 mm) was properly sealed into the base pedestal (d = 56.0 mm) using a special epoxi resin along its periphery, previously cleaned with trichloroethylene for removal of grease from metal and the ceramic disc. This epoxi sealing is water resistant without ageing effects, as well as temperature resistant up to 120°C. The ceramic disc was installed and cured for 2 hours at 50°C to facilitate the elimination of trapped bubbles from the seal, so that at ambient temperature is prestressed.

The epoxi and the subsequent treatment ensure that no fine cracks will appear upon heating between the resin and the ceramic disc or the resin and the metal due to the different thermal properties. 3-mm grooves in the form of a spiral in the water compartment of the base plate serve as water channels for flushing air bubbles that may be trapped or have accumulated as a result of air diffusion (refer to section 3.2.5).

Temperature is imposed by means of a helical electric heater of 500 W at 220 V submerged in a silicone oil bath (viscosity of 10000 mm^2/s at 25°C and around 4000 mm^2/s at 80°C) that surrounds the oedometer cell. Silicone oil was chosen as cell fluid because of its low electrical conductivity and a high viscosity was preferred in order not to have toxic effects on the heated silicone (usually silicone oil of viscosity less than 100 mm^2/s appears to be toxic). The electric heater casing has an outer diameter of 8 mm and a length of 500 mm, forming a helix of an inner diameter of 110 mm and with a step of 10 mm between casings. Electrical power in the heater is controlled by applying different voltages with a selector switch (50 V, 75 V or 100 V) by means of a combination of transformers. In this way, power input varied between 25 W and 100 W, being this last value the one used at high temperatures. Electrical power is also automatically regulated by means of a programmable thermostat measuring and controlling the temperature inside the oedometer ring near the soil specimen (refer to Fig. 3.1) with type K thermocouples (Ni -10% Cr (+) vs. Ni - 5% Al and Si (-); temperature range: -200°C to 1370°C). An alarm from the thermostat with adjustable hysteresis to minimise inertial effects and acting over a relay output, connects or disconnects the electrical circuit between the transformer output and the resistance in order to maintain the specified temperature. A precision measuring temperature display and recorder connected to a data acquisition system and with a resolution of 0.1°C has also been used to register the temperature evolution of both the silicone oil bath and the oedometer ring during heating and cooling phases. The error limit of this type of thermocouples, which are the most common because of their wide measuring limits, is within ±2.2°C in the range of 0 to 200°C (ASTM STP 470B). However, in the temperature range of -60 to 100°C, less common type T thermocouples (Cu (+) versus CuNi (-); up to a limiting value of 370°C), are more suitable, presenting a lower error range of ±1.0°C (ASTM STP 470B). Thermocouples have been calibrated by comparison technique (further details of this technique are described in ASTM E220) with a fixed point equilibrium state (normal freezing point of water) and by immersing the thermocouple in water with a certified reference mercury thermometer (resolution 0.5°C). Errors of thermocouples detected by this technique are corrected in the different readout/controller units by the displacement of the zero point to an arbitrary base value or by scaling (slope correction) the physical variable. The thermostat and measuring systems have been provided with built-in reference junction with electrical compensation effective in the range from 0°C to 50°C.

Temperature range used in the tests varied from 22°C to 80°C. The cell surface is covered by a cork-insulating layer of 6 mm. Measured temperature variations near the oedometer ring during testing are lower than ±0.5°C at an average temperature of 80°C. Fig. 3.2 shows time evolution of soil temperature measured inside the oedometer ring in a heating phase (heating rate of 38.1°C/hour at a power input of 100 W), when the relay control system is working and finally when power supply is shut off. Average temperature of silicone oil at 10 mm from the heater is around 5°C higher than inside the oedometer ring.

3.2.2.2 Experimental layout. Auxiliary devices

Fig. 3.3 shows a typical layout of the temperature controlled testing system and a number of auxiliary devices necessary to perform the tests: measuring devices for water volume change, diffused air volume indicators, air and water vapour traps, pressure regulators, air and water pressure systems, air-water interfaces, thermocouples, temperature controllers and recording devices.

A graduated glass burette containing a meniscus formed by two immiscible fluids (water and kerosene or a special thinner) and enclosed in a perspex cylinder is used as measuring device for water volume change. The internal burette filled with deaired water is connected to the specimen and when water enters the sample, the interface moves down. In this way, the calibration of the burette is not pressure dependent, because the glass burette does not deform with increasing values of pore water pressures. The capacity of this volume indicator is limited to 10 cm^3 or 15 cm^3. During testing it is sometimes necessary to change

the position of the meniscus by allowing the fluid flow direction to be reversed by means of a combination of two three-way non-displacement ball valves. The drainage to the soil is closed and then by means of a purge valve installed in the air trap some water is expelled from the previously reversed system, which permits the positioning of the interface to the desired level. Afterwards, the flow direction is again reversed to the original flow direction. The initial curvature of the meniscus is restored by applying a small flow in the required direction before use. The readability of the burettes is around 25 mm^3, which corresponds to a water content resolution of about 0.07% for the conventional and thermal oedometer cells (0.02% for the lateral stress oedometer cell discussed in section 3.2.3). However, wall contamination causes the meniscus to behave poorly, making sometimes accurate readings difficult. In addition, it is important to maintain a controlled ambient temperature within a range of ±1°C, in order not to have appreciable disturbances in the readings. The measuring system has been verified by means of an electronic balance, weighing small amounts of deaired water expelled from the burette. Different sensors have been proposed for automatically measuring meniscus or interface levels in internal burettes, such as sensitive differential pressure transducers (Alva-Hurtado and Selig, 1981; Pradhan *et al.*, 1986), though Sivakumar (1993) observed calibration factors to be dependent on line pressures; optical servomechanisms with a light source and a sensor (Watts, 1980) and proximity transducer with a floating aluminium target (Lo Presti *et al.*, 1995), which can be evaluated in order to be incorporated in future research works. Short polyamide water drainage lines of 2 mm (inner diameter) × 4 mm between the cell base and the volume change device have been used to minimise expansion tubing effects. Calibrations for water volume changes usually recoverable under different back pressures have not been included, since the small immediate volume changes detected by the burettes due to the step application of water pressures are not considered in the computations of soil water intake. Air traps with a purge valve have been installed in the water pressure lines, after and before the volume change measuring device, in order to trap free air bubbles mainly during the installation procedure. The diffused air volume indicator also utilises an air trap, which is used to collect the free air accumulated beneath the ceramic discs during the diffusion process described in section 3.2.5. Vapour traps are installed in the pore air pressure lines near the oedometer cells in order to protect pressure regulators from water condensation. In addition, polyamide tubings with low cross-sectional area (2-mm inner diameter) have been utilised in the air pressure line to limit vapour transfer from the air chamber. In this way, a nearly saturated atmosphere with water vapour is created in the open air chamber at the same soil temperature, which minimises water vapour transfer from the specimen.

Equipment for handling soil specimens at the selected density, water content and temperature were also developed. Compaction can be carried out in the oedometer cell itself at variable temperatures up to a maximum of 60°C. At higher temperatures, in order to avoid the desaturation of the ceramic disc, an external mould is used. This heavy-walled and hermetic compaction mould is maintained in a silicone oil bath at a controlled temperature (refer to Fig. 3.4), using the same heating and control setup described in section 3.2.2.1 (power input limited to 25 W with a r.m.s. voltage of 50 V). Temperature measurements inside the compaction mould during heating and cooling phases are indicated in Fig. 3.2. The compaction piston is provided with Viton® o-rings and an air release valve to maintain constant water content conditions during static compaction.

3.2.2.3 Cell modifications to perform swelling pressure tests

Temperature controlled oedometer cells have been modified to perform swelling pressure tests. A specially adapted rigid loading frame formed by two loading beams connected by four rods, which is shown in Fig. 3.6 and Fig. 4.24), has been incorporated to the testing layout in order to perform constant volume swelling and shrinkage pressure tests. The flexible diaphragm and loading piston are eliminated, and only the ram, the top cap and the upper coarse porous disc giving a total weight of 3.48 N are maintained in contact with the specimen (1.8 kPa). Vertical stress is measured by an external strain gauge miniature load cell weighing 0.63 N mounted between the upper reaction frame and the loading ram of the oedometer cell. Effects of ram and o-ring friction on load cell readings are not considered, since they are minimised with Teflon® grease. The same miniature LVDT described in section 3.3.3.1 is mounted on the apparatus as shown in Fig. 3.6, measuring the relative

displacement between the cell top, where the LVDT is supported, with respect to the loading ram where the core is positioned. In this way, the deformability of the load cell is determined. Calibrations for loading system compressibility have been done and effects of apparatus deformability on swelling pressure measurements are indicated in section 6.5.

Miniature load cell presents the following manufacturer specifications: range of FS = 15 kN, sensitivity of 74.1 N/mV with excitation 15 Vdc, maximum hysteresis and non-linearity ±0.5%FS, temperature zero shift 0.018%FS/°C, temperature sensitivity shift 0.036%FS/°C (compensated up to 80°C). Calibration cycles to calculate the sensitivity of the load cell at different temperatures, which are required for the swelling pressure test at 80°C, have been carried out using a loading press with different calibrated masses and submerging the cell inside the compaction mould heating chamber used to prepare soil specimens (refer to Fig. 3.4). The operating sensitivity of the load cell / amplifier system with excitation 10 Vdc is 1.471 N/mV at 22°C (hysteresis: 0.17%FS; non-linearity: 0.30%FS), 1.490 N/mV at 60°C (hysteresis: 0.25%FS; non-linearity: 0.41%FS) and 1.493 N/mV at 70°C (hysteresis: 0.33%FS; non-linearity: 0.34%FS, presenting a maximum temperature sensitivity shift of 0.033%FS/°C. In addition, somewhat higher compressibility of the load cell have been observed at higher temperatures: 20.0 μm/kN at 22°C and 24.3 μm/kN at 70°C.

3.2.3 Lateral stress suction controlled oedometer cell

3.2.3.1 Null-type confining ring. Control system and calibration

Different methods, both compensating and semi-rigid systems, have recently been proposed to perform lateral stress measurements in oedometer cells: a null-type ring with strain gauges; an oedometer ring with a water-filled chamber connected to a pressure transducer (Dyvik *et al.*, 1985); a floating ring connected to load cells (Habib *et al.*, 1992; Habib and Karube, 1993); a splitted ring connected to LVDTs (Senneset, 1989; Senneset and Jambu, 1994); a load cell mounted in the oedometer wall (Schreiner, 1988; Schreiner and Burland, 1987; Schreiner *et al.*, 1994); and a semi-rigid system with strain gauges (Negussey, 1998). A recent review of the different systems is indicated in Dineen (1997). In this research a null-type compensating ring, similar to the one developed by Ofer (1981) and used by Ofer (1982), Ofer and Komornik (1983), Edil and Alazany (1992) and Erol and Ergun (1994), was used to determine the lateral pressure of soil specimen. A diagram of the lateral pressure ring, which is composed of a main ring and its casing, is shown in Fig. 3.5. The main ring has an inside diameter of 70 mm, a height of 30 mm and the centre section of the ring wall is machined to a wall thickness of 0.50 mm and to a height of 14 mm. The position of the 20.5 mm thick sample, with a height-to-radius relationship of 0.57 (friction effects are of certain consideration as discussed in section 4.5.1), is also indicated in the previous figure. Two active strain gauges are glued outside of the thin wall at nearly diametrically opposite points and oriented horizontally to register circumferential strains. O-ring grooves are formed at both sides of the thin section in order to create an airtight chamber between the ring wall and the casing. This chamber is filled with silicone oil of low viscosity (100 mm^2/s at 22ºC), which has been chosen because of its low electrical conductivity (no electrical interference with Wheatstone bridge). A silicone oil supply valve, a purge valve and electrical wires are connected to the top section of the ring. Lateral stress measurement can be performed by nulling the lateral strains detected by the strain gauges by means of oil pressure applied to the chamber that surrounds the deflected wall. Silicone oil pressure is applied by a ram pump connected to a continuous motor. The control electronic system of the motor was manufactured by ISMES SpA Laboratories to test saturated soils under oedometer conditions.

Electrical resistance strain gauges (ERS with resistance R_g = 120.0Ω ± 0.2% and gauge factor G_f = 2.05 ± 1.0%) are combined in a ½ Wheatstone bridge network with two active gauges with equal strains of same sign used on opposite unbalanced arms. Two active strain gauges are preferred in order to maintain the system in case one adhesive fails in this oily environment (specially when dealing with silicone oil). Partial temperature compensation of the bridge is achieved by mounting the two remaining dummy gauges inside the same chamber and glued to the rigid base of the ring, so that they

feel the same environment of the active gauges except for the mechanical strain being measured. In this way, resistance changes of the same sign caused by temperature changes will not unbalanced the bridge. However, complete temperature compensation is not feasible, even at small temperature changes, because of the difficulty of maintaining perfect symmetry in the system, as well as having gauges with well-matched temperature resistance characteristics. When possible, the whole system is maintained in a controlled water bath to improve the response of the system. This consequence is one of the reasons for not adapting the lateral stress cell for high temperature paths, where thermal strains occurring in the thin wall may be different from that of the rigid base. However, with adequate calibration procedures, temperature compensated gauges and a progressive compensation of the bridge while heated, the possibility of its use at high temperature ranges can be outlined. The non-linear output equation for resistance changes or strain detection for this type of initially balanced bridge can be expressed as (Window and Holister, 1982; Murray and Miller, 1992):

$$\frac{V_{out}}{V_{in}} = \frac{\delta R_g}{2R_g + \delta R_g} = \frac{G_f \varepsilon}{2 + G_f \varepsilon} \approx \frac{\varepsilon}{1 + \varepsilon} \tag{3.1}$$

where V_{in} is the energising input voltage (5.0 Vdc) supplied by the power unit, V_{out} the bridge output and ε the strain (negative for compression; the absolute value of the output being greater for compression than for tension). Maximum lateral strains associated with the resolution of the unbalanced signal acting on the pump motor are of the order of 0.02% to 0.04%, which is within tolerable limits for specimen ring rigidity according to ASTM D2435. Typical values of maximum lateral strains varies between 0.02% and 0.15% for semi-rigid systems and around 0.30% for compensating systems (Dineen, 1997). Okochi and Tatsuoka (1984) observed variations of K_0 within ±0.075 when varying the radia l strain of sand samples by ±0.015% in a triaxial cell.

The bridge balance to compensate for resistance tolerances of the gauges and lead wires is achieved by a potentiometer installed in the power supply unit of the Wheatstone bridge network (refer to Fig. 3.5). This enables the strains to be detected directly without having to add or subtract the initial offset, as well as to permit an initial pressure (around 50 kPa) without unbalancing the bridge due to lateral wall deflection. This initial pressure improves the response of the system, being the silicone oil less compressible and thus more appropriate to regulate under low pressures. The bridge output is amplified in the analogue control unit (refer to Fig. 3.6) changing the gain sensitivity and offset of the input signal to generate a voltage that acts on the direct current gear motor, which displaces the piston of the pressure cylinder. The pump engine group (max. capacity 3 MPa, max. input voltage 30 Vdc and max. power 3 W) is energised by this amplification of the input signal, which will be pressurising or depressurising the silicone oil system until the deflected thin wall is positioned to the initial situation. Lateral stress measurement can be performed by measuring the pressure of the silicone oil with a pressure transducer (sensitivity 1370 mV/MPa) connected to the supply line, when the target position of null deflection is achieved. Usually a null offset amplification with low gain levels is selected when steady states are being approached. In transient states a more active system is required, which can be achieved by selecting high gain levels in order to supply a higher voltage to the direct current motor. The position of the piston can be regulated inducing a fictitious offset amplification, which does not correspond to the real signal input of the Wheatstone bridge. In this way, a voltage is supplied to the motor to locate the piston at the desired level. Two relay alarms detect the initial and final positions of the piston. The pressure line is composed of rigid copper and flexible polyamide tubing connected to the oedometer ring. A safety valve controlled up to 2.5 MPa protects the thin wall and the pump engine group.

To calibrate the lateral stress system, air pressure up to 2.0 MPa is introduced in the oedometer cell, where the main ring without soil is installed. The lateral deformation of the thin wall caused by the applied air pressure is nulled by silicone oil pressure imposed by the automatic control system. The relationship between applied air pressure in the cell and the nulling pressure detected by the pressure transducer connected to the silicone oil line is shown in Fig. 3.7. The curve fitting data for different calibration cycles is also presented in the previous figure. Non-linearity and hysteresis effects are

within acceptable limits (0.29%FS, where FS stands for 2.0 MPa), which can be related to a maximum deviation of 5.8 kPa and a maximum lateral strain associated with the unbalanced signal of around 0.10%. Ageing effects were not detected in calibration cycles performed at different periods. The linear plot is then used to determine the lateral soil pressure from the required nulling pressure applied by the ram pump during the tests. The net horizontal stress (σ_h-u_a) is calculated subtracting the applied pore air pressure.

3.2.3.2 Oedometer cell and testing layout. Compaction layout

Different suction controlled tests with lateral stress measurement have been recently reported, such as Schreiner and Burland (1987), Habib *et al.* (1992), Habib and Karube (1993), Schreiner *et al.* (1994), Habib (1995), Habib *et al.* (1995) and Machado and Vilar (1997).

A scheme of the lateral stress suction controlled cell is shown in Fig. 3.8. The general description of the cell with respect to load and matric suction application is similar to what was detailed in section 3.2.2 for the thermal cell. However, the main difference is that vertical load is applied by means of pressurised air acting on a loading piston. In section 3.2.4.1 the characteristics of the loading cap with its calibration for piston pressure, as well as the deformability of the equipment under loading paths, are presented in detail. Maximum piston pressure applied in the 100-mm upper chamber is restricted to 2.5 MPa, when using a pore-air pressure of 0.50 MPa, due to the loading capacity of the 6 ϕ7 mm stainless steel screws that connect the upper part with the cell body. Movement of the loading piston is detected by a dial gauge (dial reading 0.010-10 mm), giving a volumetric strain resolution of 0.013%. Testing layout utilises the same air and water pressure systems, diffused air flushing system and water volume change equipment detailed in Fig. 3.3.

Equipment for compacting soil specimen up to a target volume under constant water content in the same null-type confining ring was also developed. The bottom part of the suction controlled cell was substituted by a steel base to protect the brittle ceramic disc and the upper part by a 70-mm compaction piston with an air release valve and a steel casing, which acts as the piston guide connecting the loading cap with the cell body. The piston base is equipped with an o-ring, which seals the compaction chamber avoiding water content losses and an upper valve releases the entrapped and pressurised air. Some of these mechanical devices are presented in Fig. 4.19b.

The oedometer cell was modified to keep a constant sample height and to register the variation of net vertical stress applied by the specimen upon wetting in the constant volume swelling pressure tests. Similar adaptations to that described in section 3.2.2.3 have been performed and are presented in Fig. 3.4 and Fig. 4.24b. Maximum weight of the loading ram connected to the miniature load cell and external LVDT, the top cap and the upper coarse porous disc is 27.2 N, which exerts an initial vertical stress of 7.1 kPa.

3.2.4 Suction controlled oedometer cells and testing layout calibrations

3.2.4.1 Mechanical calibration. Cell deformability and vertical load calibrations

Special care has been taken in order to calibrate for vertical load application and to measure the deformability under net vertical stress increase of the different oedometer cells. This normalisation procedure ensures a better reproducibility of the different measurements of the same soil packings subjected to the same stress paths taken with different oedometer cells. This calibration technique, which improves the knowledge of the imperfections of the different equipment, is important when different cells are used to test the thermal behaviour of soils. Usually, strains induced by thermal effects are smaller than the associated ones due to suction and net vertical stress paths. For this reason, results obtained with the thermal cells, which present different construction characteristics compared to conventional ones, should be previously corrected taking into account the different calibration

results before the definitive comparison of the readings associated with soil changes. In addition to the analysis of the different calibration techniques, repeatability and reproducibility of the measurements using different equipment have also been accomplished and are presented in section 4.2.2.1.

Results of the deformability of the structure of the distinct oedometer cells under net vertical stress increase and decrease are presented in Fig. 3.9. The sample of the conventional and thermal cells has been substituted by a 10-mm high stainless steel disc and 1 mm smaller in diameter than the ring. In this way, the loading element is positioned at the same level and with the same upper coarse porous stone that corresponds to the testing layout. In the case of the lateral stress device the loading platen with the coarse porous stone were directly positioned over the saturated ceramic disc, therefore not being possible to detect seating errors due to the interaction with the disc that simulates the sample. Calibration cycles have been carried out under constant u_a = 0.50 MPa and at temperatures of 22°C and 80°C. A first loading-unloading cycle was applied to eliminate the initial irrecoverable seating at the contacts between the loading head – the coarse porous stone, the porous stone – the metal disc and the steel disc - and the saturated ceramic disc. Deformations are mainly associated to seating errors due to the closing of gaps between the different elements previously indicated and compliance errors, which occur in the different porous stones as they deform under increasing load and tie screws as they extend and cause relative displacement of the cell top, where the dial gauge is supported, with respect to the loading platen where the carbide ball point is positioned. This last error is of great importance when testing at high cell pressures. Compliance and misalignment errors of the loading platen are assumed negligible. Bedding errors caused by surface irregularities at the interfaces between the specimen and the loading surfaces could not be directly determined by the calibration procedure, however it is expected that these errors are relatively small because of sample preparation technique (static compaction flat surfaces without trimming). Deformability of the cells, which is within tolerable limits accepted for this type of apparatus (Lloret, 1982; Pousada, 1984), is expressed as a percentage of the thickness of the sample, which is taken as 10 mm. Deformability of the apparatus is considered under loading-unloading paths, where usually the calibration corrections exceed 5% of the measured deformations (ASTM D2435), mainly when testing high-density packings. Deformations of the equipment are neglected in isothermal wetting-drying paths, as they are obtained at constant net vertical stress, air pressure and temperature. Micrometer reading changes when varying water pressure in order to impose a predetermined matric suction are only considered at the beginning of the suction step, when the water pressure difference generates a small displacement of the HAEV ceramic disc that affects the starting reading (offset usually less than 5 μm). Total displacements measured for a loading or unloading step under constant matric suction and temperature are corrected subtracting the corresponding calibration values for the same net vertical stress increase or decrease, according to the fitted power expressions presented in Fig. 3.9.

Calculated net vertical stress $(\sigma_v\text{-}u_a)_c$ exerted by the diaphragm or the piston pressure σ_v in conjunction with applied air pressure u_a, can theoretically be determined by considering vertical equilibrium according to the following expression (refer to Fig. 3.10):

$$(\sigma_v - u_a)_c = \frac{(A_p - A_r)\sigma_v - (A_p - A_a)u_a + (W - F)}{A} \tag{3.2}$$

where A_p is the loading platen or piston area (ϕ = 48.00 mm for the conventional cell, ϕ = 76.00 mm for the thermal cell and ϕ = 99.80 mm for the lateral stress cell), A_r the ram area (ϕ = 10.00 mm for the conventional and thermal cells, and ϕ = 13.92 mm for the lateral stress cell), and A_a the air pressure conduit area (ϕ = 2.50 mm only for the conventional and thermal cells). W represents the loading cap weight, which is only significant in the case of the lateral stress cell (W = 24.9 N), and F the maximum static o-ring friction (only applicable to the loading piston of the lateral stress cell and with a maximum value of 3.8 N under null vertical pressure). The diaphragm or piston force is divided by the coarse porous stone area A in contact with soil sample (ϕ = 49.70 mm for the conventional and thermal cells, and ϕ = 69.6 mm for the lateral stress cell). Eq. (3.2) is adequate if a total contact is ensured between the membrane and the loading cap. However, at higher diaphragm deformations

certain gap can exist between the membrane and the loading cap that can affect the net load applied on the soil.

Fig. 3.11 represents calibration results to take into account diaphragm effects and actual geometry of the loading platen on net vertical stress for the conventional and temperature controlled cells. Calibrations for piston friction effects due to o-ring seal and actual geometry of the loading piston are also included for the lateral stress cell. An arrangement for calibrations of load transmitted by the diaphragm and the piston has been designed according to the scheme shown in Fig. 3.10. The cell body was anchored to the floor and the loading ram joined to the platen was connected by a special hinge to a lever mechanism, which was acting on a calibrated load cell. Increasing and decreasing steps of diaphragm and piston pressures were applied to the different loading systems under constant u_a = 0.50 MPa and under a reference loading cap position with no membrane stretching. In addition, calibration curves for the conventional cell were verified under zero air pressure conditions, giving similar coefficients compared to the previous calibrations. The difference between measured and calculated net vertical stress is usually small for the diaphragm system, according to calibration results presented in Fig. 3.11. Maximum non-linearity and hysteresis errors for the diaphragm system on net vertical stress in loading and unloading cycles are between 0.35%FS and 0.57%FS for testing conditions with u_a = 0.50 MPa (FS stands for a reference value of $(\sigma_v\text{-}u_a)$ = 1.0 MPa). Obviously, these estimations are influenced by the non-linearity and hysteresis errors of the load cell (refer to section 3.2.2.3). However, the piston system shows a higher non-linearity and hysteresis error of 1.30%FS (FS stands for the same reference value), because of o-ring friction and distortion effects that increase at higher piston pressures. An estimation of o-ring static friction effects on net vertical stress F/A at varying piston pressures σ_v and under a constant u_a = 0.50 MPa is around $\delta(F/A)/\delta\sigma_v \approx 45$ kPa/MPa, with a minimum measured effect on net vertical stress of around 1 kPa under zero piston pressure.

Calibration curves relating diaphragm pressure corrections to true pressure acting on the sample and given by the expressions shown in Fig. 3.11 are used either for the application of specified net vertical stresses or for the determination of the actual net vertical stress from known pressures.

3.2.4.2 Temperature calibrations

In processing non-isothermal oedometer test results the deformation of the structure of the different experimental oedometer cells, as well as the water volume change of the transmission lines, were carefully calibrated for thermal expansion under non-isothermal paths. Results of the dilatation of the structure of the thermal oedometer cell under heating and cooling cycles are presented in Fig. 3.12. The loading platen with the upper coarse porous stone were directly positioned over the saturated ceramic disc, therefore not needing to correct for any metallic disc deformation that simulates the sample. Calibration cycles for every temperature step under thermal equilibrium have been carried out under constant u_a = 0.50 MPa and u_w = 0.30 MPa, and at different net vertical stresses (0.026 and 0.085 MPa), which are the same applied to the soil in the different non-isothermal paths. Transient thermal deformation during heating or cooling was impossible to calibrate precisely. Thermal deformations of the apparatus affecting vertical measurements, which are represented in Fig. 3.12a, are mainly associated to the dilatation of the following elements: ceramic and coarse porous discs, loading head, measurement frame and dial gauge. In the course of a heating-cooling path the measured change of vertical displacement Δh_m is corrected according to the following expression:

$$\frac{\Delta h}{h_o} = \frac{\Delta h_m}{h_o} - \frac{\Delta h_c(\Delta T)}{h_o}; \quad \frac{\Delta h_c(\Delta T)}{h_o}(\%) = -6.75\times10^{-5}(\Delta T)^2 - 7.17\times10^{-3}\Delta T \pm 0.034 \qquad (3.3)$$

where $\Delta h_c(\Delta T)$ is the calibration value for a ΔT temperature change with reference to ambient temperature T_{amb} = 22°C (negative deformations are equivalent to swelling strains) and h_o = 10 mm is the reference sample height.

Radial deformation of the ring, though apparently small to affect K_0 condition, was also considered for evaluating soil volumetric strain. However, changes of lateral stress affecting soil behaviour caused by small ring expansions and contractions that occur during non-isothermal paths could not be calibrated and thus, not being possible to take these effects into account. Nevertheless, it is assumed that these variations in the lateral stress, as well as certain loss of oedometer condition, do not have an important influence in the volume change behaviour of the dense packing with high swelling tendency that do not present thermal contraction of soil skeleton upon heating, which is the case of the tests performed. Thermal expansion and contraction of the oedometer ring at selected points and temperatures were determined with a bore gauge comparator (resolution of 1μm), previously zeroed at ambient temperature. Calibration results for three different heating-cooling cycles are presented in Fig. 3.12b. An equivalent thermal expansion coefficient $\alpha_r \approx 1.65\times10^{-5}$ °C^{-1} is obtained, which is in agreement with the linear thermal expansion coefficient of stainless steel AISI 316 (1.6×10^{-5} °C^{-1}). Maximum change in diameter of oedometer ring under applied loads is usually limited to 0.03% (ASTM D2435) in order not to lose oedometer conditions, which is obtained at a temperature change of around 20°C. Under constant volume considerations the effect of ring expansions and contractions $\Delta d/d_o$ can be related to equivalent vertical displacement changes $\Delta h_d/h_o$ in order to obtain an overall correction using Eq. (3.3), in the following way:

$$\frac{\Delta d}{d_o}(\%) = (-1.65\times10^{-3}\Delta T + 4.45\times10^{-3}) \pm 5.0\times10^{-3} \;;\quad \frac{\Delta h_d(\Delta T)}{h_o} = -2\frac{\Delta d(\Delta T)}{d_o}$$
$$\frac{\Delta h}{h_o} = \frac{\Delta h_m}{h_o} - \left(\frac{\Delta h_c(\Delta T)}{h_o} + \frac{\Delta h_d(\Delta T)}{h_o}\right) \tag{3.4}$$

where d_o = 50 mm stands for the reference sample diameter. In the first expression, negative values refer to swelling strains. The overall correction $\left(\Delta h_c(\Delta T)/h_o + \Delta h_d(\Delta T)/h_o\right)$ is represented in Fig. 3.12c. In general, the second term represents approximately 14% of the total correction, similar to the hysteresis error involved in the first term, and therefore can usually be neglected.

Void ratio changes Δe associated to volume variations of the sample ΔV (positive in compression) and temperature changes ΔT with reference to T_{amb} = 22°C can be estimated based on the assumption of a coefficient of volumetric thermal dilatation of clay particles $\alpha_s \approx 2.9\times10^{-5}$ °C^{-1} (Horseman and McEwen, 1996), according to the following expressions (subscript 'o' refers to the initial condition, whereas 'f' refers to the final stage):

$$V_o = V_{vo} + V_{so} = (1+e_o)V_{so} \;;\quad V_f = V_{vf} + V_{sf} = (1+e_f)V_{sf}$$
$$V_{sf} = (1+\alpha_s\Delta T)V_{so} \tag{3.5}$$
$$\frac{\Delta V}{V_o} = -\alpha_s\Delta T - (1+\alpha_s\Delta T)\frac{\Delta e}{1+e_o} \;;\quad \frac{\Delta e}{1+e_o} = \frac{-\frac{\Delta V}{V_o} - \alpha_s\Delta T}{1+\alpha_s\Delta T}$$

where V is the sample volume, V_v the void volume and V_s the volume occupied by solids.

To analyse thermal effects of expansion and contraction of the oedometer ring on void ratio changes, the volumetric deformation $\Delta V/V_o$ is approximate to $-2\alpha_r\Delta T$ in the absence of vertical strain, where $\alpha_r \approx 1.65\times10^{-5}$ °C^{-1} is the thermal coefficient of linear expansion of the ring. The last expression of Eq. (3.5) transforms to:

$$\frac{\Delta e}{1+e_o} \approx \frac{(2\alpha_r - \alpha_s)\Delta T}{1+\alpha_s\Delta T} \tag{3.6}$$

According to this last expression it is admitted that thermal expansion and contraction of the oedometer ring is partially compensated by the immediate response of thermal strain of clay particles, and in this sense it is expected that thermal deformations would not significantly affect the lateral stress of the specimen. This aspect has also been sustained by Towhata *et al.* (1993) when conducting non-isothermal consolidation tests on saturated clays. For an initial void ratio of $e_o \approx 0.590$ corresponding to the high-density packing and a temperature change of $\Delta T = 58°C$, the void ratio change calculated using the above expression is $\Delta e \approx 0.0004$, which is a small magnitude that can be neglected.

Water volume changes were also determined when conducting non-isothermal paths (refer to section 4.2.1.1). Careful cyclic calibrations at constant u_w = 0.05 MPa and 0.30 MPa, at constant u_a = 0.50 MPa and at different temperatures were carried out in order to determine thermal expansion of water tubings, of the low pressure chamber and the water contained within them. Water volume changes were measured with a burette (10 mm^3 readability) at a reference room temperature of 22°C. In the increasing temperature calibration process, thermal expansion of water is the dominant phenomenon, and therefore a net effect similar to water exit from sample is detected (calibration volume change ΔV_c is negative). In processing drained test results, these expansions were subtracted from measured values of water volume change ΔV_m (positive for water income). Water content changes within the soil sample Δw (positive for increasing water content) can be estimated according to the following expression, similar to that proposed by Saix and Jouanna (1990):

$$\Delta w = \frac{\gamma_{w\,(22^oC)}\left(\Delta V_m - \Delta V_c\right)}{W_s} \tag{3.7}$$

where W_s is the weight of soil solids and $\gamma_{w(22°C)}$ the reference water unit weight at 22°C. Calibration results of water volume changes at approximately steady state conditions, when no more appreciable variations are detected within an hour period, in two different heating-cooling cycles corresponding to different water pressures are presented in Fig. 3.12. Calibration volume change as a function of oedometer cell temperature change with respect to ambient temperature (T_{amb} = 22°C) for a heating path or to a reference temperature T_{ref} = 80°C for a cooling path, has been expressed as:

$$\begin{aligned} &\Delta V_c = a\Delta T^2 + b\Delta T \\ &a \approx -0.121 mm^3(^oC)^{-2} \text{ and } b \approx -3.10 mm^3(^oC)^{-1} \text{ for heating} \\ &a \approx -0.050 mm^3(^oC)^{-2} \text{ and } b \approx -11.2 mm^3(^oC)^{-1} \text{ for cooling} \end{aligned} \tag{3.8}$$

Maximum correction for ΔT = 58°C is around 0.59 cm^3 for a heating path, which is associated to an equivalent variation of water content of approximately 1.77% for the high-density packing.

The degree of saturation Sr as a function of void ratio e and water content w at a certain temperature change ΔT (reference temperature T_o = 20°C) can be evaluated by the following expression, which takes into account free water and soil particles expansion:

$$\begin{aligned} &V_v = eV_{so}(1+\alpha_s\Delta T)\ ;\quad V_w = V_{wo}(1+\alpha_w\Delta T + \overline{\alpha}_w\Delta T^2) \\ &Sr = \frac{V_w}{V_v} = \frac{wGs_o}{e}\left(\frac{1+\alpha_w\Delta T + \overline{\alpha}_w\Delta T^2}{1+\alpha_s\Delta T}\right) \end{aligned} \tag{3.9}$$

where V_v is the void volume, V_{so} the volume occupied by solids at the reference temperature, V_w the water volume, $\alpha_s \approx 2.9\times10^{-5}$ °C^{-1} the coefficient of volumetric thermal expansion of soil particles, $\alpha_w \approx 2.48\times10^{-4}$ °C^{-1} and $\overline{\alpha}_w \approx 3.45\times10^{-6}$ °C^{-2} coefficients for thermal expansion of pure free water based on experimental data, and Gs_o = 2.70 the specific gravity of soil particles at the reference

temperature. Degree of saturation changes δSr can be calculated from void ratio changes δe, water content changes δw and temperature changes δT affecting soil particles and water expansion in a free water sense, according to the following expressions based on Eq. (3.9):

$$\begin{aligned}
\delta Sr &= \frac{\partial Sr}{\partial e}\delta e + \frac{\partial Sr}{\partial w}\delta w + \frac{\partial Sr}{\partial T}\delta T \\
\frac{\partial Sr}{\partial e} &= -\frac{Gs_o}{e^2}\left(\frac{1+\alpha_w(T-T_o)+\overline{\alpha}_w(T-T_o)^2}{1+\alpha_s(T-T_o)}\right) = -\frac{Sr}{e} \\
\frac{\partial Sr}{\partial w} &= \frac{Gs_o}{e}\left(\frac{1+\alpha_w(T-T_o)+\overline{\alpha}_w(T-T_o)^2}{1+\alpha_s(T-T_o)}\right) = \frac{Sr}{w} \\
\frac{\partial Sr}{\partial T} &= Sr\left(\frac{\alpha_w + 2\overline{\alpha}_w(T-T_o)}{1+\alpha_w(T-T_o)+\overline{\alpha}_w(T-T_o)^2} - \frac{\alpha_s}{1+\alpha_s(T-T_o)}\right) \\
\frac{\partial Sr}{\partial T}\delta T &\approx Sr_o\left(\frac{1+\alpha_w(T-T_o)+\overline{\alpha}_w(T-T_o)^2}{1+\alpha_s(T-T_o)} - 1\right)
\end{aligned} \tag{3.10}$$

Special care needs to be taken to compute water content changes due to soil water evaporation through the open air pressure line. Steady state corrections similar to those described for diffused air can be applied.

3.2.4.3 Temperature and ageing effects on water permeability of HAEV discs

To obtain the values of soil water permeability for different suction and temperature conditions taking into account ceramic disc impedance, as well as to consider the impeded water flow through the ceramic disc during compression and heating in terms of an impedance factor (refer to section 5.2.1), it is important to assess the adequate disc water permeability corresponding to the different testing periods. Water coefficient of permeability of the different saturated HAEV discs (0.55 MPa of bubbling pressure) of the conventional and thermal oedometer cells were measured periodically. Demineralised and deaired water inundating the cell air chamber at a pressure of 1.0 MPa is forced to cross the ceramic disc at different temperatures (22°C or 80°C), resulting in a hydraulic head across the system of δh = 100 m calculated with a reference water unit weight of 10 kN/m^3. The volume of water flowing through the ceramic disc (thickness: δz = 7.40±0.05 mm) due to this gradient is measured using a water volume change indicator maintained at a constant ambient temperature of 22°C. This measured volume V_m at steady state conditions is plotted against elapsed time in Fig. 3.14 (conventional oedometer cells) and in Fig. 3.15 and Fig. 3.16 (thermal oedometer cells). The coefficient of permeability at different temperatures $k_d(T)$ is determined by the following expression, which takes into consideration the actual volume flowing through the disc:

$$k_d(T) = \frac{\Delta V_m\ \rho_w(22^oC)}{A\ \Delta t\ \rho_w(T)}\left(\frac{1}{\delta h/\delta z}\right) \tag{3.11}$$

where ΔV_m is the water volume measured crossing a ceramic disc of cross-sectional area A (disc diameter: 53.0 mm) during a time increment Δt. Fig. 3.14 shows permeability results for the different conventional cells at 22°C, and Fig. 3.15 and Fig. 3.16 the corresponding values for the thermal cells at different testing temperatures (22°C and 80°C). The initial permeability at 22°C (between 8.1×10^{-11} m/s and 1.5×10^{-10} m/s) is in accordance with this type of ceramic disc (around 1.2×10^{-9} m/s for a bubbling pressure of 0.55 MPa and 2.6×10^{-11} m/s for 1.52 MPa). There is also great agreement with the response of water permeability at high temperatures, where the expected values based on the characteristics of the permeant at high temperatures coincides with the decrease of absolute water

viscosity μ_w upon heating and the small effect of water density ρ_w change, according to the following expressions:

$$k_d(T) = K_d \frac{\rho_w(T)g}{\mu_w(T)} \quad ; \quad k_d(80^oC) = k_d(22^oC)\frac{\rho_w(80^oC)\mu_w(22^oC)}{\rho_w(22^oC)\mu_w(80^oC)} \approx 2.741\, k_d(22^oC) \qquad (3.12)$$

where the disc intrinsic permeability K_d, characteristic of the porous medium, is represented in Fig. 3.15. The coincident values reveal a minor thermal volume change and no significant distortion of pore geometry upon heating.

A progressive ageing effect decreasing disc porosity and consequently intrinsic permeability is observed in the different ceramic discs in contact with soil, mainly at high temperatures. Ceramic discs contain varying proportions of kaolin, talc, alumina and other clay and feldspathic materials, consisting of approximately 56% SiO_2, 15% Al_2O_3, 12% MgO and small amounts of Fe_2O_3, CaO, TiO_2, K_2O and Na_2O (Soilmoisture Equipment Corp. Specifications). This analytical composition is quite similar to that of Boom clay powder reported in section 2.1.3. Despite these small differences there are certain cation exchange effects through pore water exhibited by the ceramic discs in contact with the soil, specially over long term testing. Ions present in soil solution or in the water reservoir beneath the disc try to migrate into the porous network of the ceramic disc and diffuse throughout the disc mass tending towards equilibrium and affecting in some manner its porosity. In the same way, ions present in the water reservoir and ceramic disc are free to migrate through soil solution and diffuse throughout the soil mass, though this chemical influence is usually neglected, due to lower contact time that experiences the tested soil. Apparently, this chemically induced phenomena affecting ceramic discs are increased at higher temperatures, as observed comparing both Fig. 3.15 and Fig. 3.16 with Fig. 3.14. Ageing effects at high temperatures are accompanied by a notable darkness of the natural colour of the disc.

Permeability tests on HAEV discs with 1.52 MPa bubbling pressure of the lateral stress oedometer cell (disc diameter: 79.0 mm and thickness: $\delta z = 7.21 \pm 0.05$ mm) and the triaxial cell (disc diameter: 24.0 mm and thickness: $\delta z = 7.40 \pm 0.05$ mm) are presented in Fig. 3.17. A hydraulic head across the system of $\delta h = 300$ m has been imposed. Initial disc permeability varies between 9.8×10^{-12} m/s and 1.1×10^{-10} m/s (manufacture value for this type of disc is around 2.6×10^{-11} m/s). Ageing effects at ambient temperature have also been observed in the ceramic discs of the lateral stress cell and the top ceramic disc of the triaxial cell. The bottom ceramic disc of the triaxial cell was replaced after the first isothermal test.

3.2.5 Flushing system and diffused air volume indicators

3.2.5.1 Concepts and formulation of air diffusion through saturated ceramic discs

Water content changes in the soil are calculated by measuring the water volume that crosses the high entry disc and correcting this value taking into account the water evaporated from the specimen, which increases the relative humidity of the air chamber and condenses in the vapour trap located in the air supply line, and the amount of air diffusing through the ceramic disc. Further details of water evaporation rates are discussed in section 4.5.2.1. Though it is not totally necessary to know the exact volume of dissolved air, since in the following paragraphs an alternative procedure based on steady-state considerations is suggested to correct water volume without using direct procedures, the independently and periodically measured volume of diffused air permits to validate the correction process, as well as to prevent air accumulation beneath the disc specially at high temperatures.

When an air-water interface is established in the specimen there is the possibility for air to diffuse through the saturated ceramic disc membrane, which is installed for the prevention of free air passage between the

sample and the measuring system. After long testing periods the diffused air accumulates beneath the disc and introduces an error in either the pore-water pressure measurement associated with undrained tests or in the water volume change measurement associated with drained tests (Fredlund, 1975; Fredlund and Rahardjo, 1993), the latter being the case of interest. This type of diffusion involves gases dissolving into water according to Henry's law, diffusing through the water according to Fick's law, and then coming out from the solution in the form of air bubbles below the ceramic disc in the low water pressure chamber, again according to Henry's law. In addition, the diffused air accumulated beneath the disc can avoid water uptake, due to cavitation or by replacement of water with air, resulting in a progressive shrinkage upon wetting because of soil free water evaporation.

Soil water volume change under isothermal conditions consists of the flow of water to and from the specimen, corrected by the flow of air through water in the high air-entry disc (low pressure chamber) and the flow of free soil water evaporation in the high pressure chamber through the air pressure line. These flows, which perturb the water volume change measurement, act in opposite directions, being reflected their contrary actions in the water volume change indicator. On one hand, the diffusion process through the ceramic disc is presented as a soil water outlet, while the evaporation is registered as a water inlet into soil mass. Sometimes these overlapped effects are cancelled out and are not detected in the overall measurement, while other times it domains the diffusion effect at high matric suction levels (usually at 0.45 MPa) and others the evaporation flow at low matric suction levels. In general, the dominating flow trend is detected at the end of the lineal graphic representation of water volume change with respect to time, i.e. under steady state conditions of diffusion and evaporation. The diffused air volume recorded continuously using the water volume change indicator for the different specimens with a clear diffusion trend (negative steady-state slope when imposing a matric suction of 0.45 MPa) are compared to periodically measured values using the diffused air volume indicator, where measurements are taken at intervals of 3 days and accumulated for the testing period (refer to section 3.2.5.2). These results normalised by disc voids, multiplying the cross-sectional area by the disc porosity that is assumed around n = 31% according to Soilmoisture Equipment Corp. Specifications (n.A = 658 mm^2), are presented in Fig. 3.18. The two different procedures reported approximately the same order of magnitude values, suggesting that the linear steady-state diffusion with respect to time can be used to correct the intermediate transient water volume change readings. This way, an overall steady state correction can be applied to these representations in order to obtain the overall corrected water volume change by rotating the graph around the origin in a magnitude corresponding to the final slope. Nevertheless, measured values consistently report higher volumetric rates because overlapped evaporation effects try to diminish the diffusion steady-state slope. Differences between directly measured values and estimated from steady-state considerations can be used to approximately evaluate, within certain experimental uncertainty, the volumetric rates of evaporation at an imposed matric suction of 0.45 MPa and at a temperature of 80°C: $(0.13 \pm 0.07)\times10^{-6}$ $(mm^3/s)/mm^2$ across a unit area of disc voids. According to all previously outlined the diffused air volume should be measured independently, even if this measured value is not directly applied for the water volume correction, in order to have an estimation of its magnitude and consequences, as well as indirectly determining the rate of evaporation. Generally an increase in the diffused air flow under sustained matric suction reflects a progressive drying of the ceramic disc or the opening of a crack, which can further cause a free air passage. This progressive drying affects the soil, which shrinks due to free water evaporation specially under high temperatures (refer to section 4.2.2.1).

Theoretical models of the air diffusion process have been developed based, primarily, on Fick and Henry's laws (Barden and Sides, 1967; Pollard *et al.*, 1977; Geankoplis, 1983). Although Henry's law, which governs the solution of gas in liquid, was derived for a plane air-water interface, it has been applied to the curved air-water interface that characterises the meniscus in the disc. The rate at which air can pass through water contained in the ceramic disc can be approximately described by Fick's law of diffusion, which states that the rate at which air mass $\partial M_d/\partial t$ is transferred across a unit area of disc voids is equal to the product of a diffusion coefficient D and the diffused air concentration gradient in the y-direction expressed in terms of mass per unit volume of disc voids $\partial C_d/\partial y$ (Fredlund and Rahardjo, 1993):

$$\frac{\partial M_d}{\partial t} = -D\frac{\partial C_d}{\partial y} \tag{3.13}$$

Air diffusing through ceramic disc water is also affected by path length, following a tortuous way exceeding the overall height of the disc (though for calculations the disc thickness has been chosen), and the area available for flow or disc voids, which can be estimated multiplying the overall area of the disc by its porosity. Concentration difference is assumed equal to the difference in density M_d/V_w of the dissolved air in water under nearly saturated states, which at the same time is related to the air pressure difference u_d following the ideal gas law under isothermal conditions:

$$C_d = \frac{M_d}{nV} = \frac{M_d}{V_w} \;\; ; \qquad C_d = \frac{M_a}{RT}\frac{V_d}{V_w}u_d = \frac{M_a h}{RT}u_d \;\; ; \qquad \frac{\partial C_d}{\partial y} = \frac{M_a h}{RT}\frac{\partial u_d}{\partial y} \tag{3.14}$$

where n is the disc porosity, h is the volumetric coefficient of solubility of dissolved air in water (constant under isothermal conditions), M_a the molecular mass of dry air mixture (M_a = 28.966 kg/kmol), R the molar gas constant, T the absolute temperature and u_d the absolute dissolved air pressure. This pressure is considered equal to the free air pressure applied over the ceramic disc under steady-state conditions. On the other hand, the diffused air pressure below the HAEV disc is assumed to be the same as the water pressure u_w in the base plate low-pressure compartment, which is the pressure used in the volume measurement of the diffusing constituent (Barden and Sides, 1967). For this reason, the rate of diffusion depends on the matric suction being applied. An increase in pressure in the free air or alternatively a decrease in water pressure will develop in a pressure difference between the free and the dissolved air, becoming this difference in the driving potential to the free air to diffuse into the ceramic disc water.

3.2.5.2 Experimental measurement of the diffused air

The amount of air diffusing through the ceramic discs was obtained from different experiments that involved a progressive main wetting of different samples. It is assumed that air in the specimens at degrees of saturation less than 85%, which is the case of the different testing results used for the diffused air determination, is essentially free (not occluded and continuous) and does not interfere with the diffusion process of occluded air of the porous stone. At degrees of saturation higher than 85%, the air phase within the soil becomes occluded and the initial free air flow is reduced to a diffusion process through pore-water, interfering with the diffusion process of the ceramic disc. This is the case of a main drying path following the wetting path, where usually high degrees of saturation are attained before surpassing the soil air-entry value.

A constant u_a = 0.50 MPa was applied at the top of the specimen and varying water pressures 0.05 MPa ≤ u_w ≤ 0.44 MPa were also used at the bottom of the ceramic disc, in order to impose decreasing matric suction steps. The steady-state air flows diffusing through the ceramic disc are plotted against the applied matric suction steps in Fig. 3.19 for the different oedometer cells and different soil temperatures. The flows $\partial V_d/\partial t$ are normalised with respect to the area of ceramic disc voids. The pressure at each stage was held constant for approximately 1 week, until a clear steady-state condition has been reached. It is also possible to compute the mass rate $\partial M_d/\partial t$ of diffused air removed from the base plate applying the ideal gas law, which is also represented in the previous figure:

$$\frac{\partial M_d}{\partial t} = \frac{u_{db} M_a}{RT}\frac{\partial V_d}{\partial t} \tag{3.15}$$

where u_{db} is the absolute constant pressure used in the diffused air volume measurement (absolute diffused air pressure in the base plate), which coincides with the absolute water pressure $u_w + u_{atm}$.

The following expressions of air flow across a unit area of disc voids measured at the exit point can be obtained combining Eqs. (3.13), (3.14) and (3.15), which can also be expressed in terms of air pressure head h_d at a constant diffusing air density ρ_{db} as suggested by Fredlund and Rahardjo (1993):

$$\frac{\partial V_d}{\partial t} = -\frac{Dh}{u_{db}}\frac{\partial u_d}{\partial y} \quad ; \qquad h_d = \frac{u_d}{\rho_{db} g} \quad ; \qquad \frac{\partial V_d}{\partial t} = -\frac{Dh\rho_{db} g}{u_{db}}\frac{\partial h_d}{\partial y}$$
$$\frac{\partial V_d}{\partial t} = -\frac{DhM_a g}{RT}\frac{\partial h_d}{\partial y} = -k_d \frac{\partial h_d}{\partial y} \tag{3.16}$$

where the constituent density is determined at the constant absolute pressure u_{db}. The occluded air permeability k_d for different applied matric suctions and temperatures is also presented in Fig. 3.19. Temperature effects can be observed on occluded air permeability, presenting the heated ceramic discs higher values (around 90% higher at a matric suction of 0.25 MPa). The diffusion coefficients D for air through ceramic disc water were calculated from the previous equations, following similar criteria as Barden and Sides (1967). The diffusion coefficient values, which appear also to be temperature dependent as observed in Fig. 3.19, are in accordance to reported values corresponding to equivalent porous media that are also presented in the previous figure (for further reference values refer to Barden and Sides, 1967). Because the diffusion coefficient reduces notably with water content, similar porosity for the different saturated porous media are required in order to compare results (approximately 17% to 18% for the saturated ceramic disc). Diffusion coefficients for the ceramic discs ($D \approx 7.5\times10^{-11}$ m^2 /s) are smaller than the corresponding values for diffusion of air in free water (around 2.2×10^{-9} m^2/s at 22°C), suggesting that factors such as tortuosity of the path, breakdown of Henry's law in a curved air-water interface or the higher viscosity of the water within the disc can be associated with their reduction (Barden and Sides, 1967). However, the fact that at higher temperatures of 80°C the coefficient of diffusion increases with respect to the corresponding one at ambient temperature by a factor between 2.1 and 4.5, puts forward as evidence for viscosity of water as an important factor in governing these phenomena.

A ram pump, an air trap and a burette have been used to measure the volume of diffused air under the same imposed water pressure. Fig. 3.3 shows the arrangement connected by a valve to the base plate compartment, below the ceramic disc. The ram pump is used to establish a differential water pressure of less than 50 kPa across the base plate for approximately 30 s. This pressure gradient is the driving force for flushing water, which transports air bubbles from the base plate to the collecting air trap. Previously the water volume change indicator has been by-passed and a constant air pressure regulated at the same water pressure has been imposed to the top of the diffused air measuring burette, using the same pressure transducer. This burette (polyamide tubing of 2.7×4.0 mm) is graduated up to 2000 mm^3 with a readability of 5 mm^3 and is connected to the top part of the air trap. The valve connecting the air trap and the burette is opened and the air-water interface is positioned to the desired level in the graduated burette. The flushed air displaces the water in the burette during the upward movement of the air bubbles. Sometimes it is difficult for the bubbles to freely move up in the burette, and some small blows needs to be given to the indicator in order to help them in their movement. After removing all the diffused air, a new water level reading is recorded, being the difference from the initial reading the measurement of the air volume at the same water pressure imposed to the base plate. Corrections applying the ideal gas law to the air volume measured in the diffused air volume indicator V_m have been used to incorporate temperature differences between the base plate (T_d = 22°C or 80°C) and the measuring device (T_m = 22°C):

$$V_d = \frac{(T_d + 273)}{(T_m + 273)} \frac{(u_{atm} + u_w)}{(u_{atm} + u_w + d\gamma_w)} V_m \tag{3.17}$$

where the last correction factor takes into account pressure differences between the average air-water interface in the burette and the base plate (u_w is the water back-pressure and d ≈ 0.30 m the height difference between the interface and the base cell).

As observed in Eq. (3.16), the flow rate of air depends on the volumetric coefficient of solubility for air in water, which is also temperature dependent. In order to minimise diffusion effects at high temperatures it is important to use an adequate gas with a low volumetric solubility to impose matric suction. Fig. 3.20 presents some results of volumetric solubility in water for different gases constituents of dry air and at different temperatures. The original source of these data (Perry, 1992) presented the values in terms of a coefficient of solubility H' referenced to an absolute pressure u_g (a standard pressure of u_g = 101.3 kPa is assumed), which can be transformed to volumetric solubility h according to the following expressions:

$$u_g = H' x_g \;\; ; \qquad x_g = \frac{n_g}{n_g + n_w} \;\; ; \qquad H = \frac{\dfrac{M_g}{M_w}\dfrac{u_g}{H'}}{\left(1 - \dfrac{u_g}{H'}\right)} \approx \frac{M_g}{M_w}\frac{u_g}{H'}$$
$$h = H\frac{\rho_w(T)}{\rho_g(u_g, T)} \;\; ; \qquad h = \frac{RT\rho_w(T)}{M_w H'\left(1 - \dfrac{u_g}{H'}\right)} \approx \frac{RT\rho_w(T)}{M_w H'} \tag{3.18}$$

where x_g is the solute mole fraction in the solution; n_g and n_w the number of moles of the dissolved gas and the solvent respectively (M_g and M_w are the molecular mass of the dissolved gas and water); H the coefficient of solubility expressed in terms of the ratio between the mass of dissolved gas and the mass of liquid, which is temperature and pressure dependent; h the volumetric coefficient of solubility, which is the ratio of dissolved gas volume to the volume of liquid and that is mainly temperature dependent; R the molar gas constant; T the absolute temperature; $\rho_w(T)$ the water density; and $\rho_g(u_g,T)$ the density of the dissolved gas, which can be estimated according to the ideal gas law. As observed in Fig. 3.20, nitrogen, which is the main volumetric component of dry air (78.08%), is a suitable gas for imposing air pressure in axis translation technique at high temperatures, due to the fact that it presents a lower volumetric coefficient of solubility in water compared to dry air. It is also important to emphasise that oxygen, the second component with respect to volume in dry air (20.95%), is the one that presents the highest solubility and that gives rise to higher solubility values in the dry air mixture.

3.3 Development of Suction Controlled Isotropic Cells

3.3.1 Suction controlled mini isotropic cell

Fig. 3.21 shows an outlay of the apparatus, which is described in Cruz (1996). A small cylindrical specimen (20 mm × 20 mm) is used in order to reduce testing time to reach steady state conditions after each suction step. Air and water pressures are both imposed at the bottom of the specimen. Water pressure is controlled at the centre of the boundary by a HAEV ceramic disc of 0.5 MPa and 10 mm in diameter. Air pressure is applied through a 3-mm thick annular plate of porous stainless steel, similar to that described for the triaxial cell in the next section. Volumetric strain in the specimen is measured by controlling the water volume change of the cell chamber. Two volume change measuring devices (calibrated burette with a range of 5.0×10^3 mm^3 and a readability of 10 mm^3) are used to measure both water volume change and total volume change. However, this equipment shows a low volumetric resolution of around 0.159%, as well as a low water content resolution (around 0.10%), due to the reduced dimensions of the sample. Also small temperature variations can affect strain measurements (around 11.3 mm^3/°C or 0.180%/°C) due to thermal dilatation of water contained in the confining cell of 54.5×10^3 mm^3. Further improvements are required to incorporate more accurate and automatic water volume change devices, as well as to increase the sample volume up to a convenient size to maintain an acceptable equalisation time, while ensuring an adequate volumetric strain resolution. Auxiliary devices to prepare and place soil samples in the cell are also detailed in Cruz (1996).

3.3.2 Temperature and suction controlled triaxial cell layout. Modifications for isotropic testing

The design of a new thermal triaxial apparatus to test unsaturated soils requires the adoption of a reliable method for controlling matric suction, the development of an accurate procedure to monitor the volume change of the specimen and an adequate heating system to allow for temperature paths. Suction control has been achieved by means of different techniques: osmotic (Delage *et al.* 1987; Cui, 1993), axis translation (Sivakumar, 1993; Anderson *et al.*, 1997) and controlled relative humidity of the atmosphere that surrounds the soil (Lagny, 1996). Monitoring of cell fluid in double-walled cells (Bishop and Donald, 1961; Wheeler, 1986; Josa *et al.*, 1987; Josa, 1988), volume-pressure controllers for air and water volume change measurements (GDS unsaturated soil testing system: Adams *et al.*, 1996), digital imaging techniques (Macari *et al.*, 1997) and the use of internal local transducers (Maswoswe, 1985; Drumright, 1987; Anderson *et al.*, 1997) have been used for the measurement of the volumetric deformation of the sample.

This section describes the new hydraulically loaded triaxial apparatus specifically designed for unsaturated soil testing with simultaneous control of stress, suction and temperature, as well as some modifications carried out to perform isotropic tests. This triaxial equipment has been built according to the cross-section scheme and picture shown in Fig. 3.22a (Romero *et al.*, 1997) and in Fig. 3.22b. The basic design of the cell is based on the Bishop and Wesley (1975) hydraulic triaxial apparatus for controlled stress path testing, with a moving pedestal that pushes the soil sample against a stationary internal load cell. The apparatus is designed to test unsaturated samples of 38 mm diameter and 76 mm height in both axial compression and axial extension under either controlled rate of loading or controlled rate of strain. Axial load can be applied by means of compressed air or another fluid pushing a piston in the loading pressure chamber that acts on the lower base of the specimen. The top cap, screwed to an internal pressure and temperature compensated miniature load cell, is maintained fixed in position by an adjustable rod passing through the top of the pressure chamber. This arrangement prevents cap rotation and maintains the alignment between the loading piston and the sample cap. The loading ram, with the same diameter as the specimen throughout its height, provides the vertical stress independently from the cell pressure. The internal load cell, free of piston seal interference, is used as a redundant system in monitoring ram friction from the loading pedestal and controlling the deviatoric stress.

For isotropic tests the lower piston of the loading pressure chamber is blocked to a specified height by means of a 65-mm high steel cylinder installed between the base plate and the loading ram. The specimen top cap is disconnected from the fixed adjustable rod. During setting up, wetting and drying, loading and unloading paths it is unlikely that the sample will remain vertical. To avoid this problem a non-contact alignment device for specimen tilting control, which replaces the load cell, is used to carry out isotropic compression tests. Maximum initial tilting of specimen is thus controlled up to a maximum of 0°45'.

A novel feature of the system is the possibility of independent or simultaneous application of air and water pressures required for matric suction control to both ends of the sample. In this latter case, both top and bottom platens include a combination of two different porous stones: a peripheral annular coarse one (3.0 mm thick porous stainless steel with 15 μm pore size) connected to the air pressure line and an internal fine pore one (7.4 mm thick and 24.0 mm in diameter) with a high bubbling pressure (top and base plate assemblies are shown in Fig. 3.23). This way, both fluid pressures can be applied to the caps at the same time ensuring a significantly shorter equalisation stage, an important advantage when testing low permeability unsaturated soils. The perforated loading ram and top cap take the drainage and air pressure lines inside to the sample ends. Water content changes in the soil are calculated measuring the water volume by means of two burettes connected to both high entry discs, following a similar layout as indicated in Fig. 3.3. A diffused air flushing system is used in conjunction with both water volume change indicators.

Both air and silicone oil of low viscosity can be used as confining fluids. The latter one has been chosen because of its low electrical conductivity (no electrical interference with internal transducers), some

buoyancy effect in reducing the weight of the internal LVDTs and small rates of flow through the membrane reducing the fluid exchanges to a minimum in long-term tests (Leroueil *et al.*, 1988). Silicone rubber membranes, noted for their flexibility, resilience and tensile strength over a wide temperature range, were also developed for use at temperatures higher than 50ºC (refer to section 4.4.2.2 for the construction process). Migration of air confining fluid is reduced by using two membranes separated by a coating of silicone grease. Confining pressure is imposed by means of compressed air (maximum cell pressure is limited to 4.0 MPa), which acts over a free interface of silicone oil in an expansion chamber that compensates the thermal volumetric variations of the confining fluid (approximately an increase of 5.5% of the initial volume upon heating from 22ºC to 80ºC). A 15-mm thick perspex wall cell is externally enclosed by another stainless steel AISI 316 cylinder, also 15 mm thick, where four windows (30 mm wide) have been provided: two for observing the internal LVDT transducers and two for the laser beam to reach the specimen. Diaphragm pressure transducers are used to measure cell pressure, pore water and pore air pressures.

3.3.3 Axial displacement transducers

3.3.3.1 General characteristics

Local internal measurements of specimen axial deformation have been performed in order to exclude bedding errors at both ends of the specimen in contact with top cap and pedestal, as well as temperature effects on the stationary pedestal during heating and cooling cycles (thermal displacement of around 2.7 μm/°C for cell temperature change). In addition, no external axial measurements can be done because the upper stationary loading ram is disconnected during isotropic tests. A number of local strain measuring devices have been developed, such as electrolevel gages by Burland and Symes (1982), and Jardine *et al.* (1984); Hall effect transducers by Clayton and Khatrush (1986), and Clayton *et al.* (1989); non-contact type proximeters by El-Hosri *et al.* (1981) and Hird and Yung (1987, 1989); local deformation transducers (LDTs) by Goto *et al.* (1991); and miniature LVDTs (Cuccovillo and Coop, 1997).

Axial displacements are measured using two miniature LVDT transducers (model SM3 from Schlumberger) adhered to the membrane, mounted on two opposite sides of the sample and covering the central part of the specimen (initial length of 35 mm; refer to Fig. 3.24). Factory characteristics of these transducers are: nominal calibrated working range, ±3 mm; non-linearity, 0.4% of 6mm; typical sensitivity at 5 kHz, 136 mV/V/mm; operating temperature, -40°C to 85°C; temperature zero shift, 0.005% of 3mm/°C; temperature sensitivity shift, 0.010% of 3 mm/°C at 5 kHz; weight including leads and core, 8.7 g. LVDTs are energised with 5.17 V r.m.s. at 5.031 kHz by means of a readout/controller unit, giving a manufacturer sensitivity of 1.422 μm/mV. Analog output from this unit (0 to ±10 Vdc) gives a preconditioned signal (modified to an operating sensitivity of 0.300 μm/mV) before the connection to the A/D converter. This unit also has a display mode (average reading, peak, valley, tare and alarms), which permits to have an on-line visualisation of the axial displacement evolution, as well as to define a new offset for the LVDTs, depending on test evolution. These local devices, suitable for operation in oily environments under high levels of mechanical stress, present a wide range of strain measurement between 2.57×10^{-5} and 0.171. The lower value is assumed based on an estimated resolution of 0.10 × non-linearity error.

Interference with the actual behaviour of the specimen has been tried to be kept to a minimum. The measuring core inside the LVDT is free to move, allowing to accommodate and rotate due to non-uniformity (barrelling) of the sample at large strains. Top collars and base plates of the LVDT system are stuck to the membrane according to the scheme shown in Fig. 3.24 at electrical zero. Standard PVC wiring of transducers (temperature resistant up to 105°C) is protected by a high temperature resistant contractile wire casing.

The accuracy of the measurements, in addition to calibration errors, depends on the following sources of error:

- environmental effects (temperature and pressure cell changes);

- performance and ageing effects of the glue used and of the membrane;
- slip between membrane and soil sample; and
- resolution of the A/D converter with respect to the resolution of the transducer system.

Measurements were made to determine the effect of pressure on the output of the sensors and they were found to be insensitive to pressures over the range experienced in the tests (up to 1.5 MPa). However, some bedding errors due to top collar and base plate fittings under increasing pressures were detected in a dummy sample of stainless steel, usually between ±5 μm and ±10 μm when confining pressure is increased up to 0.3 MPa starting from atmospheric conditions. At higher values (up to 1.5 MPa), any changes were detected. Temperature effects are analysed in the following section. Slippage between membrane and specimen has been minimised by sticking together the membrane and the specimen with anaerobic catalysed silicone sealant. Resolution of the A/D converter is discussed in section 3.3.6.

3.3.3.2 Temperature calibrations

LVDT transducers were carefully calibrated for temperature effects on sensitivity and zero shifts. Calibration cycles at different temperatures were carried out submerging the LVDTs in silicone oil contained in the same heating chamber used to prepare soil specimens (refer to Fig. 3.4). The comparison procedure was conducted under steady state conditions using a certified dial gauge (0.001 – 5 mm) maintained at a constant ambient temperature. Calibration curves presented in Fig. 3.25 show an adequate linearity and hysteresis for different temperatures. Non-linearity during monotonous displacement is less than 0.43%FS (FS = 6 mm) at ambient temperature and increases slightly up to 0.50%FS at 80°C. Combined error (non-linearity and hysteresis) is limited to 0.48%FS at ambient temperature. Temperature effects on sensitivity were not detected on LVDT 2, but a small shift of –0.0123% of 3mm/°C is found in LVDT 1.

Temperature zero shift analysis involved the placement of a dummy stainless steel AISI 316 specimen covered with a 0.38 mm latex membrane inside the triaxial cell and the installation of LVDTs according to Fig. 3.24. Measured values are corrected taking into account linear dilatation of the dummy. A linear coefficient of thermal dilatation of 1.6×10^{-5}°C^{-1} has been considered. Zero shift evolution during heating paths is presented in Fig. 3.35, Fig. 3.36 and Fig. 3.37. Values of ±0.0027% of 3mm/°C have been observed between 22°C and 40°C, and of around ±0.0065% of 3mm/°C between 40°C and 60°C. Zero drift corrections were not applied to measured values since both shifts are nearly compensated in the temperature range of interest.

3.3.4 Radial displacement sensors

3.3.4.1 Introduction. Laser-based electro-optical sensors

Different electrical methods for direct measurement of local lateral deformations have been developed and used, such as the application of proximity transducers (Cole, 1978; Khan and Hoag, 1979; Symes and Burland, 1984; Hird and Yung, 1989; Shibuya *et al.*, 1994; Scholey *et al.*, 1995); Hall effect sensors (Clayton *et al.*, 1989); lateral local deformation transducers LDTs (Lo Presti, *et al.* 1995; Hoque *et al.*, 1997); radial LVDTs (Anderson *et al.*, 1997); strain gauge collars (Kolymbas and Wu, 1989); resistance wire transducers (Skopek and Cyre, 1995); and receiver and sender optoelectronic sensors (Baumgartl *et al.*, 1995). To provide reliable results, the radial measurement system has to satisfy the following requirements:

- be stable for long test duration and have a high strain resolution of at least 10^{-2} %,
- have small influence upon deformation of the specimen and not restrain or load the sample,
- be capable of measuring large deformations at several locations along the specimen height,
- not be affected by electrical noise and be accurate at high-speed automatic data acquisition,
- not be affected by changing cell pressure and temperature, and

- be simple of operation and installation.

Existing systems for lateral deformation measurements, while quite accurate, are difficult to satisfy all previously outlined criteria, specially with respect to the measurement at several locations, to sensitivity to cell pressure and temperature changes and to simplicity of installation. Due to these limitations it was decided to seek a high resolution long range detection system that could be easily located outside the cell in order to detect lateral movements along the sample profile with small target sizes and not to be affected by pressure and temperature variations within the chamber. In this sense it appeared that inductive proximity transducers for conductive targets could not be employed due to the limited detection range, usually restricted to a maximum working range of 5 mm to 10 mm and with a lower resolution at high target distances (usually around 4 μm at a detection distance of 10 mm), as well as presenting wider target areas. As a result, attention was focused on a long range electro-optical laser system delivering highly accurate sensing within a wide measurement range at higher stand-off distances from the target surface and presenting smaller target areas, which can be used to detect irregularities and inhomogeneous deformations along the sample profile that are not accessible to conventional non-contact displacement sensors.

The laser-based position sensing system utilises the principle of optical triangulation, which is schemed in Fig. 3.26a. A low-power semiconductor laser diode source with a maximum output of 3 mW emits a coherent electromagnetic radiation in the invisible infrared region of the spectrum (wavelength of 780 nm) or in the visible (wavelength of 670 nm) that strikes the target opaque or translucent surface. The diffused or scattered laser light reflecting back from the surface into the sensor head is passed through a receiver lens system and focused onto a position sensitive detector PSD. As the target moves, the position of the focused beam on the detector changes, and signal processing electronics translate the PSD output currents proportional to ($a.\tan\theta_a$) into an analog voltage Vdc proportional to displacement (refer to Fig. 3.26b). PSD sensing system utilises the light quantity distribution of the entire beam spot that is focussed on the system to determine the target position (centre of beam spot distribution). Depending on the diameter of the beam itself, measurements errors can be of certain consideration, specially where high resolution data is required. Modern technology uses a CCD discrete sensing array, which detects the peak value of the light quantity distribution for each pixel within the area of the beam spot and determines a more precise target position resolving positional changes of less than 1 μm.

LB-72 controller and LB-12 sensor head from Keyence laser displacement sensors were found to satisfy all sensitivity, environmental, size and range requirements for the testing layout. Stand-off distances from the sensor head to the target surface varies between 30 mm and 50 mm (air as transparent medium), with a measurement range of ±10 mm at a reference distance of 40 mm (refer to Fig. 3.26a). The resolution of these sensors is primarily governed by the electrical internal noise, which depends on the reference stand-off distance, the measurement range and the response speed. The selected laser transmitter and receiver displacement sensors ensure a resolution of 2 μm at a response time of 60 ms (response frequency of 6 Hz for oscillating objects). The sensors provide the following factory specifications: non-linearity around 10 μm/mm, sensitivity obtained from the analog output voltage controllers between 1 μm/mV and 2 μm/mV, and a maximum temperature zero shift of 6μm/°C. Temperature effects are due to optical alterations of the transmitter and receiver lens. In this way, operating temperature of the sensor head is limited to a maximum of 50°C. Accurate measurements are ensured regardless of operating illumination (usually limited up to a maximum of 4000 lux with incandescent or fluorescent lamps) and changes in target colour and surface condition, due to an automatic laser power and sensitivity control circuit that adjusts the received light to an optimum level. However, sudden colour and surface changes can be associated to zero shift errors on measurements.

3.3.4.2 Implementation in the triaxial cell

Radial deformations on two diametrically opposite sides of the triaxial specimen can be measured by means of this long-range electro-optical laser system mounted outside the chamber on rigid supports

attached to the cell base. The surface of the rubber membrane is illuminated by the coherent laser light, which crosses 15-mm transparent perspex wall and 25 mm of confining fluid (air or silicone oil). Usually the target surface is the latex membrane, but sometimes it is recommendable to coat part of the membrane with a thin layer of white acrylic painting in order to maintain the surface colour in long term tests (over three months period) or under varying cell temperatures, which can affect membrane characteristics. The laser-emitting portion of the sensor head is positioned at varying stand-off distances from the target surface by means of micrometer screws attached to the lateral rigid supports. A reference distance of 45 mm with 5-mm air gap between the perspex wall and the sensor head is selected when air is used as confining fluid. However, the reference distance needs to be increased up to 50 mm when using silicone oil. This relatively high reference distance allows the measurement at high cell temperatures without appreciable effects on the sensor head. An operating indicator (usually LEDs indicating in and out of range conditions) helps reaching the centre of the reference range and facilitates positioning of the transducer radially during calibration and testing. The metallic cell that surrounds the perspex window acts as a protective cover minimising ambient light effects arriving to the sensor lens. The visible red beam spot with a diameter of 1 mm, even perceptible with the invisible laser radiation of the sensor, helps to confirm the measuring position.

A novelty of this lateral measuring system is that it can be moved up and down by means of an electric motor, which acts on the vertical displacement of the sensor at a rate of approximately 2.6 mm/s. This way, the whole profile of the sample from pedestal to cap can be travelled in approximately 30 s and measured with the same strain resolution. Care has been taken in order not the exceed the response time of the transducer, in this way 300 readings have been taken at a sampling rate of 100 ms. The vertical displacement of the lateral sensors is measured by two LVDTs fixed externally to the cell, with a range of 100 mm, sensitivity of around 50 mV/mm, linearity better than 0.50% and estimated resolution of about 50 μm. The volume change determination, mainly for degree of saturation computations, is more representative of the whole specimen than that obtained from local measurements. Additionally, some non-uniformity patterns of the sample and uncertainties such as specimen tilting, restraints from end platens, deformation modes (bulging, convex or concave shapes), wetting front advances and local irregularities of the membrane surface, can be easily detected.

Each sensor is connected to a power source and the output voltages are taken from the controller to the A/D data acquisition system, which is described in section 3.3.6.

3.3.4.3 Calibrations and performance evaluation

Careful calibrations have been carried out in order to investigate refraction effects mainly in the diffusive reflectance, as well as some weak reflection consequences on the measurement outputs, due to the different transparent mediums that interfere between the sensor head and the target surface. Any object that refracts, reflects or decreases the light intensity, including dust or trapped air bubbles in the silicone oil confining fluid, may cause interference errors, which affect the output signals. Fig. 3.26c and d represent some consequences due to the refraction of the diffusive reflectance. In this way, it is important to calibrate the sensor outputs using the same layout as the testing setup. Cyclic calibration curves at different constant cell temperatures and pressures to minimise effects on perspex wall have been obtained for the laser system in combination with the two suggested cell fluids. The procedure was conducted using a certified dial gauge (0.001 - 5 mm) presenting a higher resolution than the sensors and a calibration setup to allow the placing of the carbide ball point in contact with the micrometer screws of the lateral supports, which permit the positioning of the sensor head at the desired distances. The procedure also involved the placement of a stainless steel specimen covered with a 0.38 mm untreated latex membrane (no special layer was applied) inside the triaxial cell with the same setup required for the tests. Different experimental layouts permit the calibration of the movements of the target surface with respect to a fixed position of the sensor head, which is the case corresponding to a real testing condition, as well as the movement of the sensor head with respect to a fix target surface, presenting the latter case a variable perspex wall distance in relation to the sensor head. Testing results at ambient temperature (22°C) and with air as confining fluid have shown similar sensitivities for both procedures, which can be

theoretically demonstrated according to the two-dimensional model presented in section 3.3.4.5. Therefore, it was opted, because of the difficulty of accomplishing calibrations at different cell temperatures, to follow the latter procedure. Theoretical sensitivities for the different calibration procedures can be obtained according to the expressions outlined in section 3.3.4.5.

Cyclic calibration curves presented in Fig. 3.27 show an adequate linearity and a small hysteresis for the different transparent media: air, air–perspex wall–air and air–perspex wall–silicone oil. The non-linearity at ambient temperature and with a perspex wall interference (air is the confining fluid) during monotonous displacement in incremental steps of 0.25 mm up to a partial range of FS = 5 mm is less than 14 μm, which represents a value of 2.8 μm/mm or in equivalent form 0.28%FS. Hysteresis during a displacement cycle is less than 0.32%FS. The maximum non-linearity and hysteresis error is less than 3.6 μm/mm and around 9.5×10^{-3} %/mm with reference to an initial diameter of the specimen of 38 mm. Similar calibration cycles have been performed with silicone oil of low viscosity (100 mm^2/s) as confining fluid. Special care has been taken to avoid trapped air bubbles in the silicone oil, which can cause some perturbations in the readings. Non-linearity during monotonous displacement is less than 0.30%FS and hysteresis in a cycle is around 0.34%FS. Maximum non-linearity and hysteresis error is limited to 3.9 μm/mm (1.0×10^{-2} %/mm with reference to an initial diameter of the specimen of 38 mm). Fig. 3.28 shows typical sensitivity results obtained from several calibration cycles for the two sensors at ambient temperature and with perspex wall interference (air and silicone oil as confining fluids). Sensitivity values for air are of the order of 1.634 μm/mV ± 0.30% for sensor 1 and 1.598 μm/mV ± 0.25% for sensor 2, which are within the range of manufacturer specifications. In the case of silicone oil confining fluid at 22°C, sensitivity values are around 1.559 μm/mV ± 0.29% for sensor 1 and 1.524 μm/mV ± 0.26% for sensor 2. Additional calibrations conducted over longer periods (after one year testing and with perspex wall interference and air as confining fluid) showed a relatively good long-term stability: 1.587 μm/mV ± 0.31% for sensor 1 and 1.528 μm/mV ± 0.26% for sensor 2 (the systematic shift observed in Fig. 3.28 is due to optical property changes of the perspex wall, partially filled with silicone oil).

Increasing cell pressures also induce the perspex wall outward movement, despite the use of the stainless steel confining chamber. This lateral displacement influences in a quasi-reversible way the output of the sensor, due to a reduction in the y distance indicated in scheme d of Fig. 3.26. This effect is more important when three transparent media are used, where no complete compensation is expected as discussed in section 3.3.4.5. The maximum outward movement of the perspex wall is around $\Delta y = -\Delta x = -60$ μm (mid-height of the window) at a confining pressure of 2.0 MPa. However, due to the fact that most experimental paths are carried out under constant cell pressure, no further calibrations concerning this problem are considered and attention is focused on non-isothermal paths, as further discussed.

3.3.4.4 Calibrations for non-isothermal paths. Temperature effects on sensitivity and zero shifts

Cyclic calibrations to study temperature dependence on sensitivity shift of the sensor under isothermal conditions, due to physico-chemical changes of the optical properties of silicone oil and perspex wall (index of refraction is usually temperature dependent), have been carried out using the forced convection heating system described in section 3.3.5. Sensor head maximum operating temperature at a distance of 10 mm from the perspex wall is limited to 40°C (around 35°C for a cell temperature of 60°C), due to the fact that this wall and the air gap act as an insulator minimising heat transfer from the inner cell. The calibration setup is located in a temperature controlled room, where the maximum temperature variation is (22±1)°C. Calibration curves at different cell temperatures presented in Fig. 3.27 show an adequate linearity and a small hysteresis. However, non-linearity during monotonous deformation and hysteresis errors at higher temperatures are somewhat higher, as indicated in Fig. 3.27. According to Fig. 3.28 temperature sensitivity shift is of minor importance (approximately -7.7×10^{-3} %FS/°C for sensor 1 and -1.0×10^{-2} %FS/°C for sensor 2, where °C stands for cell temperature variation and FS for 20 mm). However, the influence of cell temperature on zero shift of the sensor is caused by the lateral displacement of the rigid supports attached to the base cell where the sensors are installed (thermal

dilatation of 0.75 μm/°C, where °C stands for cell temperature variations), temperature effects on optical properties of the sensor lens and temperature induced displacements on the perspex wall. Careful cyclic calibrations presented in Fig. 3.29 have been done at three different levels (bottom, mid-height and top part of the specimen) to take into account these two latter effects at constant stand-off distance of the sensor head and monitoring its temperature in a constant laboratory environment. At a distance of 10 mm from the insulating perspex wall, which is the reference distance used in the different thermal tests, the net zero shift error is in the order of 5.4 μm/°C for sensor 1 and around 3.8 μm/°C for sensor 2, where °C stands for cell temperature change. Zero shift evolution when heating is represented in Fig. 3.35, Fig. 3.36 and Fig. 3.37. This drift is recoverable in a cooling path, as observed in Fig. 3.38. These non-compensated shifts are taken into account in processing test results. However, zero shift influence can be further minimised installing the sensor head at an adequate reference distance from the heated cell in order to avoid temperature effects on optical lens. Maximum operating target distance limited by the micrometer mechanism of the lateral support is 57.85 mm. In this way, this type of long-range transducer can be used to measure lateral displacements at high cell temperatures without important effects on sensor lens.

3.3.4.5 Theoretical considerations of refraction effects

The presence of the confining perspex cell and fluid in the line of action of the diffuse reflectance between the target and the PSD creates some optical interference, which is mainly associated to various indices of refraction changes. When the diffusive or scattered reflectance crossing one transparent medium strikes the border surface of another transparent medium its direction changes according to Snell's law of refraction, which describes the passage of light from a body A to a body B or the reverse: $n_a \sin\phi_a = n_b \sin\phi_b$, in which ϕ_a and ϕ_b denote the coplanar angles included between the normal and the directions of the ray in A and B, and n_a and n_b the respective indexes of refraction with respect to some medium (Hecht, 1987). In the following equations the indexes of refraction of the different media relative to air or vacuum are assumed to be n_a = 1.000 (air), n_p = 1.150 to 1.492 (cast perspex) and n_s = 1.403 (silicone oil at 25°C with a viscosity higher than 100 mm^2/s).

Fig. 3.26 presents three schematic representations of the refraction effects, when the diffused reflection ray crosses different layered media corresponding to the different experimental layouts. The surface of the rubber membrane is illuminated by the incident light, which crosses the different transparent media without appreciable bending. It is admitted that for transparent media the refracted rays, which are the only ones represented in the different schemes, contain more intensity than the reflected rays. The equations for the simplified geometrical two-dimensional model, which relate the parameters of the system to the horizontal distance between the sensor head and the target, are referred to the different geometries represented in the previous figure. The following equations apply for one transparent medium of air (refer to Fig. 3.26b):

$$x \tan\theta_a = b \;; \qquad \frac{\delta x}{\delta(\tan\theta_a)} = -\frac{x}{\tan\theta_a} \tag{3.19}$$

where x is the reference stand-off distance varying between 30 mm and 50 mm, b is a constant distance of 16.98 mm for this type of sensor, and θ_a the angle between the normal and the direction of the ray ($\theta_{a\,min}$ = 18.76°, $\theta_{a\,max}$ = 29.51°, and θ_a = 20.67° at x = 45 mm). The second expression represents the variation of the stand-off distance related to the change of reflected ray angle detected by the PSD, and which is an indicator of the sensitivity of the sensor.

For perspex and air transparent media, the following expressions apply (refer to Fig. 3.26c):

$$n_a \sin\theta_a = n_p \sin\theta_p \; ; \quad (x+y)\tan\theta_a + c\tan\theta_p = b$$

$$\delta(\sin\theta_a) \equiv \cos^3\theta_a \; \delta(\tan\theta_a) \; ; \qquad \delta(\tan\theta_p) = \frac{1}{n_p}\left(\frac{\cos\theta_a}{\cos\theta_p}\right)^3 \delta(\tan\theta_a)$$

$$\left.\frac{\delta x}{\delta(\tan\theta_a)}\right|_y = \left.\frac{\delta y}{\delta(\tan\theta_a)}\right|_x = -\frac{\left(x + y + \frac{c}{n_p}\left(\frac{\cos\theta_a}{\cos\theta_p}\right)^3\right)}{\tan\theta_a} \tag{3.20}$$

where x is the distance between the perspex wall and the target, y the air gap between the perspex wall and the sensor head, and c the thickness of the perspex wall (c = 15 mm). θ_a and θ_p are the angles between the normal and the direction of the ray in air and perspex, respectively. For constant values x = 25 mm and y = 5 mm, the latter one being the gap distance used in the experiments, the refraction angles present the following values: θ_p = 15.85° and θ_a = 22.98° (a value of n_p = 1.429 is assumed). The interference caused by the perspex wall allows to increase the gap distance up to a maximum of y_{max} = 14.79 mm based on an angle θ_{min} = 18.76°, presenting a maximum stand-off distance of 54.79 mm. It can also be seen that the theoretical sensitivity indicated in the last expression is equivalent for the two calibrations procedures commented in the previous section, either varying the distance x and maintaining y constant or conversely. This similarity in the sensitivity has been verified in the different calibration processes carried out.

In the case of the three transparent media (air, perspex wall and silicone oil) represented in Fig. 3.26c, the corresponding expressions are:

$$n_s \sin\theta_s = n_p \sin\theta_p \; ; \quad n_p \sin\theta_p = n_a \sin\theta_a \; ; \quad x\tan\theta_s + c\tan\theta_p + y\tan\theta_a = b$$

$$\delta(\sin\theta_a) \equiv \cos^3\theta_a \; \delta(\tan\theta_a) \; ; \qquad \delta(\tan\theta_s) = \frac{1}{n_s}\left(\frac{\cos\theta_a}{\cos\theta_s}\right)^3 \delta(\tan\theta_a)$$

$$\left.\frac{\delta x}{\delta(\tan\theta_a)}\right|_y = -\frac{\left(\frac{x}{n_s}\left(\frac{\cos\theta_a}{\cos\theta_s}\right)^3 + \frac{c}{n_p}\left(\frac{\cos\theta_a}{\cos\theta_p}\right)^3 + y\right)}{\tan\theta_s} \tag{3.21}$$

$$\left.\frac{\delta y}{\delta(\tan\theta_a)}\right|_x = -\frac{\left(\frac{x}{n_s}\left(\frac{\cos\theta_a}{\cos\theta_s}\right)^3 + \frac{c}{n_p}\left(\frac{\cos\theta_a}{\cos\theta_p}\right)^3 + y\right)}{\tan\theta_a}$$

where x, y, c, θ_a and θ_p have the same meaning as previously indicated, and θ_s refers to the refraction angle in the silicone oil. For constant values x = 25 mm and y = 10 mm, the latter one being the gap distance used in the thermal experiments, the refraction angles present the following values: θ_s = 17.32°, θ_p = 17.00° and θ_a = 24.69° (a value of n_p = 1.429 is assumed). The interference caused by the perspex wall and the silicone oil allows to augment even more the gap distance in the range of y_{min} = 3.71 mm and y_{max} = 22.46 mm based on an angle θ_{min} = 18.76°, presenting a maximum stand-off distance of 62.46 mm and a measuring range of 18.75 mm. Measured values of gap distances are y_{min} = 2.70 mm and y_{max} = 22.99 mm for sensor 1 and y_{min} = 2.83 mm and y_{max} = 23.33 mm for sensor 2, showing a good agreement with theoretical values. As observed, the calibration sensitivity is influenced by the procedure used, either varying x and maintaining y constant or the inverse process. Due to the difficulty of accomplishing the calibrations by means of the variation of the distance x between the target surface and the perspex wall, which is the real situation presented in the tests, it was decided to obtain these values by interpolation using other calibration results. The different theoretical

calibrations obtained from the previous equations contrasted with the practical calibration results are presented in Fig. 3.30. Due to the non-linear relationships of the theoretical equations, it was decided to use a reference distance of 45 mm. In general, a good agreement between theoretical and practical calibrations is observed for both sensors, giving some confidence to the interpolated results, which are the ones used to evaluate test results (1.609 μm/mV for laser 1 and 1.566 μm/mV for laser 2).

When confining pressure is increased an outward movement of the perspex wall is induced $\delta y = -\delta x$, which affects the output of the sensor. For the conditions prevailing with three transparent media, where no complete compensating effect is expected, the following expressions are obtained:

$$\delta(\tan\theta_a)\big|_x + \delta(\tan\theta_a)\big|_y = -\frac{\tan\theta_a \delta y}{a} - \frac{\tan\theta_s \delta x}{a} = \frac{\delta y}{a}(\tan\theta_s - \tan\theta_a)$$

$$\text{with} \quad a = \frac{x}{n_s}\left(\frac{\cos\theta_a}{\cos\theta_s}\right)^3 + \frac{c}{n_p}\left(\frac{\cos\theta_a}{\cos\theta_p}\right)^3 + y \tag{3.22}$$

$$\delta x_{error}\big|_y = -\left(1 - \frac{\tan\theta_a}{\tan\theta_s}\right)\delta y \approx 0.47\,\delta y$$

where $\delta x_{error}\big|_y$ is the equivalent error under a constant y distance induced by the outward/inward movement of the perspex wall. The approximation holds for x = 25 mm and y = 10 mm conditions.

3.3.4.6 Assessment of errors

There are several sources of error involved in the non-contact lateral strain measurement, which are represented in Fig. 3.31 and can be classified as:

- indentation surface errors mainly associated to membrane irregularities and to the white acrylic painting layer, which is used to maintain the target colour in long term thermal tests ($\delta_{i\,err}$ referred in Fig. 3.31a);
- lateral displacement errors due to the possible mismatch between the vertical axis and the average specimen surface (Shibuya *et al.*, 1994) or non-parallel target errors as suggested by Cole (1978), which result in an additional horizontal displacement of the target caused by the average surface tilting: $\delta_{t\,err} = \delta_v \tan\alpha_1$ or $\delta_{t\,err} = \delta_v \tan\alpha_2$ (tilting angles α_1 and α_2 shown in Fig. 3.31b);
- uncontrolled horizontal target movements perpendicular to the direction of the laser beam, which also result in an additional horizontal motion detected by the sensor (represented by $\delta_{l\,err} \approx \delta_h^2/D$ in Fig. 3.31c);
- target bedding errors due to confining pressure (membrane penetration) and temperature changes inducing membrane deformation, which can be of certain consideration due to the fact that two membranes are used during testing (a silicone membrane of 0.50 mm thick and a latex membrane of 0.38 mm);
- cell pressure and temperature induced quasi-reversible displacements of the perspex wall, which need to be taken into account in loading and unloading processes, as well as under non-isothermal paths, when three transparent media are used (when two transparent media are utilised the compensating effect is expected to be cancelled out as suggested by Eq. (3.20));
- optical effect errors (indices of refraction changes) due to the presence of the perspex cell and the confining fluid, as well as air bubbles and solid particles, interfering in the line of action between the specimen (target) and the sensor head, which can also be influenced by temperature effects affecting optical properties of the transparent media;
- temperature effect errors causing lateral displacement due thermal dilatation of the rigid supports, where the sensors are fixed (approximately an outward displacement of 0.75 μm/°C for cell temperature change);

- temperature effect errors causing vertical displacement of the fixed end platen (approximately an upward displacement of 2.7 μm/°C for cell temperature change);
- temperature effect errors due to their fluctuations affecting optical characteristics of the glass lens of the transmitter and receiver sensors (maximum operating temperature on the sensor head was limited to 40°C);
- long term effects due to silicone oil adsorption by the perspex wall, which can affect optical properties of the medium (refer to Fig. 3.28);
- resolution of the transducer system with respect to the resolution of the A/D converter.

Sources of error are usually difficult to calibrate, though they can be minimised. Target bedding errors are of major consideration under loading-unloading cycles, as well as under non-isothermal paths. Lateral tilting of the specimen surface is controlled by means of the piece that substitutes the load cell. Since the performed tests are generally associated to specimens not greatly distorted, it is reasonable to assume that angles α_1 and α_2 are similar (refer to Fig. 3.31b), and thus the combined error is not excessive. Perhaps the amount of fluctuation $\delta_{i\ err}$ appears to be less than the actual indentation of the specimen surface, due to the fact that the transducer senses the distance between the probe and a small area, not a point, of the target. This minimum detectable area is equivalent to the spot area, usually less than 1 mm in diameter. Performance of the laser system with respect to the measured tilting upon heating, mainly due to thermal dilatations affecting laser lateral supports, has been evaluated using a dummy steel sample. Spurious tilting up to a maximum of 0°1'46" has been detected in a heating path from ambient to 80°C, according to Fig. 3.32. In general, reliable results from corrected output signals can be obtained from laser sensors for the different testing paths.

3.3.5 Forced convection he ating system

Several methods of heating systems to impose a uniform temperature field in triaxial cells are described in the literature. Temperature is provided either by circulation of a fluid heated in an external chamber, usually water for limited temperature increase (Virdi and Keedwell, 1988; Savvidou and Britto, 1995; De Bruyn and Thimus, 1993, 1995 and 1996); by installing internal heaters (Burghignoli and Paoliani, 1985; Bergenstahl *et al.*, 1994; Towhata and Kuntiwattanakul, 1994 and Kuntiwattanakul *et al.*, 1995 also used propellers in the inner cell); by installing internal circulating coils (Demars and Charles, 1982); and by surrounding the cell with lateral and bottom heaters or a heating jacket (Zeuch, 1983; Agar *et al.*, 1986; Baldi *et al.*, 1986; Horseman *et al.*, 1987; Saix and Jouanna, 1990; Saix, 1991; Hueckel and Pellegrini, 1992; Lingnau *et al.*, 1993, 1995, 1996; Sultan *et al.*, 1998).

The heating system schemed in Fig. 3.33, which imposes a uniform temperature field around the specimen, consists in an external stainless steel (AISI 316) heating chamber of 1.0×10^{-3} m^3 volume with a thermostatically controlled stainless steel heater of 1000 W at 220 V housed inside. A silicone oil forced convection circulation system (viscosity of 100 mm^2/s at 22°C and 35 mm^2/s at 80°C), driven by a high pressure gear pump, is able to provide soil temperatures ranging from ambient to 80ºC. A security valve and an air trap connected to a ram feeding pump to compensate silicone oil losses during long testing periods are also incorporated in the top of the heating chamber. Trapped air is collected both at the top of the triaxial cell and the heating chamber using the main and alternative flow directions of the pump motor, in order not to have air bubbles that can interfere with the lateral electro-optical system. Flexible and high-pressure polyamide tubings (3×5 mm) are used between the heating chamber and the triaxial cell, which do not transfer pump motor vibrations to the testing equipment. A silicone oil filling circuit, which incorporates a silicone oil vessel, the pump and alternative drainage lines, is also included in the system. In the operational flow direction during testing, fluid enters the upper part of the cell and leaves the lower part, where the pump is attached. The amount of power supplied to the heater is electrically controlled (both voltage and intensity) in order to balance the heat transfer from the triaxial cell to the surrounding environment. The electric circuit is composed of different transformer units, which can supply the following r.m.s. voltages by means of a selector switch: 50 V, 125 V, 175 V and 220 V. The intensity is also controlled by a regulator (triac). Fig. 3.34 indicates the power input required to maintain under steady-state conditions a specified temperature inside the cell. The operational power

input recommended to maintain the temperature by the relay control system is also indicated in the previous figure.

A temperature display and control unit with a system of relays acts on the pump motor. When a difference higher than 1°C between the upper and lower part of the specimen is detected or when the target temperature of the lower part of the soil drops below a specified minimum usually 1°C less than the desired value, the pump motor is activated in order to impose and maintain a uniform temperature field within the cell. The velocity of the pump motor can manually be adjusted up to a maximum of 3000 rev/min (at 75 W), which corresponds to a maximum of 2.9×10^6 mm^3/min, this value calculated with the properties of heated oil with viscosity of 35 mm^2/s at testing pressures. Optimum flow conditions to ensure a uniform temperature field have been achieved selecting 1200 rev/min to 1500 rev/min, corresponding to flows of 1.2×10^6 mm^3/min and 1.5×10^6 mm^3/min, average velocities inside the conduits of 1.4×10^3 mm/s and 1.8×10^3 mm/s, and average velocities around 3.7 mm/s inside the cell.

Two type K thermocouples located close to both ends of the sample are used as feedback signals acting on two programmable thermostats (display and control units), which control independently the external heater (top thermocouple) and the pump (bottom thermocouple) and permit the automatic data logging of soil temperature. The relays acting on the a.c. transformers connected to the external heater control the amount of power supplied to this heater in order to maintain the target temperature at the top of the specimen. If temperatures higher than the target value are detected, the input power is switched off after an adjustable delay of usually 15 s. Details of calibration techniques and resolution for this type of thermocouples are discussed in sections 3.2.2 and 3.3.6, this last for the resolution of the digitised values. Temperature rise to the target value can be modified during the heating path by adjusting the intensity regulator (triac) at a certain r.m.s voltage, a minimum rate being 4°C/hour to 6ºC/hour (refer to Fig. 3.35 and Fig. 3.36). Target temperature up to 60 °C can be regulated with the relay control system up to a maximum temperature variation of ±1.5°C (refer to Fig. 3.36) and around ±2.0°C for a cell temperature of 80°C (refer to Fig. 3.37).

The 15-mm perspex wall acts as an insulator to minimise heat transfer from the inner cell (thermal conductivity and heat capacity of 0.23 W/(m.K) and 1.67 J/(g.K) respectively). All the heating system is adequately isolated to prevent heat losses, with the exception of a metallic coil that does not go through the heating chamber and is used as a controlled cooling circuit. The whole system is located in a temperature-controlled room where the maximum temperature variation is (22±1) ºC. Cooling paths are represented in Fig. 3.38, with typical rates of around -35°C/hour between 80°C and 60°C, and around -14°C/hour in the range between 60°C and 40°C. The controlled cooling circuit is required for target temperatures lower than 40°C in order to increase cooling rates.

3.3.6 Data acquisition system

Keithley System 570 data acquisition and control system with a 12 bit A/D converter (system resolution 1/4096) connected to an IBM PC AT computer has been used for data logging. Accepted analog input varies between ±10 Vdc with resolution of 4.88 mV. Available analog input ranges and gain signal conditioning provide resolutions down to 0.122 mV. The system offers either 32 channels of single-ended input or 16 channels of differential input. A conversion time of 25 μs and a sample and hold acquisition time of 5 μs allow sampling speed of 35 kHz.

Preconditioned and amplified signals to increase resolution (gain and zero-shift controlled) from different external readout/controller units, which energise 14 transducers (two miniature internal LVDTs, two laser displacement sensors, an internal load cell not active in isotropic tests, two internal thermocouples, one external thermocouple, two external LVDTs for vertical displacement monitoring of laser subjection and four pressure transducers), are all connected to the data acquisition system. The readout/controller units present the readings in a display (peak, valley and average reading functions), which allow on-line visualisation of the different measurements and there zero shifting when necessary during testing. Global A/C converter ranges from 0 to +10 Vdc. Global instrumentation amplifier has

been selected at ×1. In addition, by software selection, different local programmable gain amplifiers between ×1 and ×2 have been used. The advantage of applying gain preconditioning is that it can increase the input voltage before it is digitised by the A/D converter, providing a better resolution of the measurements (refer to Table 3.1). On the other hand, any noise on the input signal will also be amplified. For this reason and due to the fact that a maximum of 14 channels are required, sometimes with low-level signals of less than 1 Vdc, two wire differential input (positive and negative leads) has been used to minimise noise. Resolution tests for the laser and internal LVDT systems in combination with the amplifier and the A/D converter have been performed, exhibiting mainly a resolution of ±1 lsb with some random noise. This random electronic noise, which affects precision of the different measurements as much as ±0.02% of reading (around ±1 lsb), have also been minimised by averaging it at software scale. Non-linearity of ±0.025% of the A/D converter full range scale is also around ±1 lsb. The system has previously been powered on for 24 hours to allow transducers and A/D converter to come into thermal equilibrium, and minimise temperature effects on offset (±35 μV/°C±0.1 lsb at the selected instrumentation amplifier gain).

Two logging programs were written in KDAC500/I language, an interpreter that runs under BASICA, to log the output voltage of the different transducers at certain intervals and convert them in engineering units. The main program is related to data acquisition during isotropic loading-unloading, non-isothermal and wetting-drying paths. The second program is used to log data from the laser sensors and external LVDTs when measuring the lateral profiles of the sample. When the run test option is selected, the current readings of the different transducers are taken and saved as zero references for the sensors at the beginning of each test setup. Sensitivities and certain calibration factors can also be changed by software selection at the beginning of the tests. The converted results are saved in spreadsheet format in the hard disc for posterior analysis at different time intervals, which can be specified by software selection before starting the tests. Time intervals can be varied between 0.01 min and 74 min in the case of the main program, and between 0.002 s and 30 s for the high-speed data logging required for the measurement of the lateral profiles. Conventional time intervals used during long term testing are around 10 min. Minimum time interval of 0.060 s is limited due to the laser sensor response time, without loosing the resolution of 2μm. Usual time intervals for lateral profile logging are of the order of 0.10 s, which correspond to 300 readings in the 30 s that delays the laser support in travelling along the sample height. There is an option of changing these intervals of logging to higher or lower values during testing. Software provides test control with on-line presentation of geotechnical parameters. Data stored in hard disc can also be copied to floppy disc without needing to stop data acquisition. As observed in Table 3.1, reliable values can be obtained by selecting an adequate resolution of the A/D converter and by maintaining it less than the resolution of the transducer system, which is estimated around 0.1 × non-linearity and hysteresis error.

Table 3.1 Channel description and A/D resolution table for the different transducers.

Channel	Gain(input volt.range)	lsb mV	Manufact.sensitiv. and energ. voltage	Operating sensitivity	Actual range	A/D resol.	Non-lin.+hyst. (resolution)
0: air press.	1(0to+10V)	2.44	100kPa/mV (10 V)	0.200kPa/mV	0-2000 kPa	0.49 kPa	1 kPa
1: load cell	not active		74.1 N/mV (15 V)	1.471 N/mV	0-15 kN	3.59 N	45 N (4.5 N)
2:conf. press	1(0to+10V)	2.44	100kPa/mV (10 V)	0.200kPa/mV	0-2000kPa	0.49 kPa	1 kPa
3:wat. press	1(0to+10V)	2.44	100kPa/mV (10 V)	0.200kPa/mV	0-2000 kPa	0.49 kPa	1 kPa
4:LVDTint1	2 (0to+5V)	1.22	1.422μm/mV(5Vac)	0.300μm/mV	0-1500 μm	0.37 μm	6 μm (0.6 μm)
5:LVDTint2	2 (0to+5V)	1.22	1.422μm/mV(5Vac)	0.300μm/mV	0-1500 μm	0.37 μm	6 μm (0.6 μm)
6: laser 1	2 (0to+5V)	1.22	2.50 μm/mV	1.559μm/mV	0-7795 μm	1.90 μm	20 μm (2 μm)
7: laser 2	2 (0to+5V)	1.22	2.50 μm/mV	1.523μm/mV	0-7615 μm	1.86 μm	20 μm (2 μm)
8:dev. press.	not active		100kPa/mV (10 V)		0-2000 kPa		
9:LVDText1	2(0to+5V)	1.22	20 μm/mV (10 V)	19.83μm/mV	0-100 mm	24.2 μm	500μm (50μm)
10:LVDText2	2(0to+5V)	1.22	20 μm/mV (10 V)	20.45μm/mV	0-100 mm	24.9 μm	500μm(50μm)
11:bot.thermc.	1(0to+10V)	2.44		0.0126°C/mV	0-126°C	0.03°C	1°C (0.1°C)
12:up. thermc.	1(0to+10V)	2.44		0.0126°C/mV	0-126°C	0.03°C	1°C (0.1°C)
13:ext.thermc.	10(0to+1V)	0.24		1°C/mV		0.24°C	1°C (0.1°C)

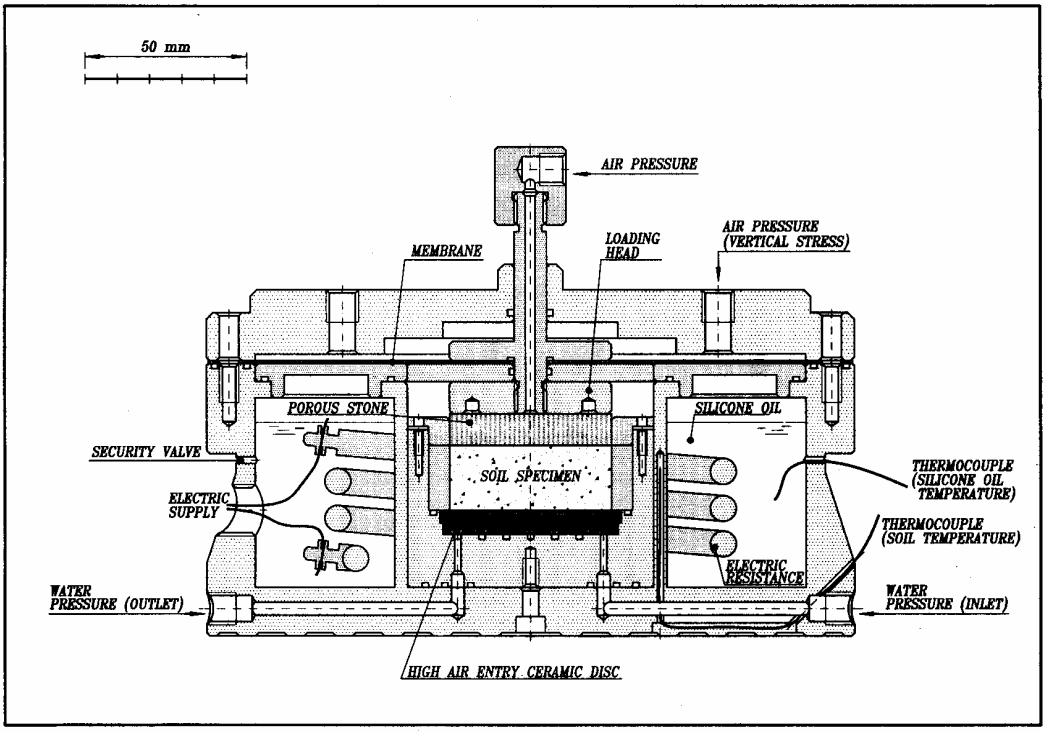

Figure 3.1 Diagram and pictures of the suction and temperature controlled oedometer cell.

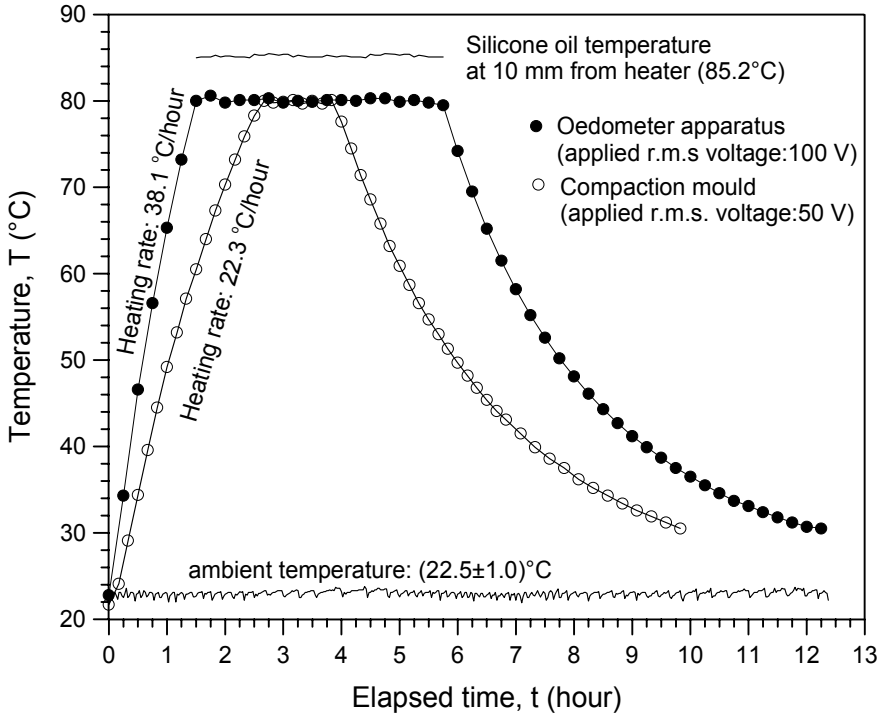

Figure 3.2 Temperature evolution during heating and cooling paths in oedometer cell and compaction mould.

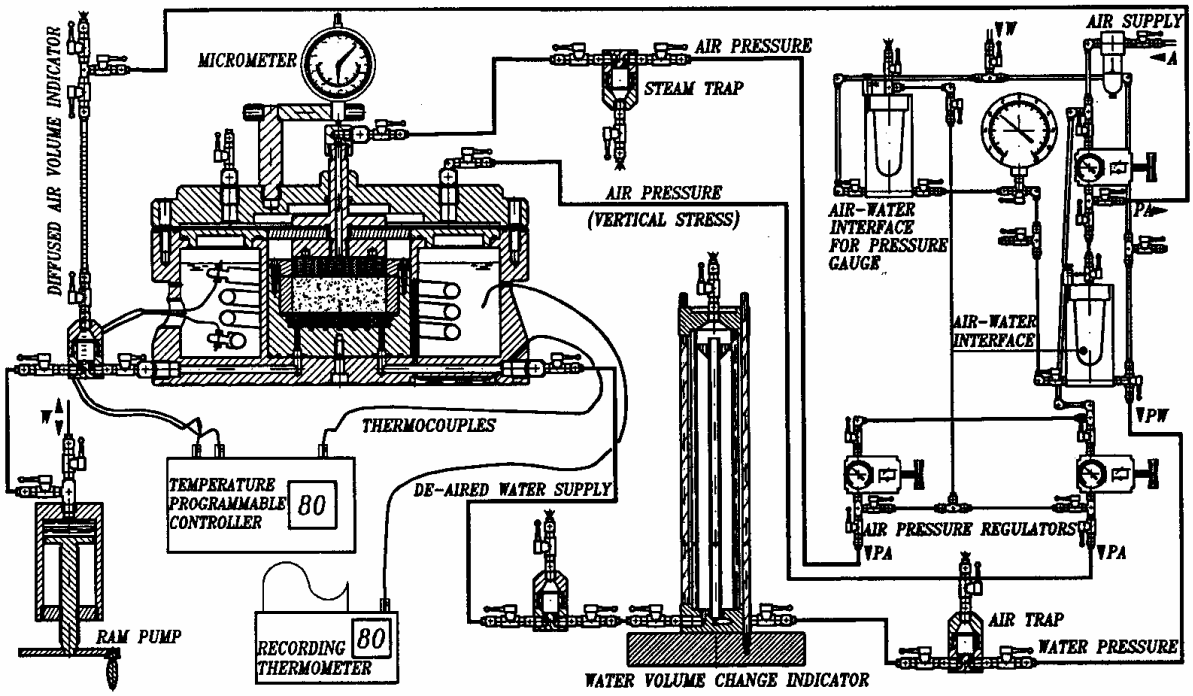

Figure 3.3 Experimental setup for temperature and suction controlled oedometer tests.

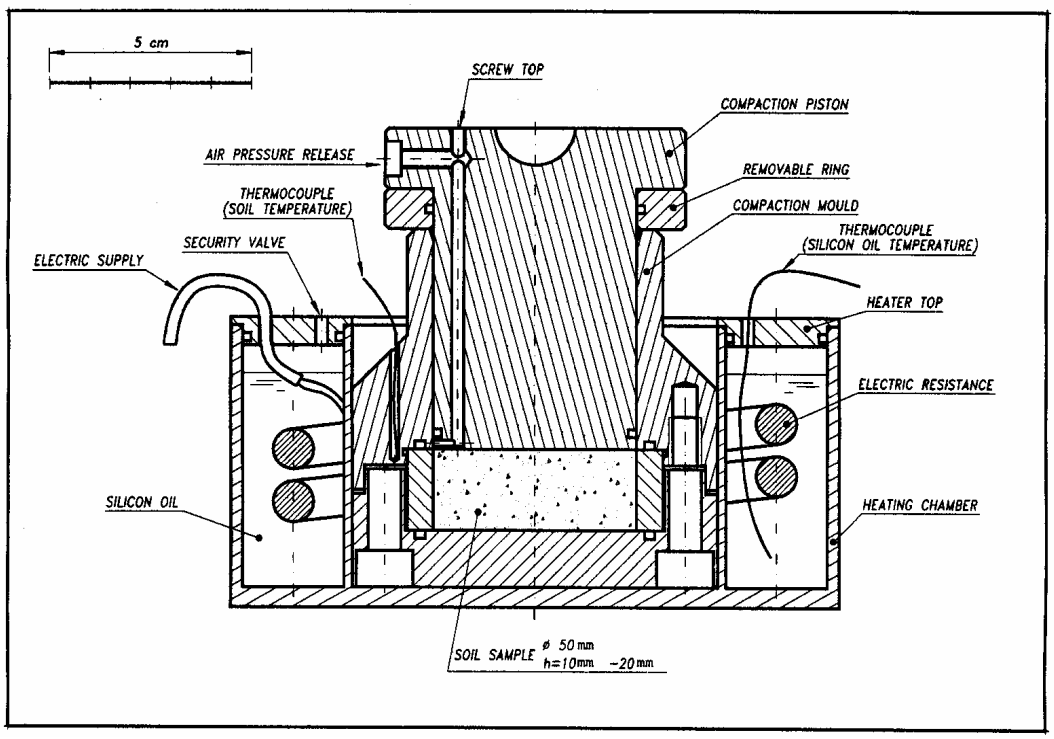

Figure 3.4 Hermetic mould and heating chamber used to prepare specimens at temperatures higher than 60°C.

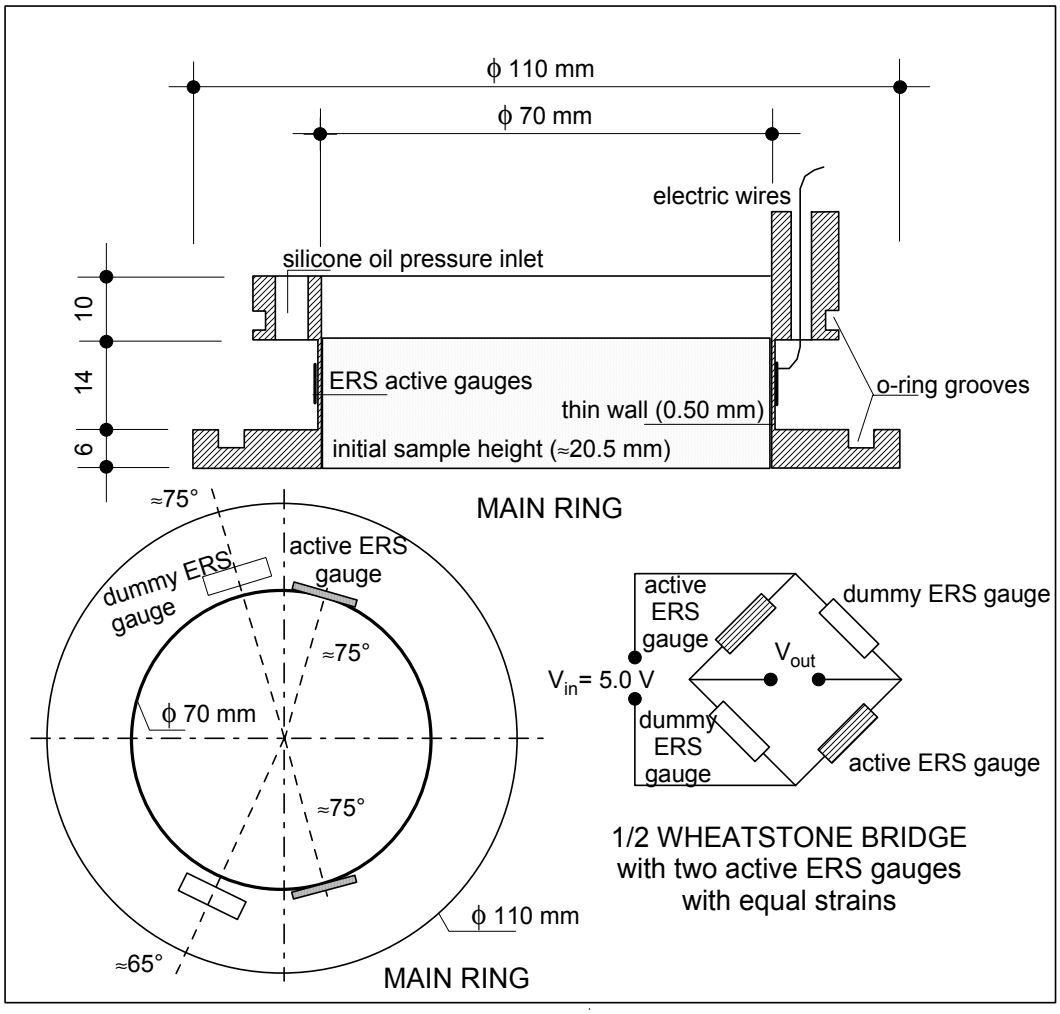

Figure 3.5 Scheme of the null-type confining ring.

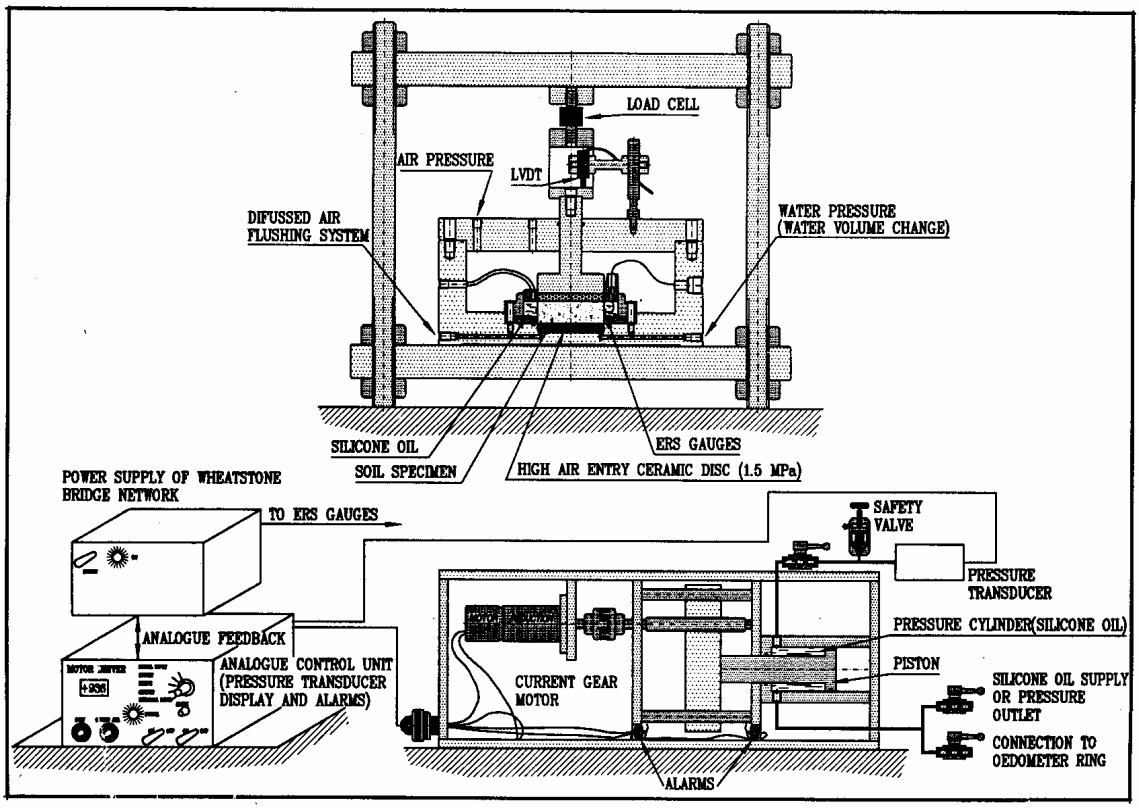

Figure 3.6 Arrangement for lateral stress swelling pressure tests. Control system and ram pump.

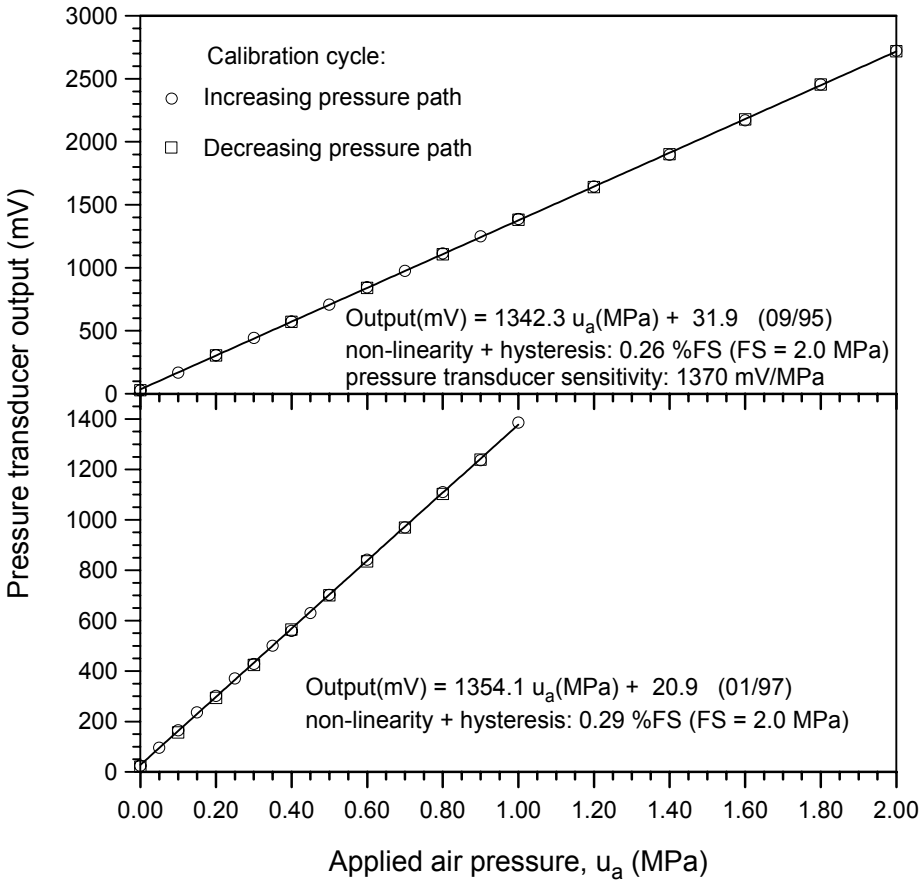

Figure 3.7 Calibration of the lateral stress system.

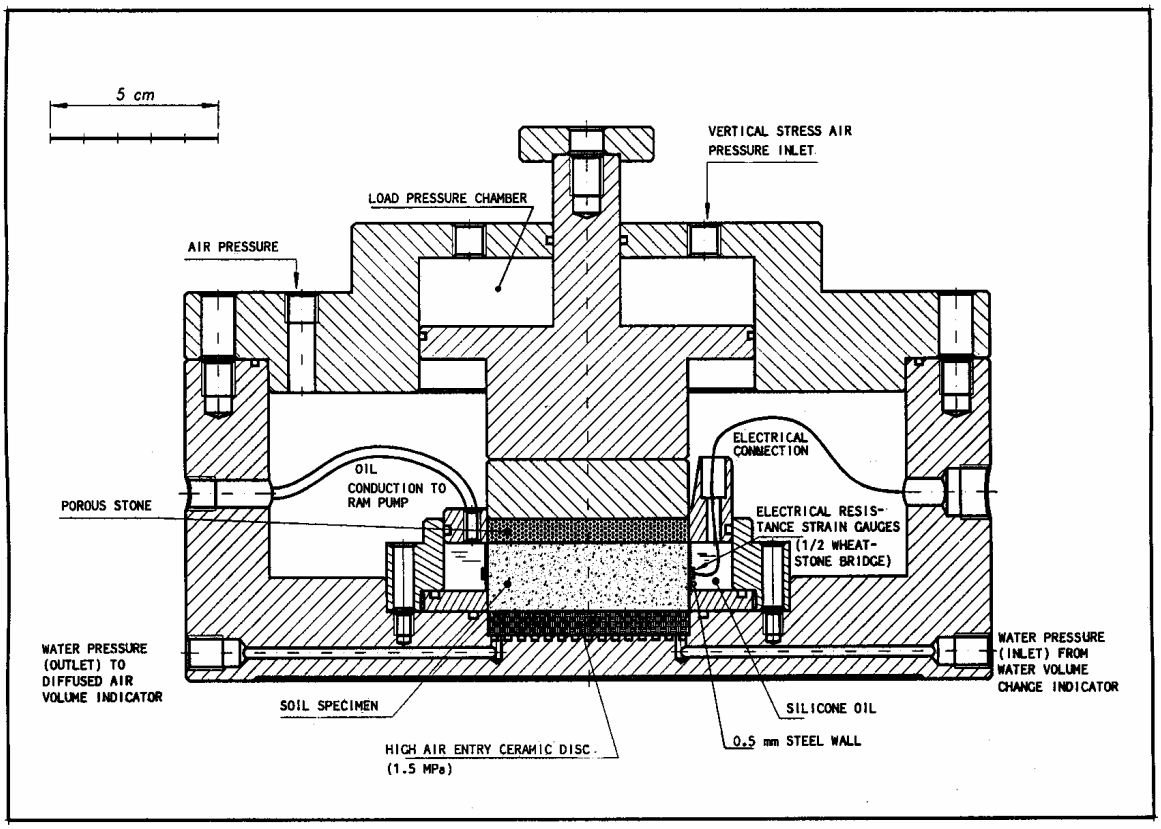

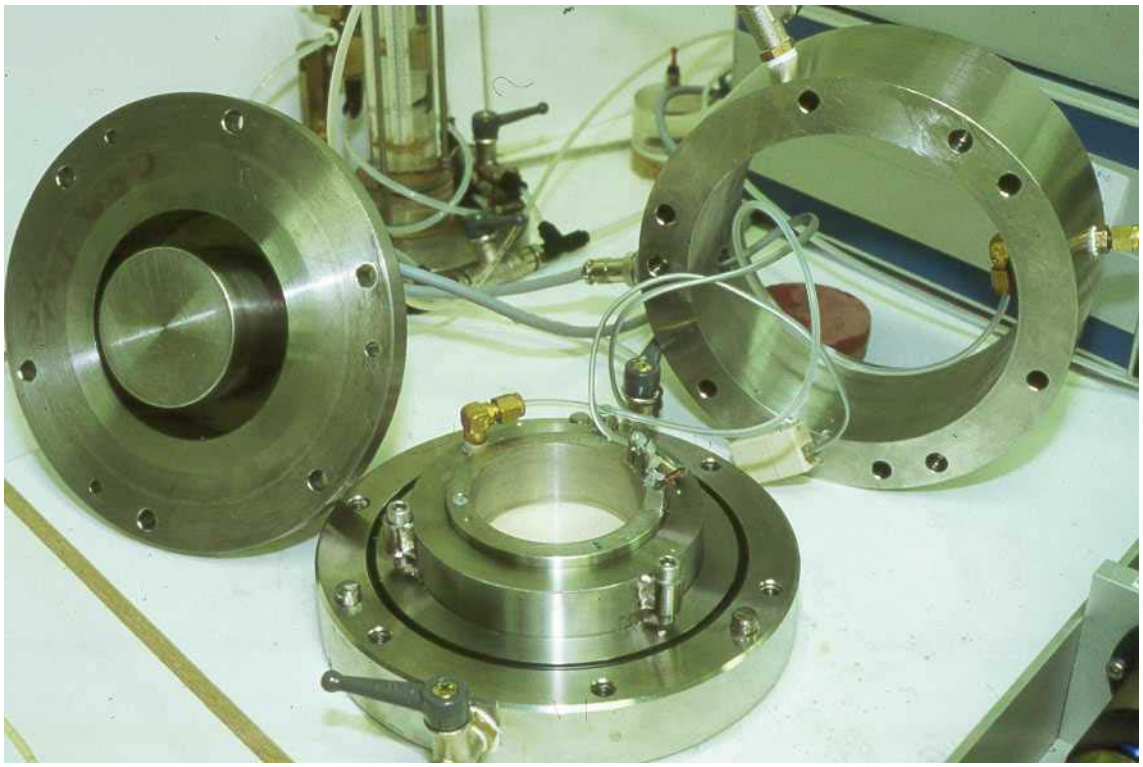

Figure 3.8 Diagram and picture of the lateral stress suction controlled oedometer cell.

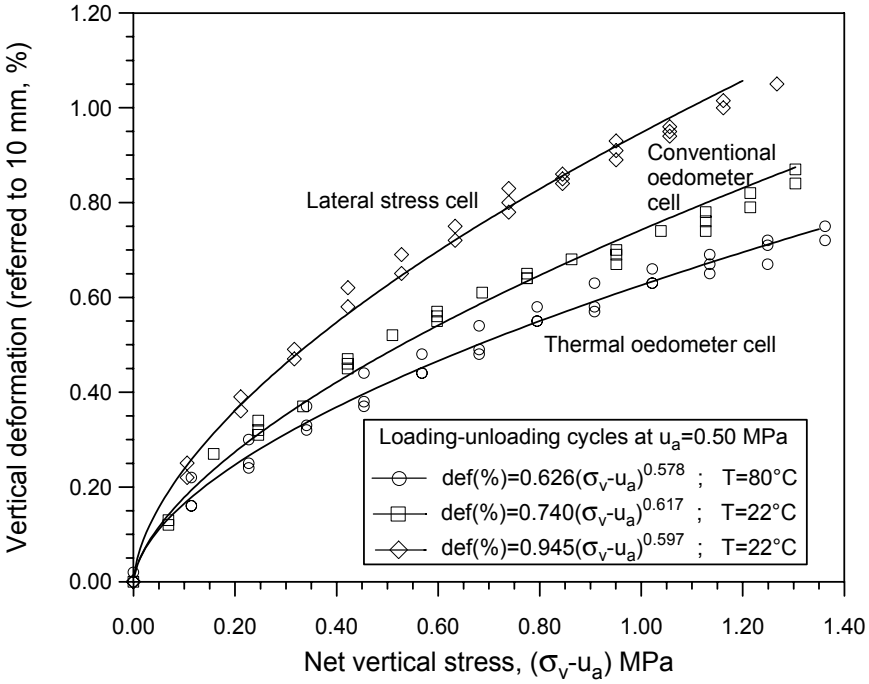

Figure 3.9 Deformability of suction controlled oedometer cells.

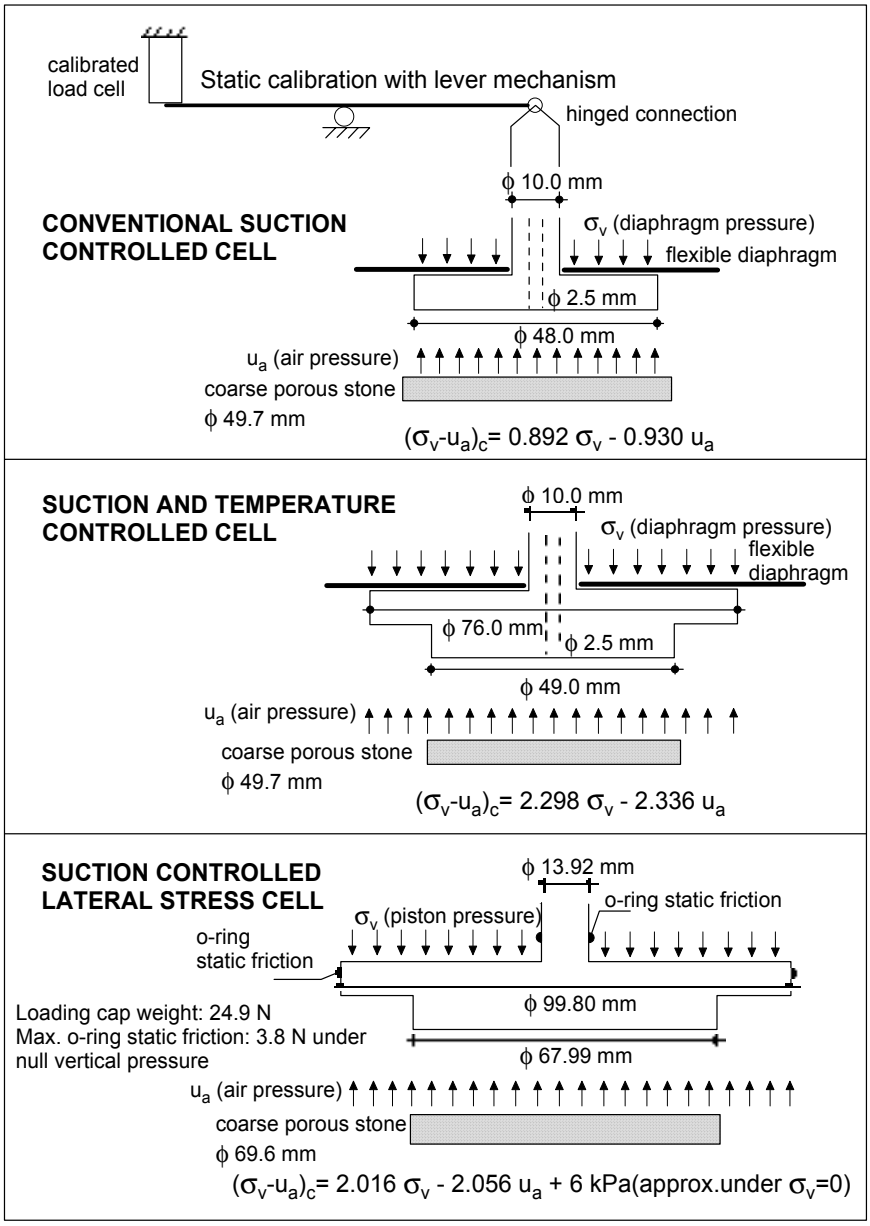

Figure 3.10 Arrangement for vertical load static calibration and theoretical relationships between diaphragm or piston pressure and transmitted net vertical load.

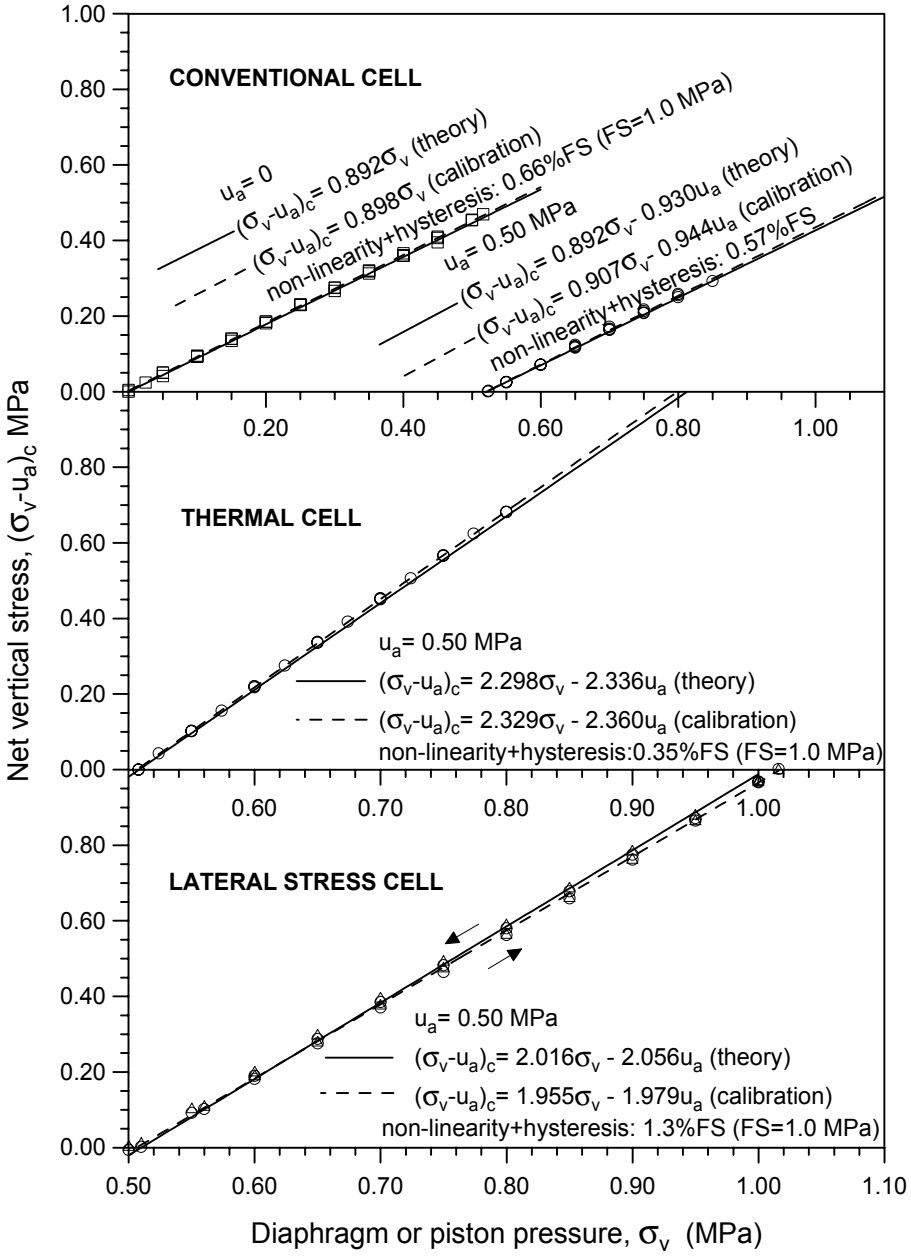

Figure 3.11 Comparison between theoretical relationships and calibration results of oedometer loading systems.

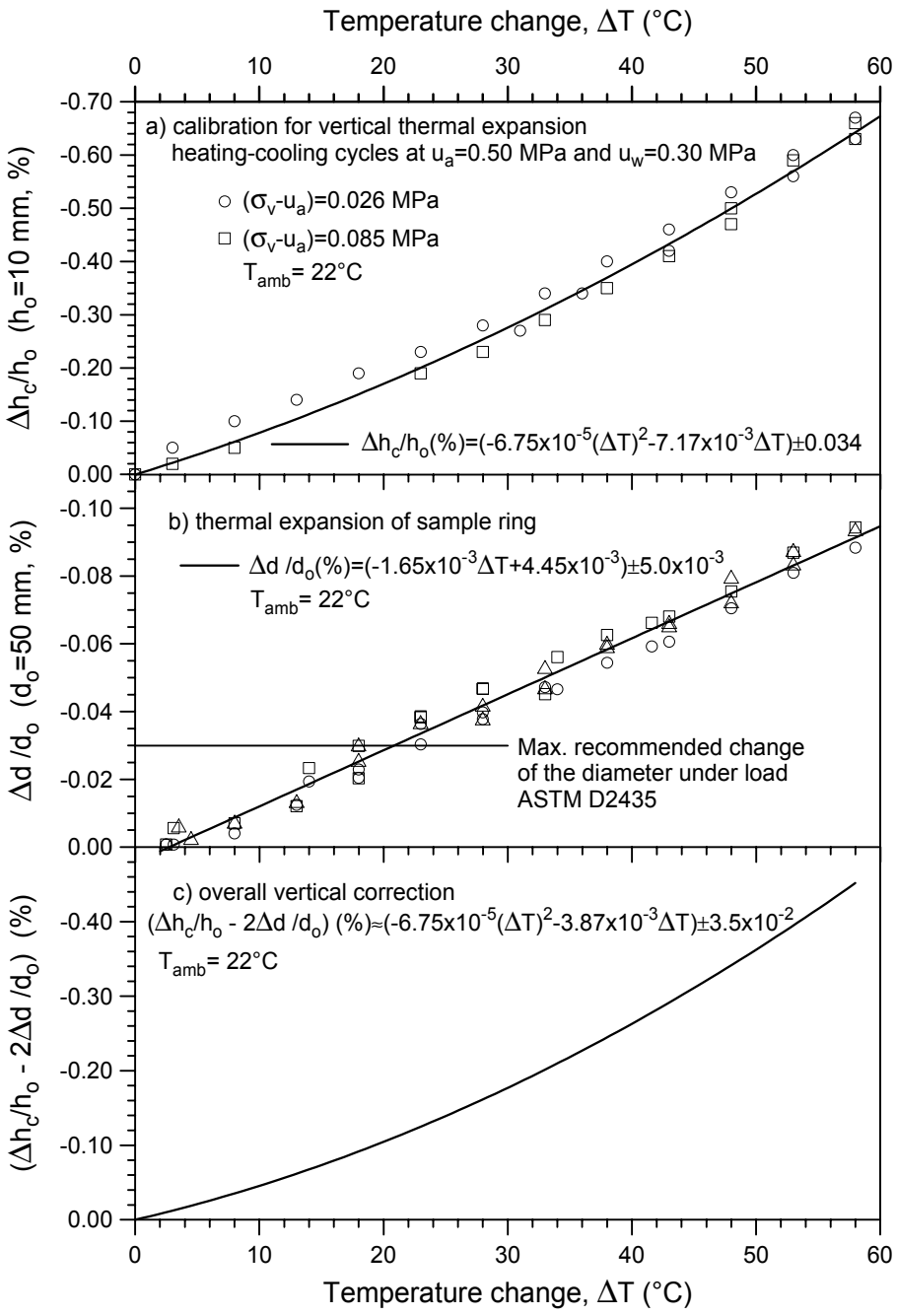

Figure 3.12 Temperature calibrations of oedometer cell for non-isothermal paths.

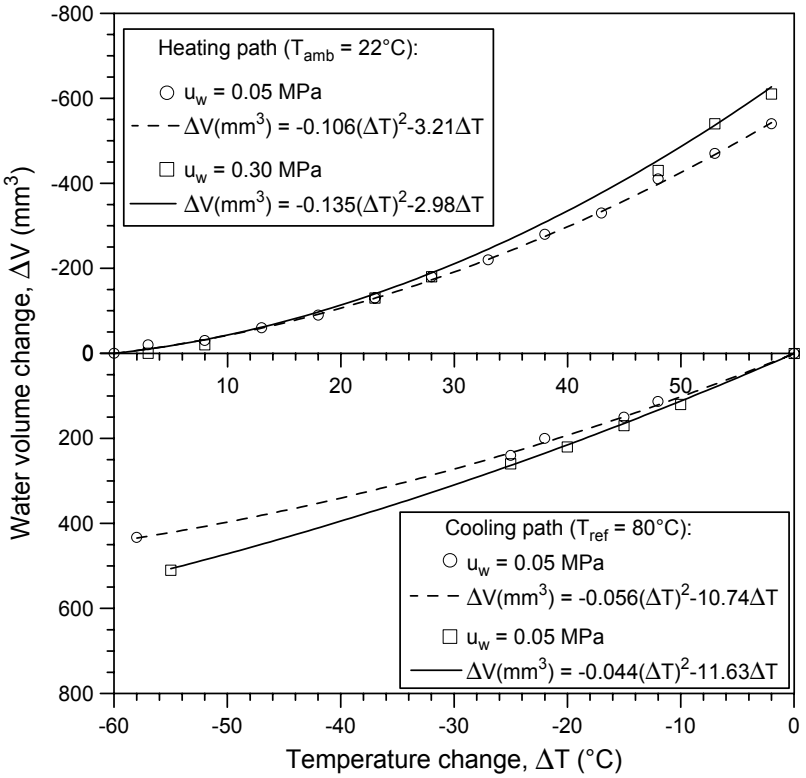

Figure 3.13 Water volume change corrections for non-isothermal paths.

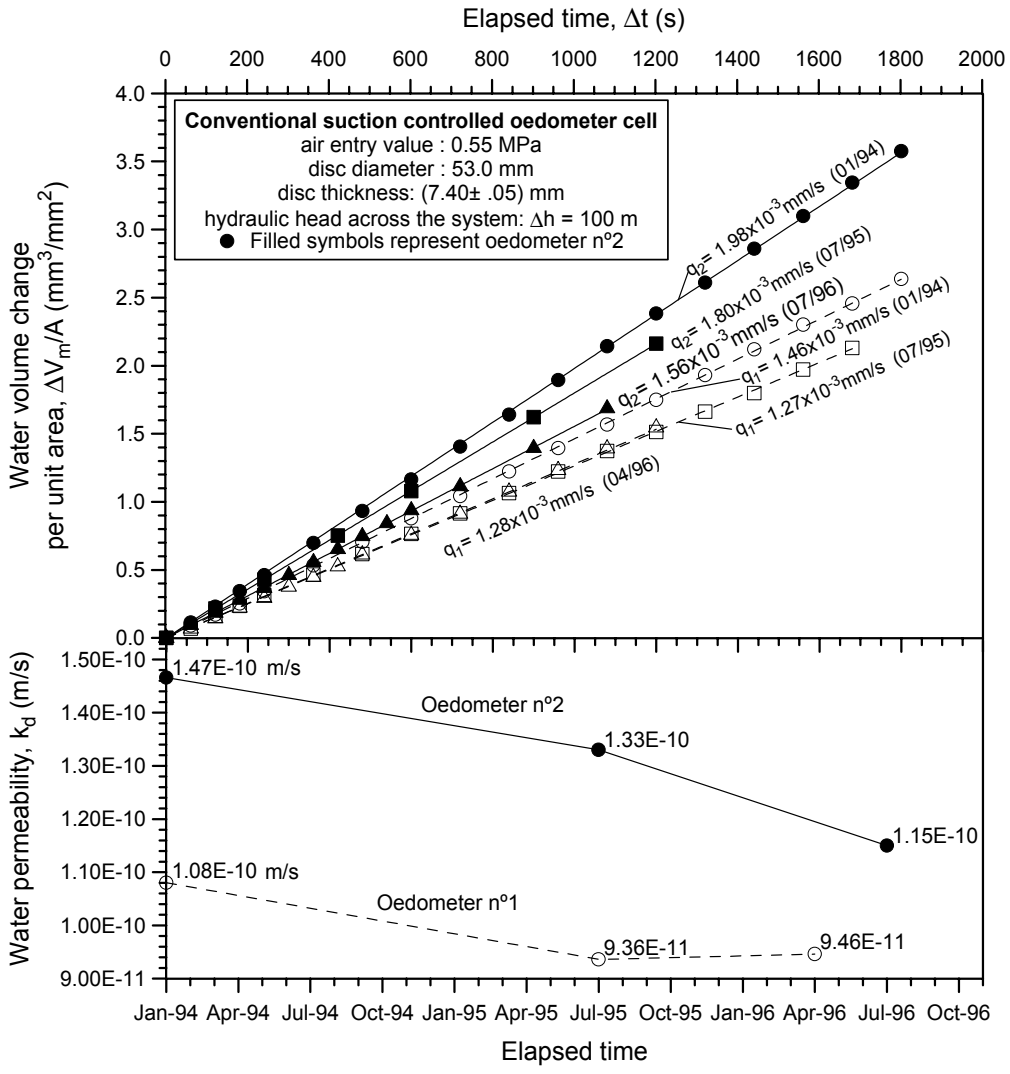

Figure 3.14 Ageing effects on water permeability of HAEV discs (conventional oedometers).

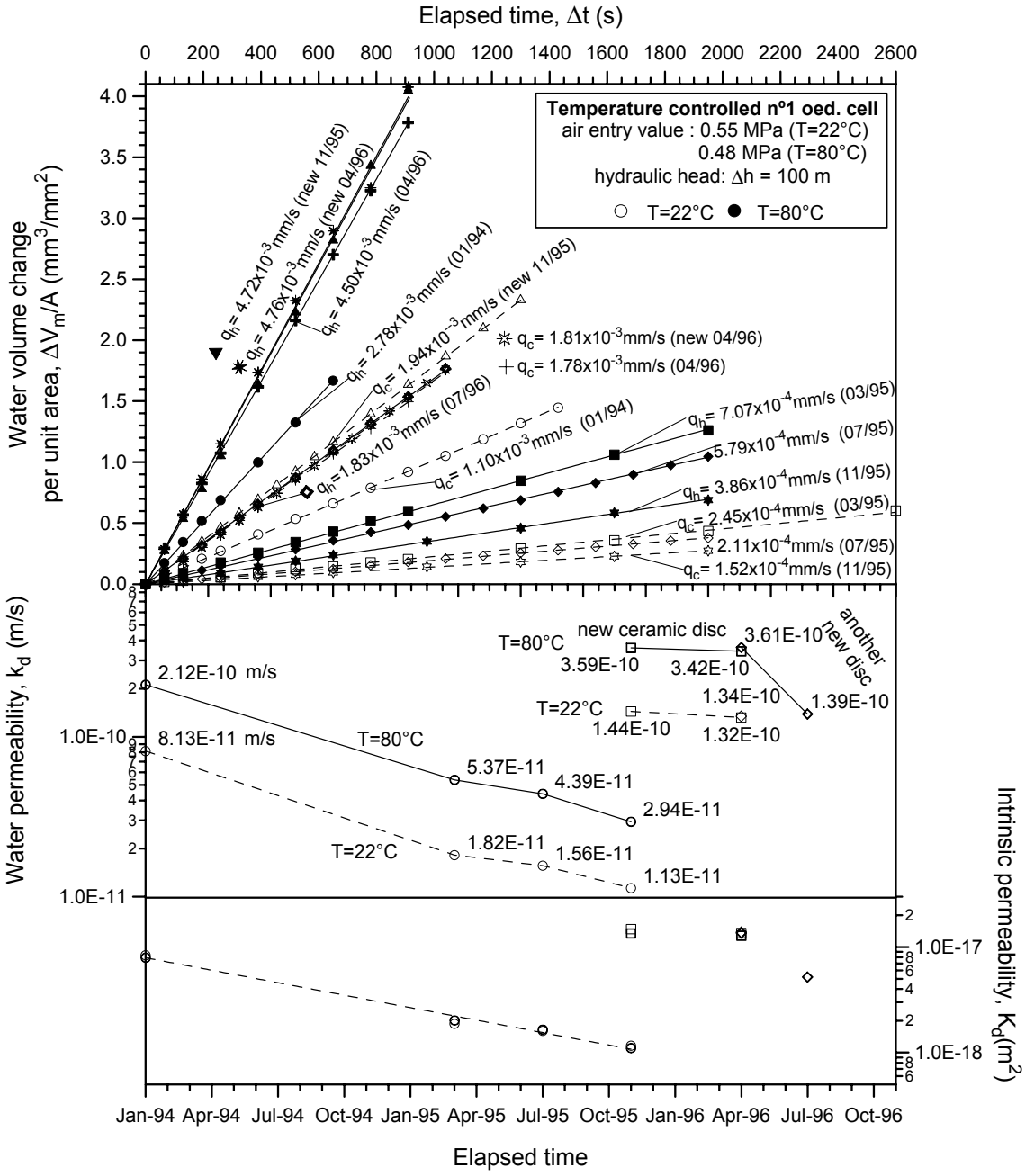

Figure 3.15 Ageing and temperature effects on water permeability of HAEV discs (thermal oedom. 1).

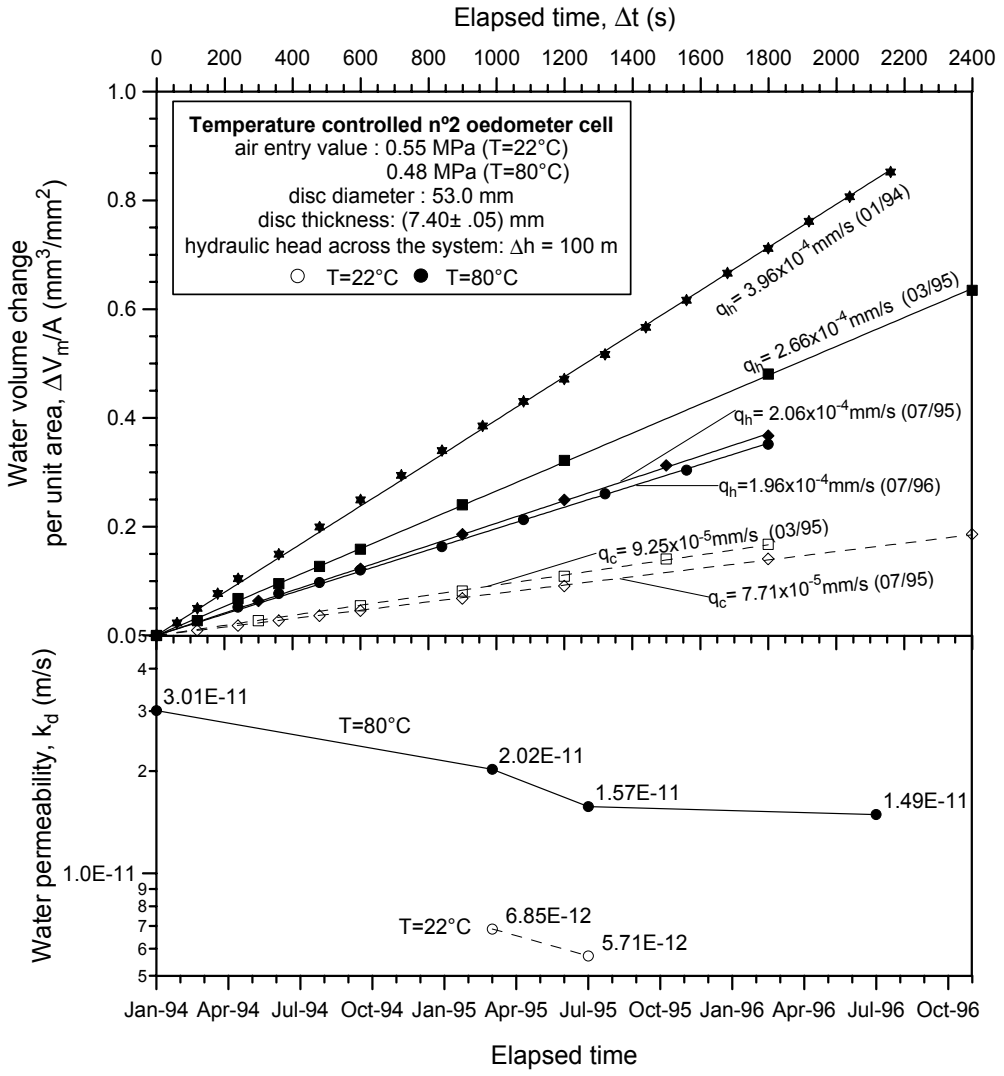

Figure 3.16 Ageing and temperature effects on water permeability of HAEV discs (thermal oedom. 2).

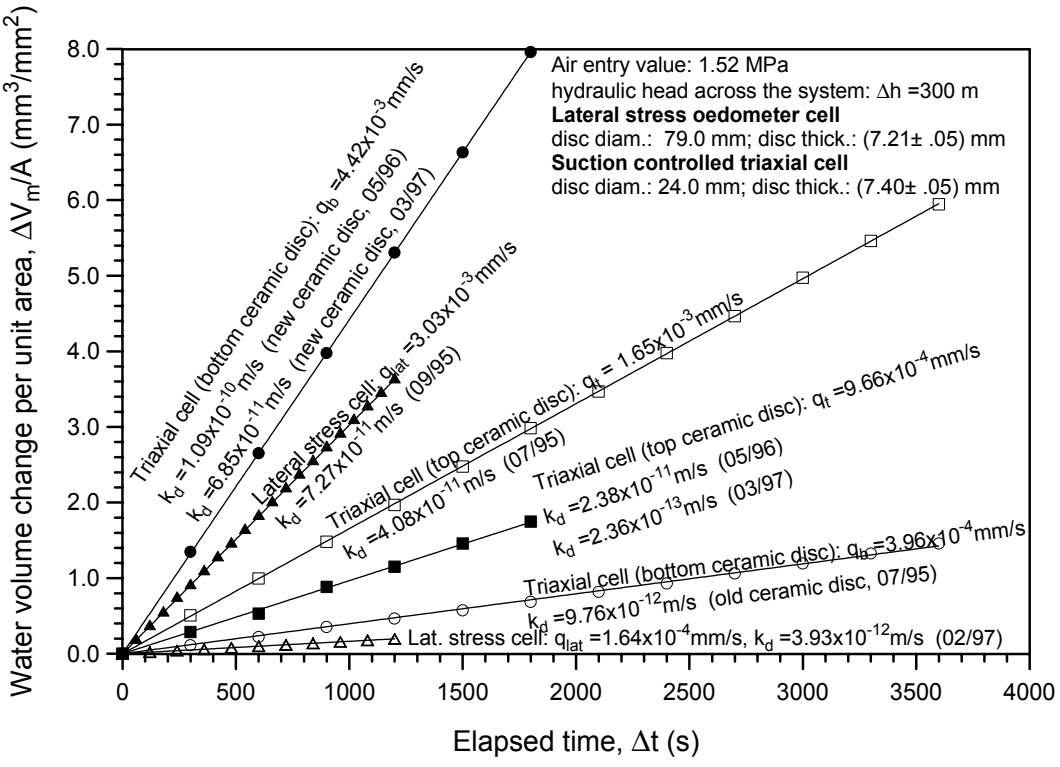

Figure 3.17 Water permeability of HAEV discs (lateral stress cell and triaxial cell).

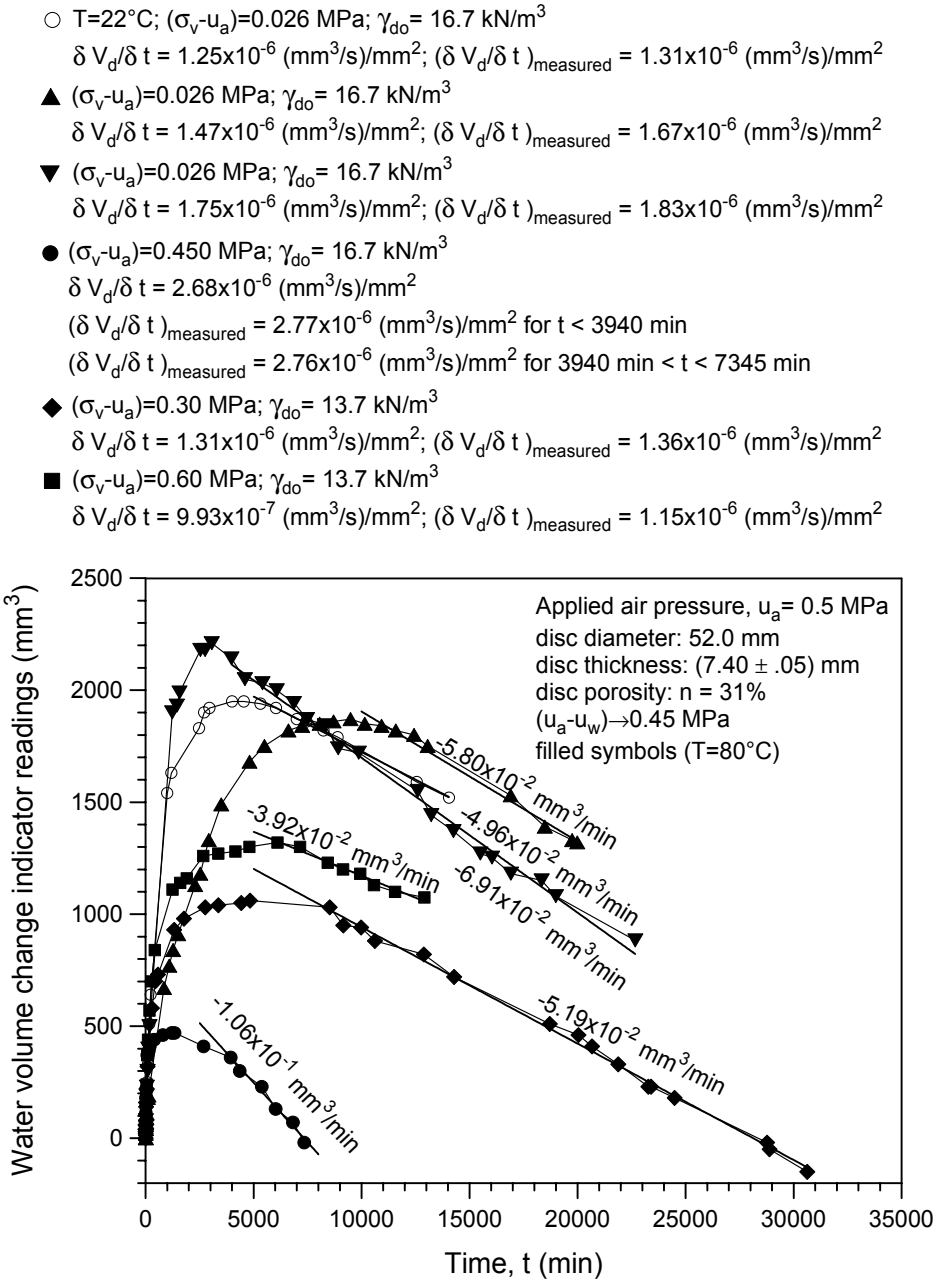

Figure 3.18 Water volume change under isothermal conditions. Comparison between directly measured values of diffused air volume and estimated from steady-state considerations.

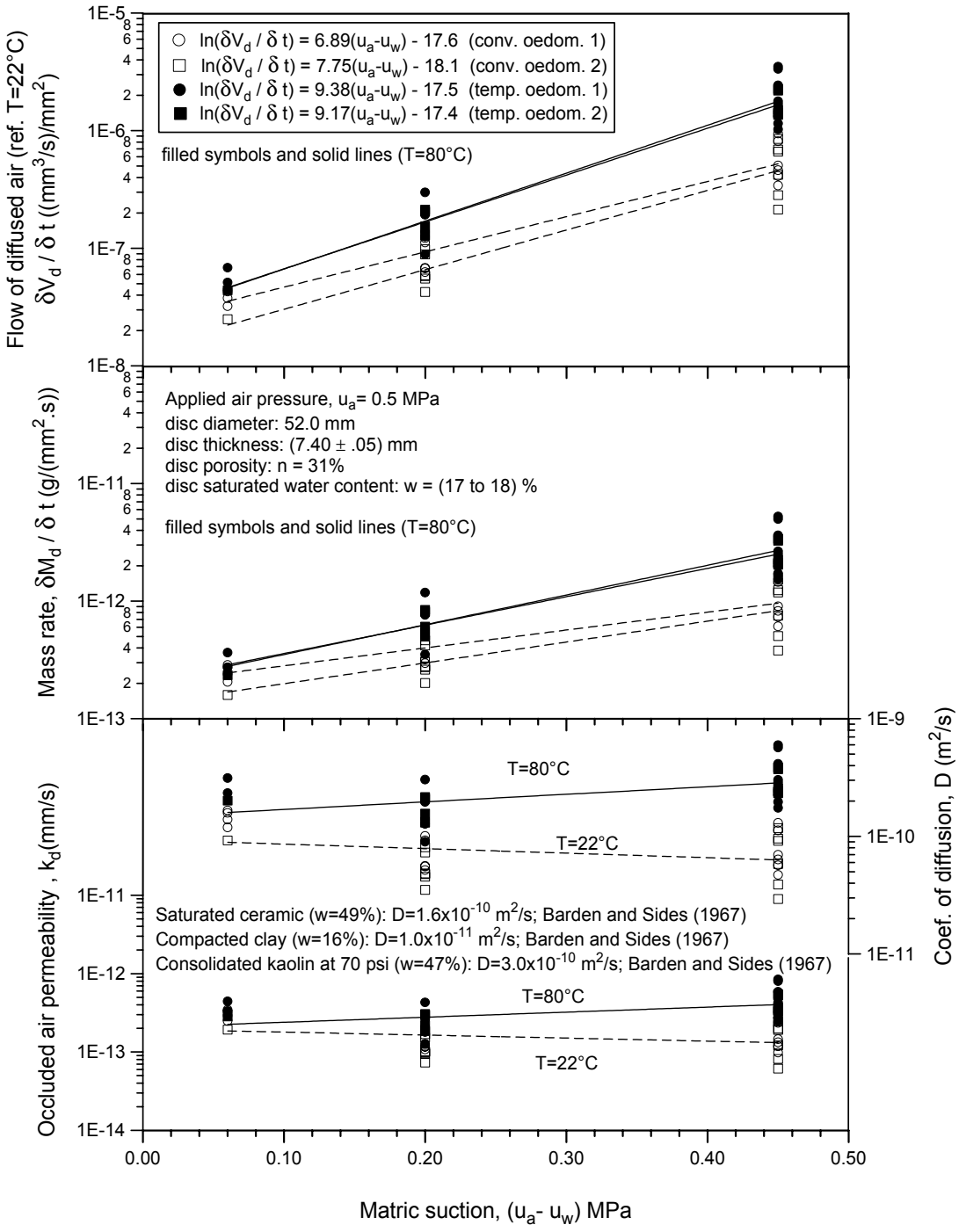

Figure 3.19 Amount of air diffusing through the ceramic discs for different matric suctions and temperatures.

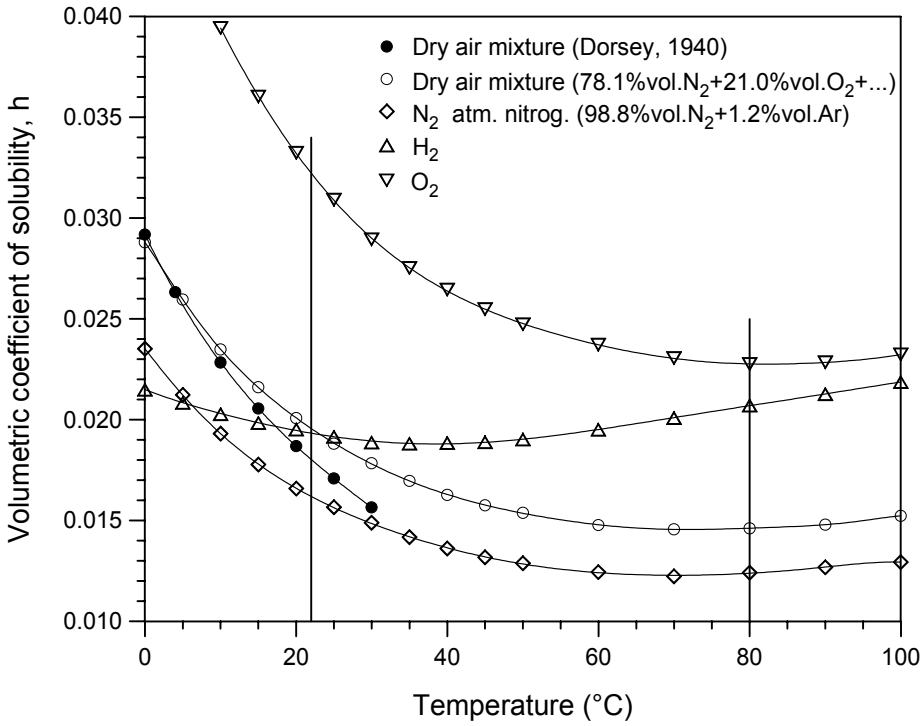

Figure 3.20 Volumetric solubility in water for different gases constituents of dry air.

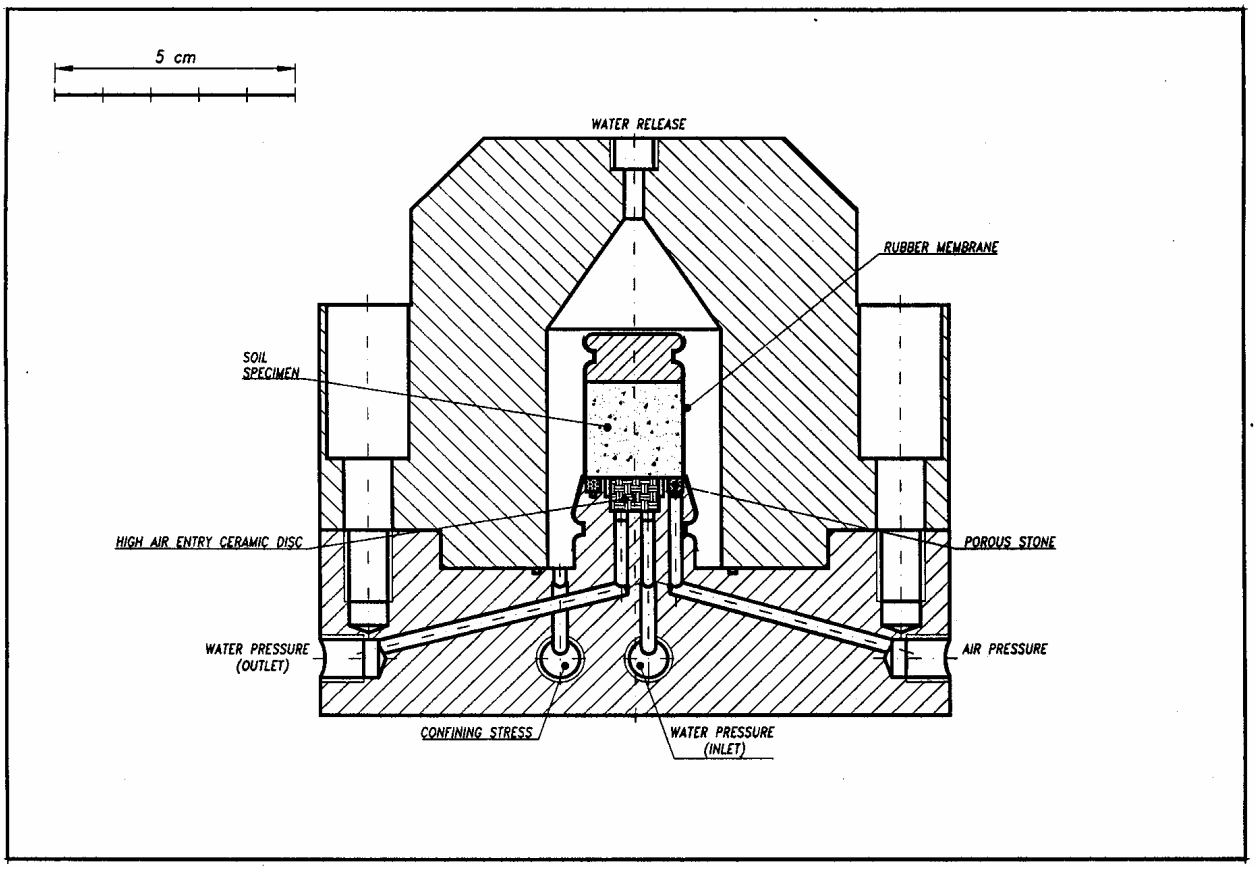

Figure 3.21 Basic scheme of the mini isotropic suction controlled cell.

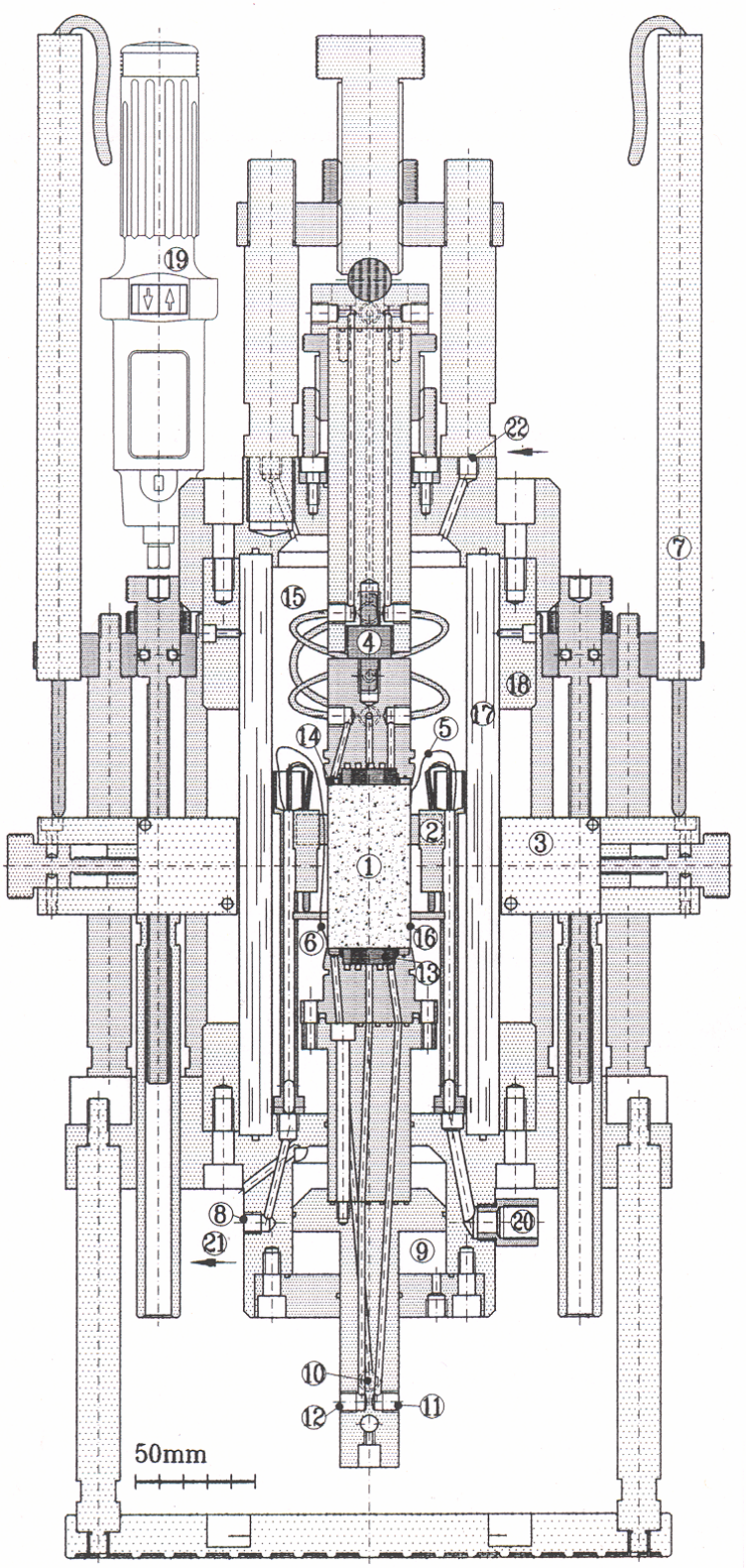

1) Specimen; 2) LVDT (axial strain); 3) Laser displacement sensor (radial strain); 4) Load cell or alignment device (isotropic test); 5) Top thermocoup1e (external heater control); 6) Bottom thermocoup1e (gear pump control); 7) LVDT (vertical displacement of 1aser sliding subjection); 8) Confining pressure; 9) Load pressure chamber (vertical stress); 10) Air pressure; 11) Water pressure (to vo1ume change measuring system); 12) Water pressure (to diffused air flushing system); 13) High air entry ceramic disc; 14) Coarse porous ring; 15) Confining fluid (silicone oil); 16) Silicone membrane; 17) Perspex wall; 18) Stee1 wall; 19) Vertical displacement e1ectric motor; 20) E1ectrical connections to transducers and data acquisition system; 21) Connection to forced convection system (gear pump); 22) Connection from forced convection system (heater).

Figure 3.22a Cross-section scheme of triaxial cell.

Figure 3.22b Picture of triaxial cell.

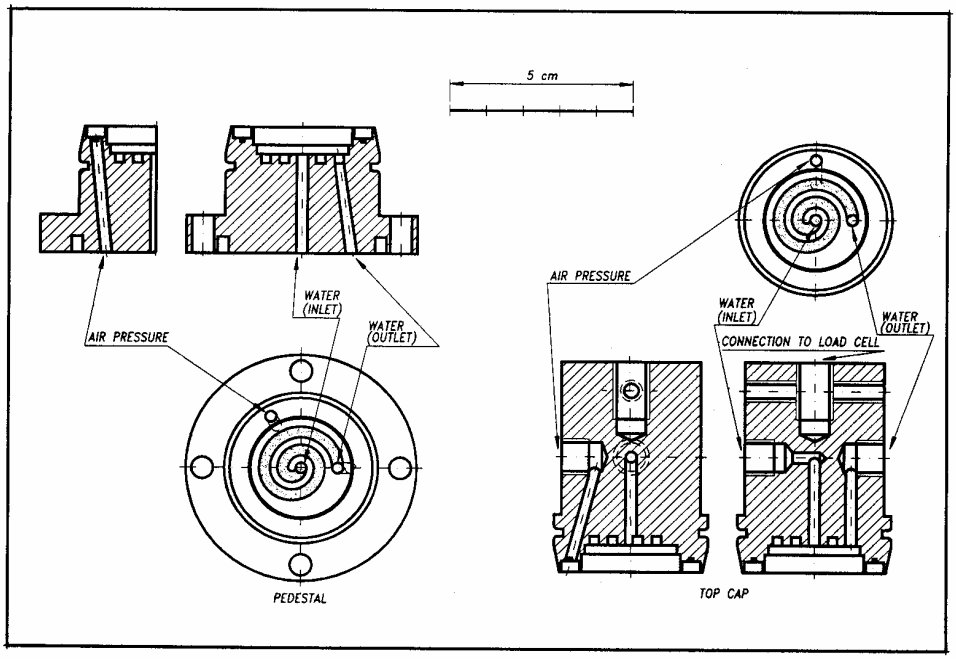

Figure 3.23 Top and base plate assembly of HAEV discs and coarse porous stones.

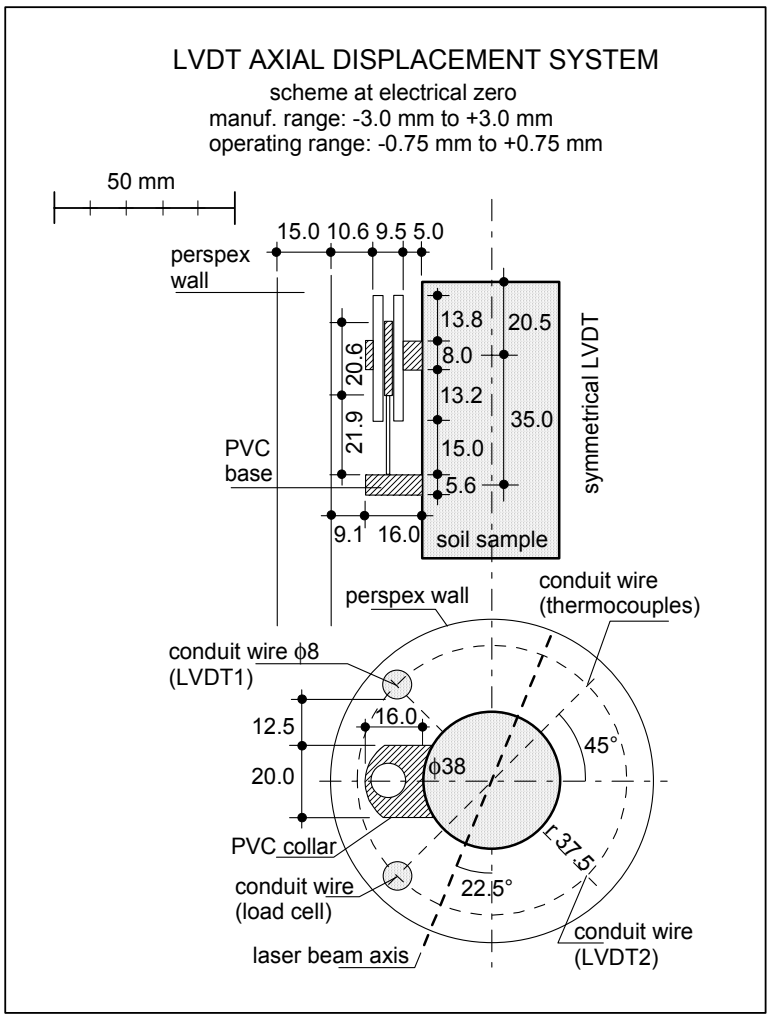

Figure 3.24 Mounting scheme of internal LVDTs.

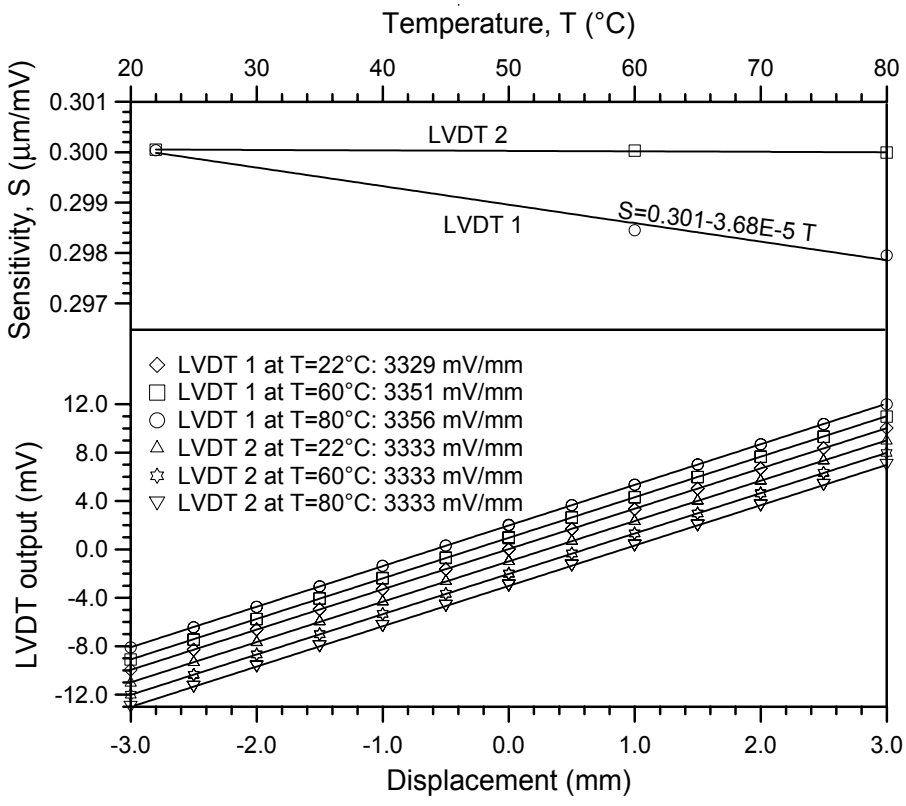

Figure 3.25 Calibration cycles of internal LVDTs at different temperatures.

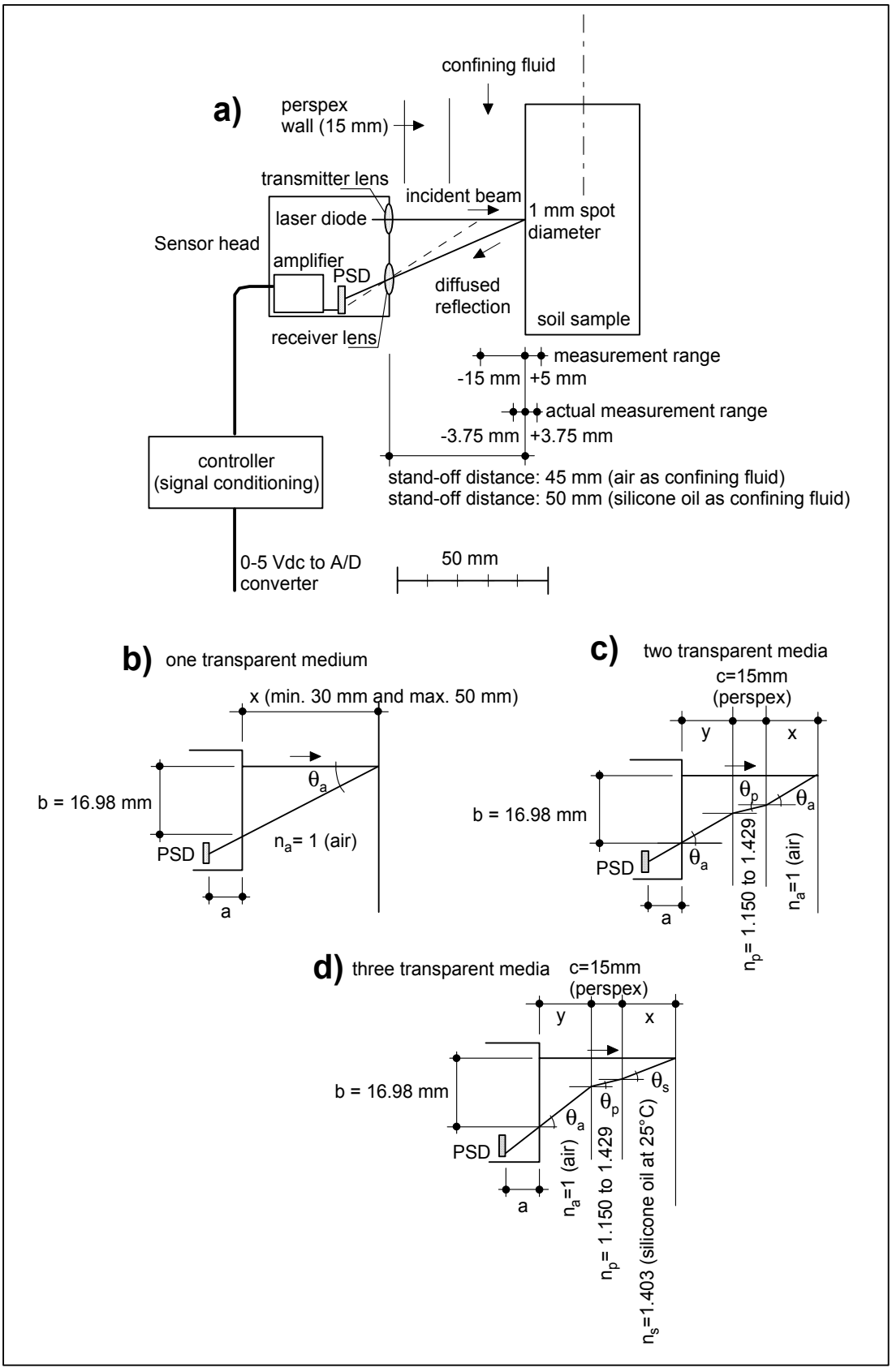

Figure 3.26 a) Lateral strain sensor head scheme and optical triangulation technique. b), c) and d) Refraction effects on sensor response.

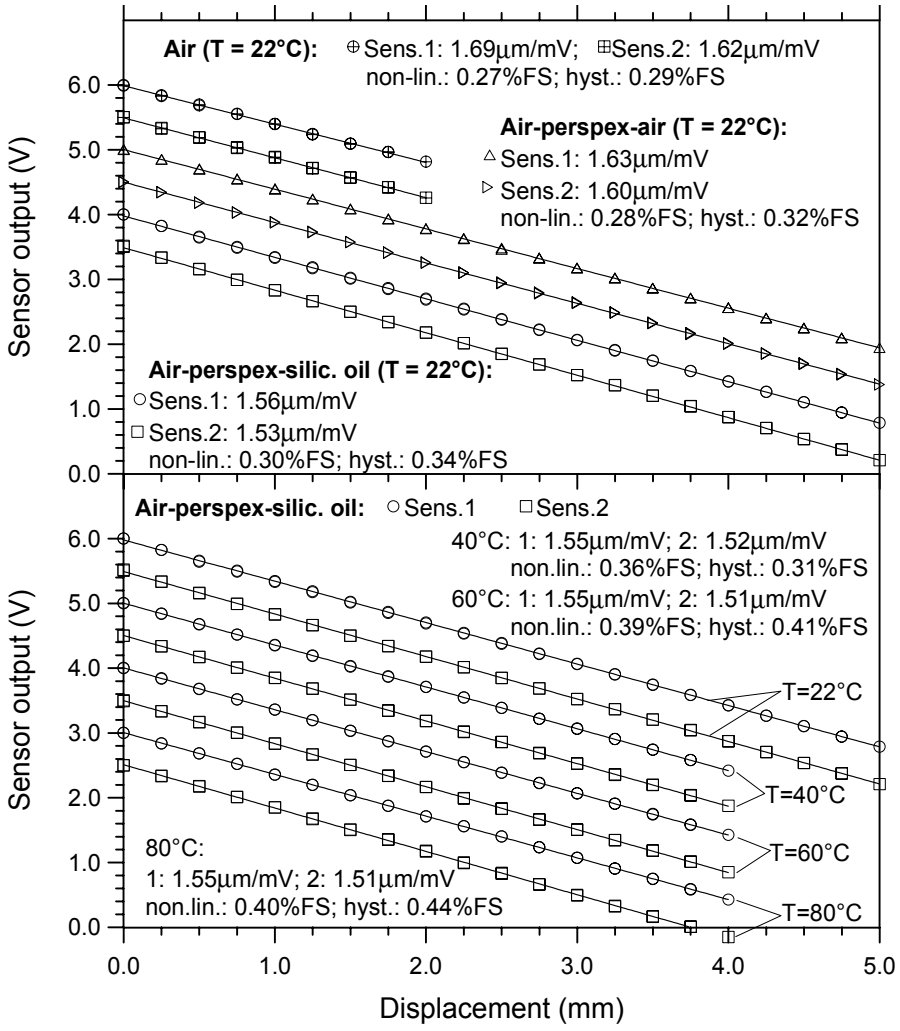

Figure 3.27 Output voltage and displacement calibration relationships of lateral strain sensor.

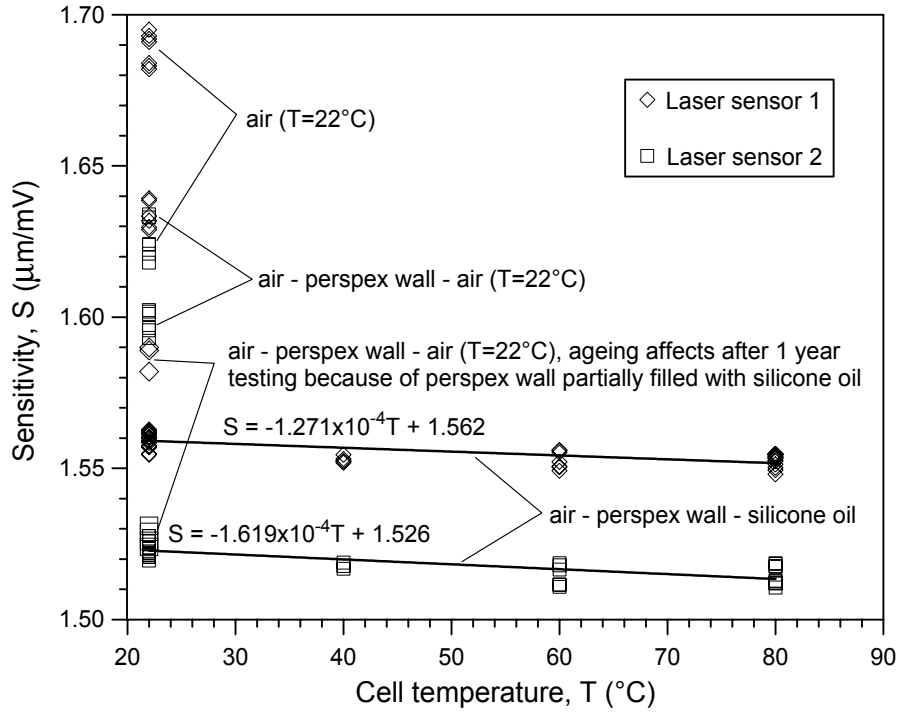

Figure 3.28 Sensitivity of the lateral strain sensor with different transparent media. Sensitivity shift for varying cell temperatures.

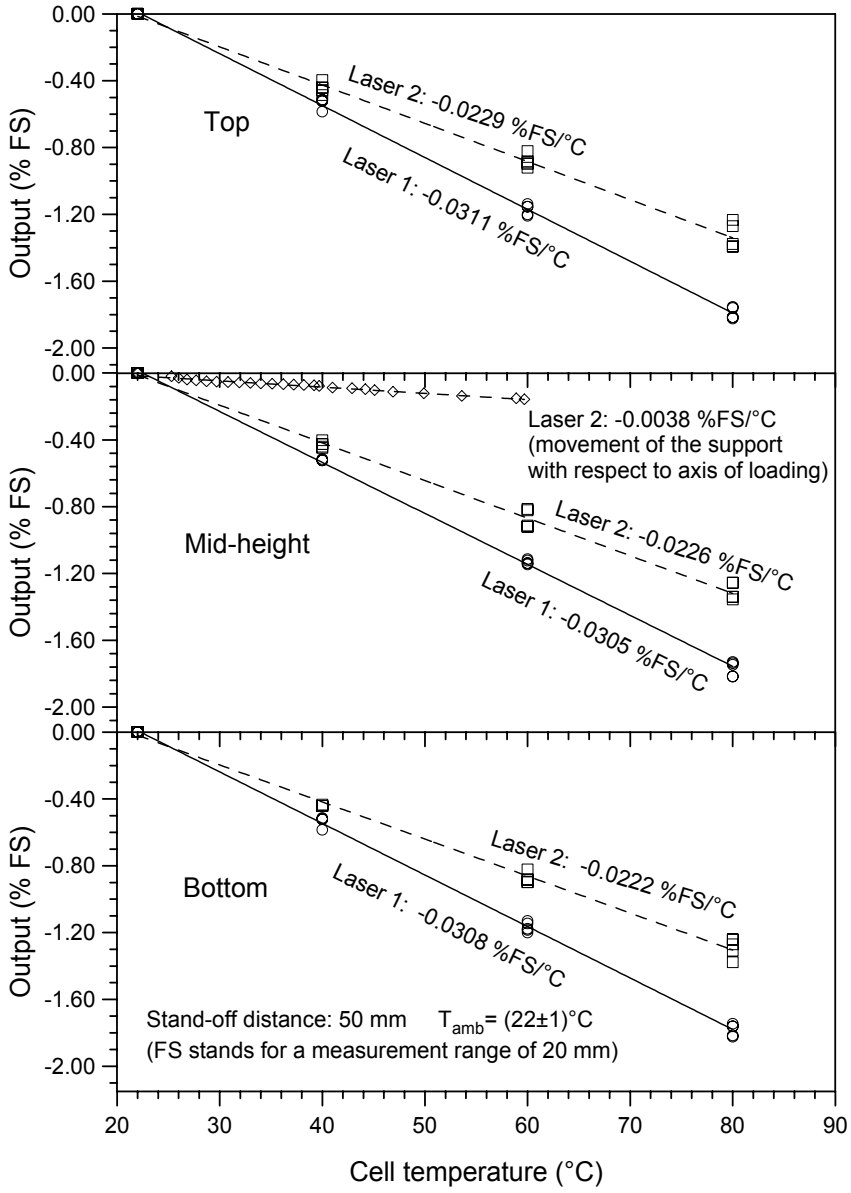

Figure 3.29 Calibration cycles of temperature effects on zero-shift of lateral strain sensors.

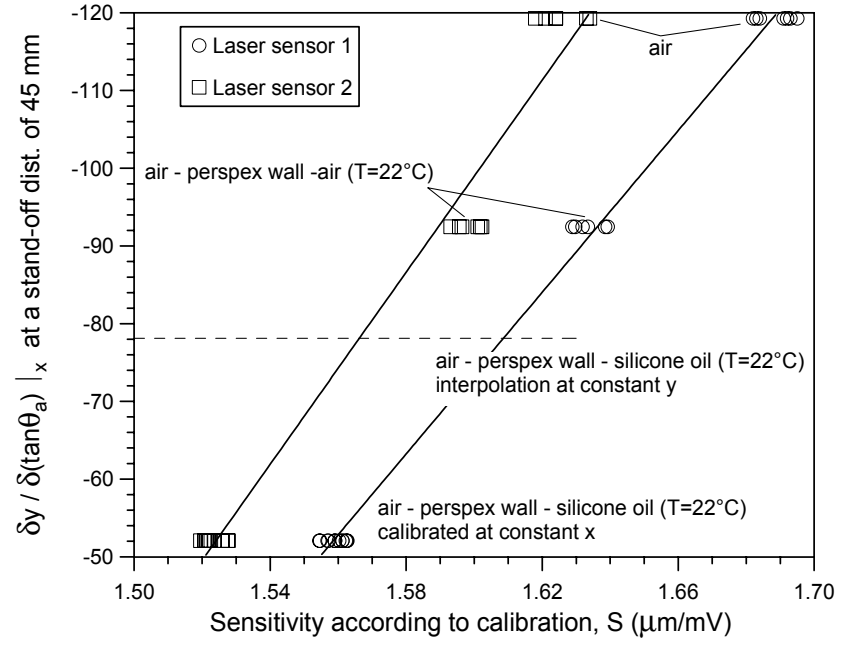

Figure 3.30 Comparison of theoretical and calibration sensitivities of lateral strain sensors.

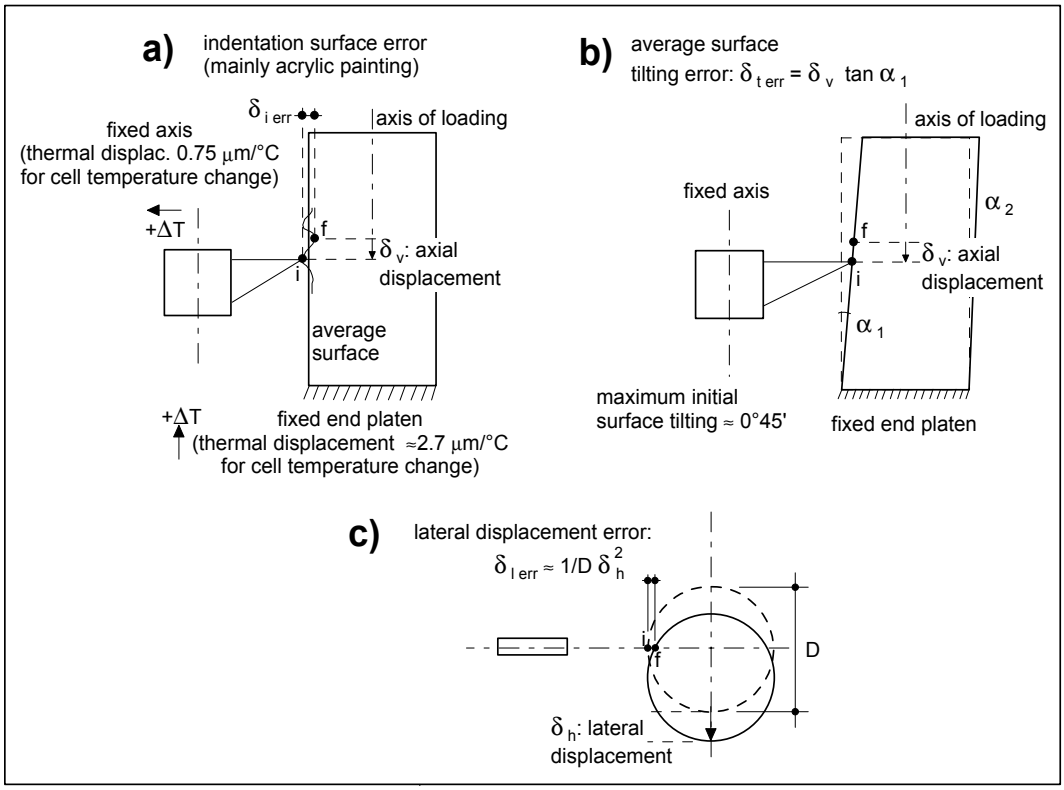

Figure 3.31 Sources of errors involved in the non-contact lateral strain measurement.

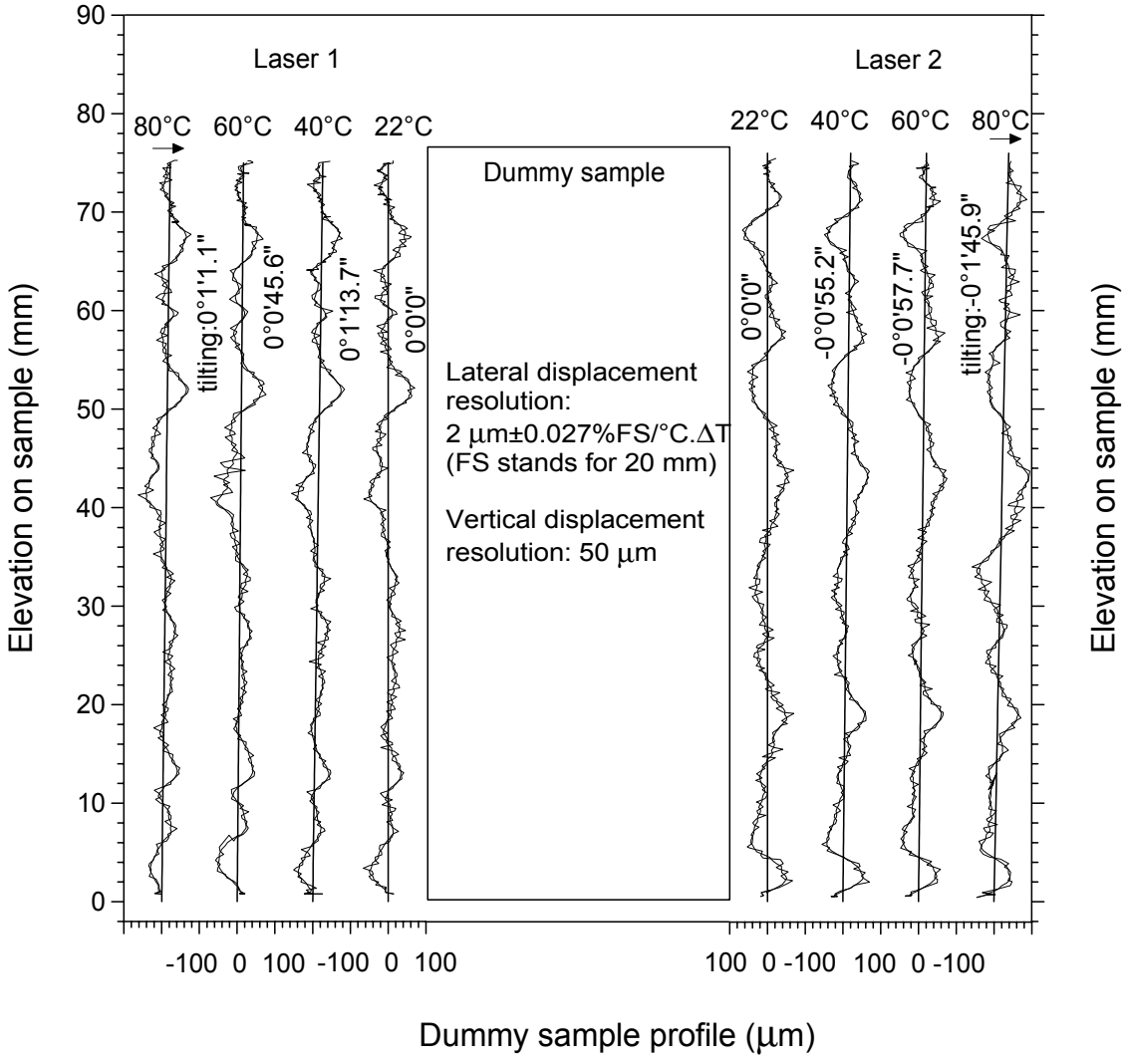

Figure 3.32 Performance of lateral strain sensors at different cell temperatures. Dummy sample profiles.

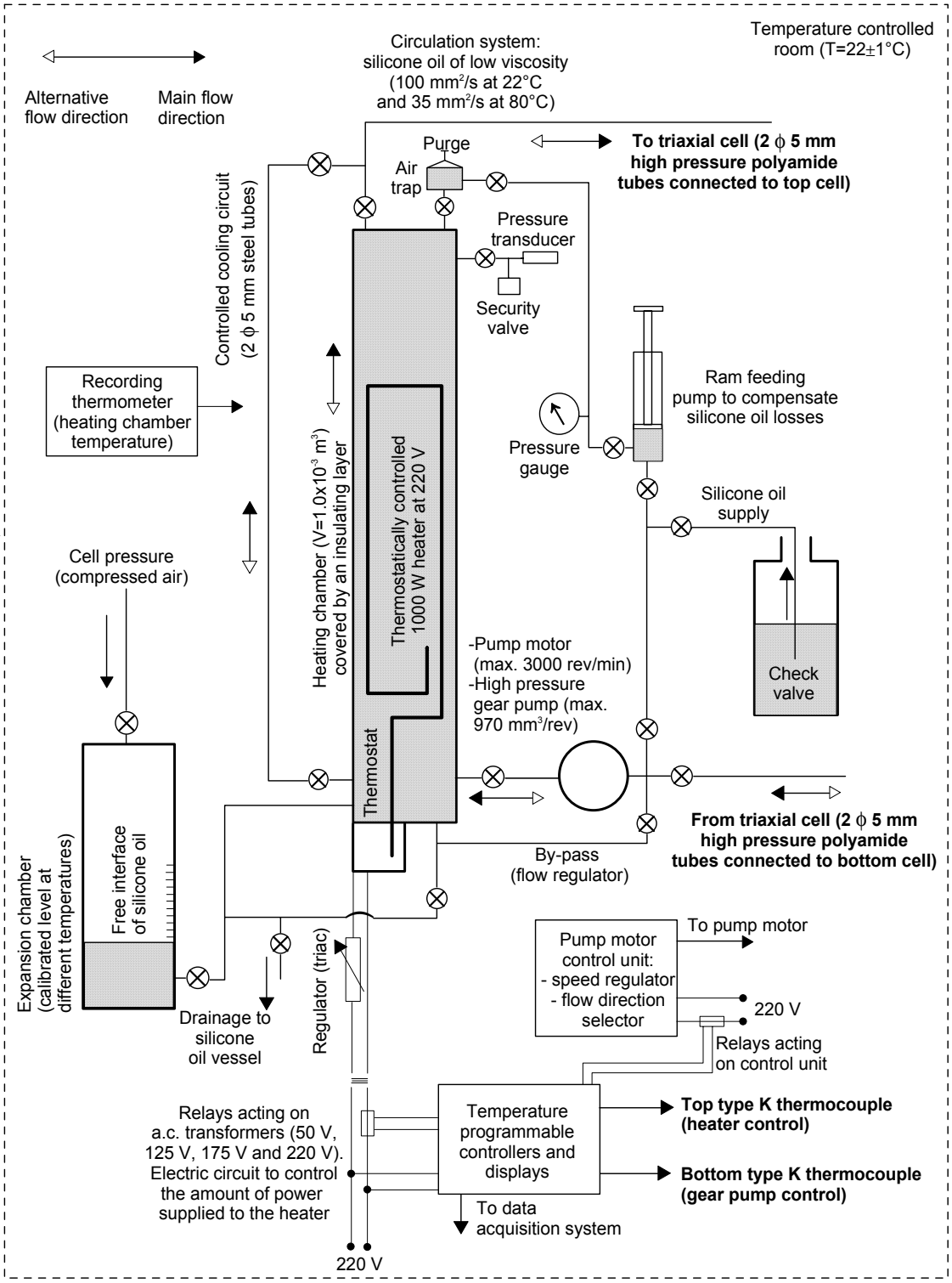

Figure 3.33 Scheme of the forced convection heating system.

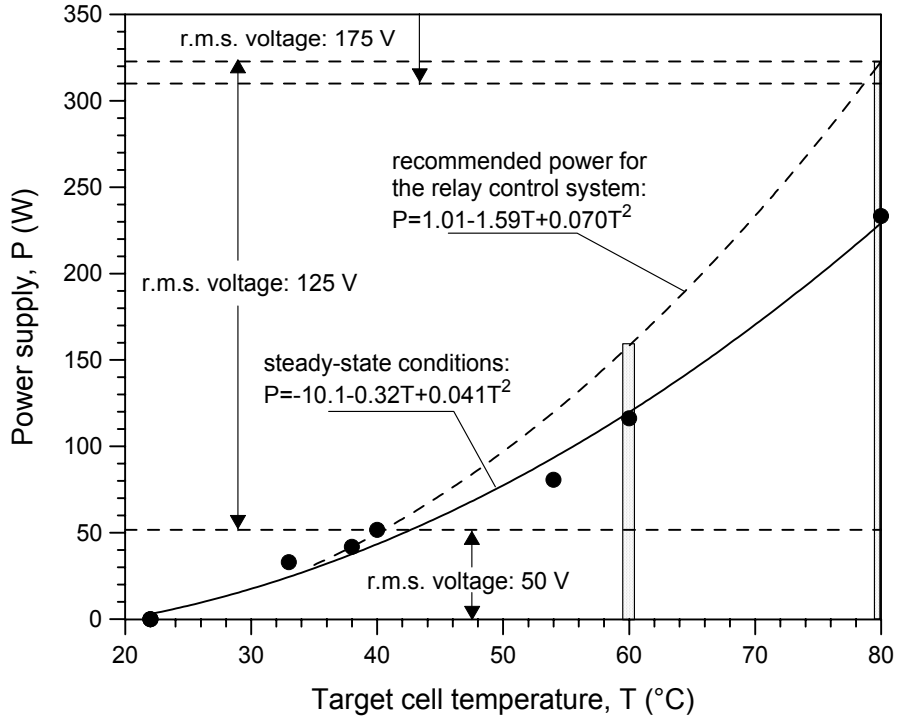

Figure 3.34 Power supplied to the external heater according to target cell temperatures.

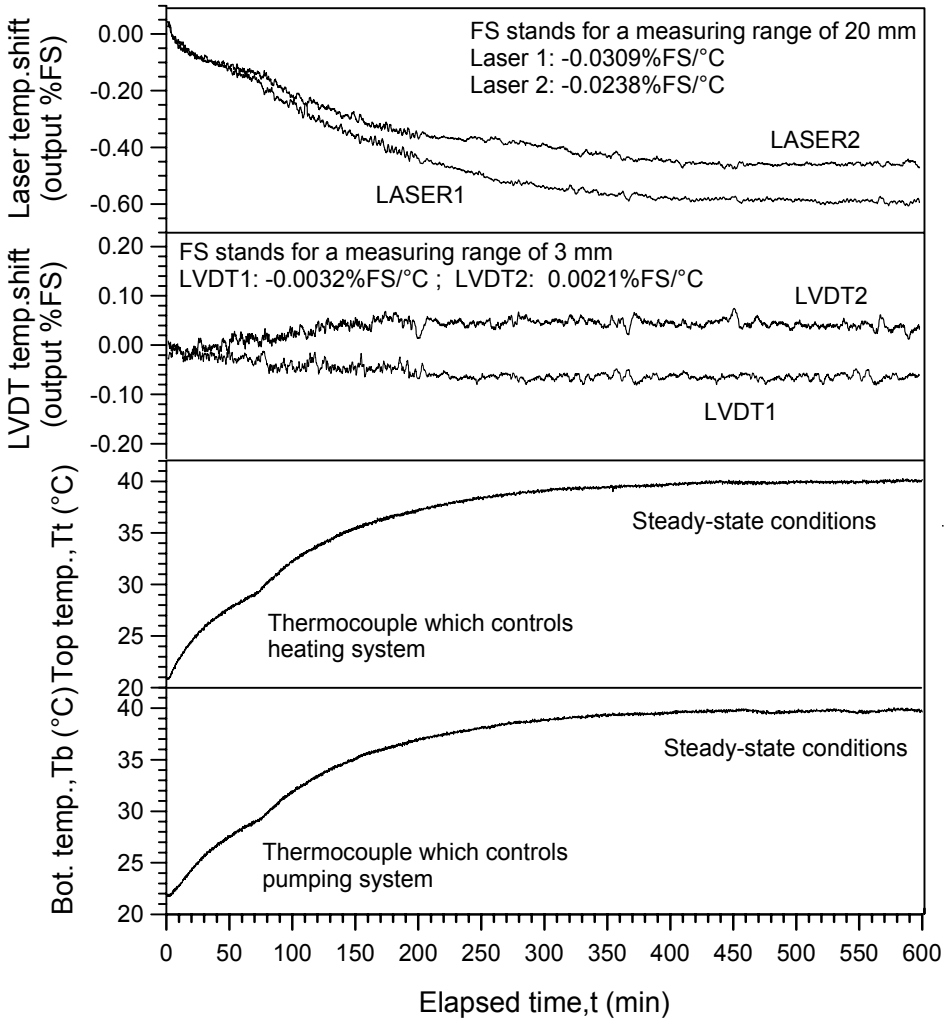

Figure 3.35 Temperature evolution and zero-shift of local sensors (22°C to 40°C).

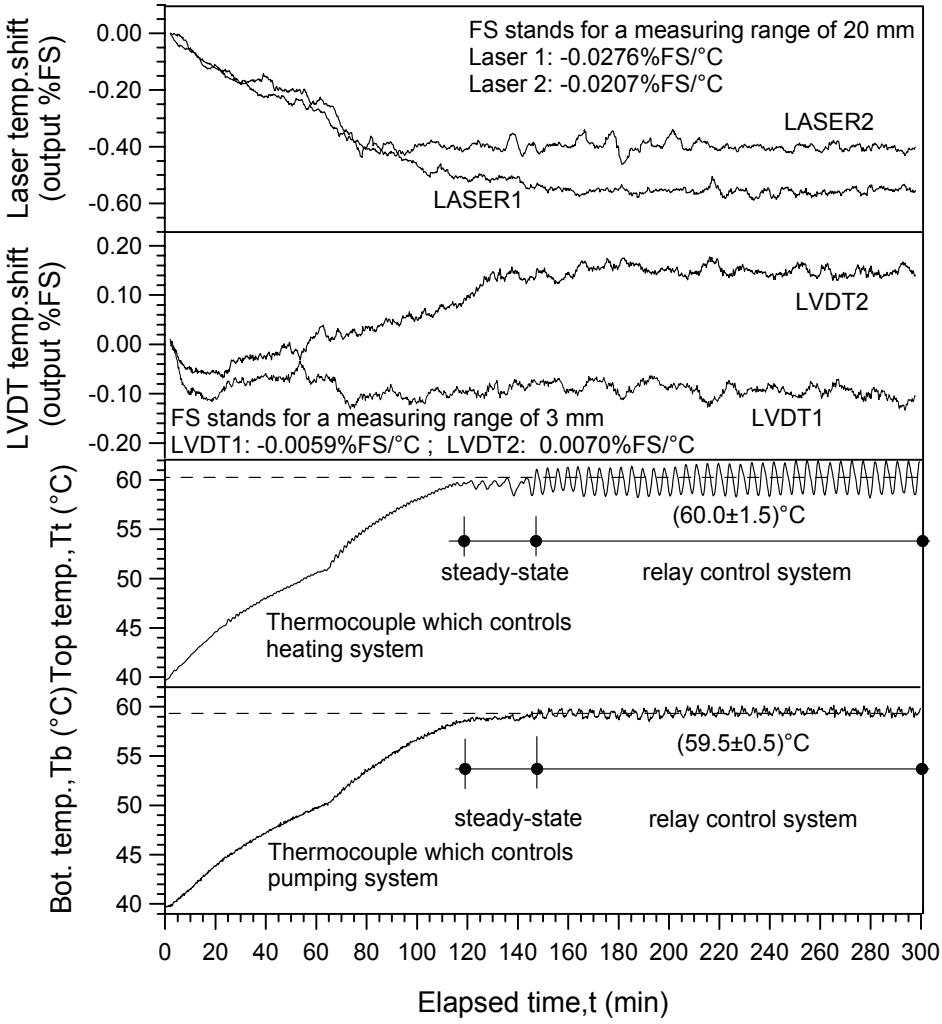

Figure 3.36 Temperature evolution and zero-shift of local sensors (40°C to 60°C).

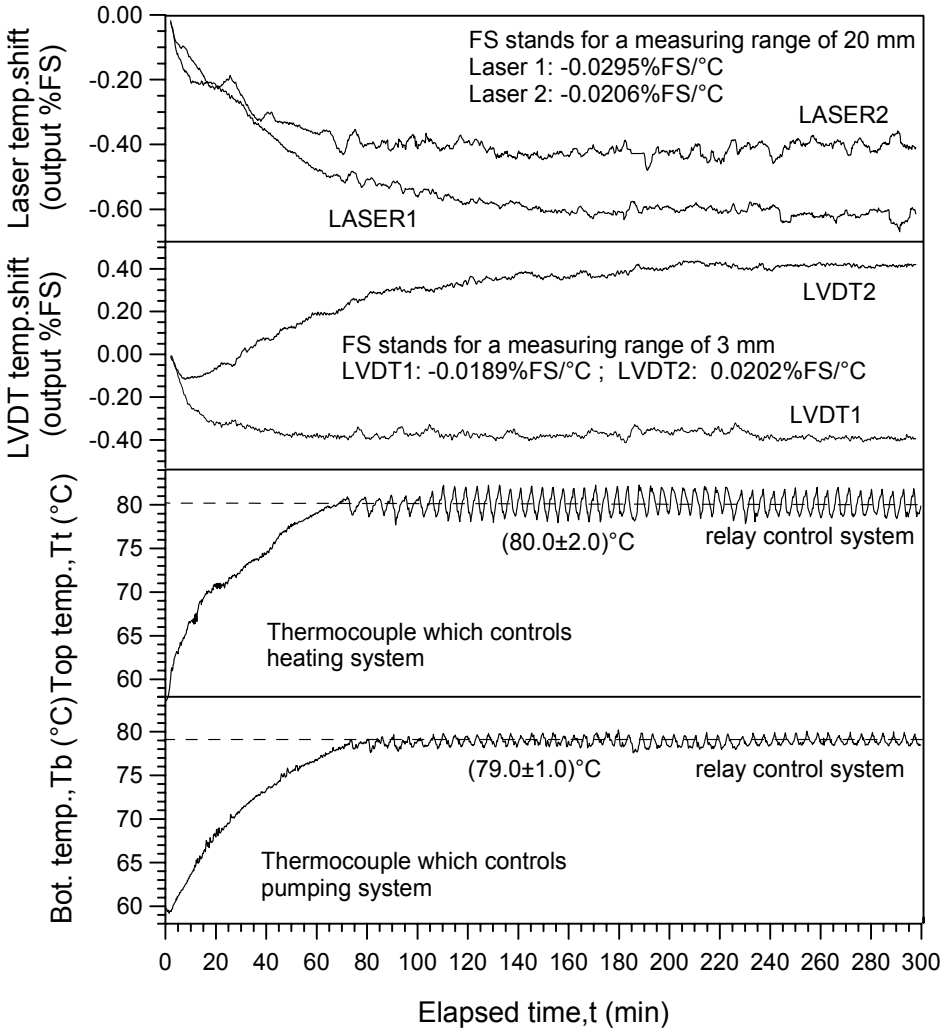

Figure 3.37 Temperature evolution and zero-shift of local sensors (60°C to 80°C).

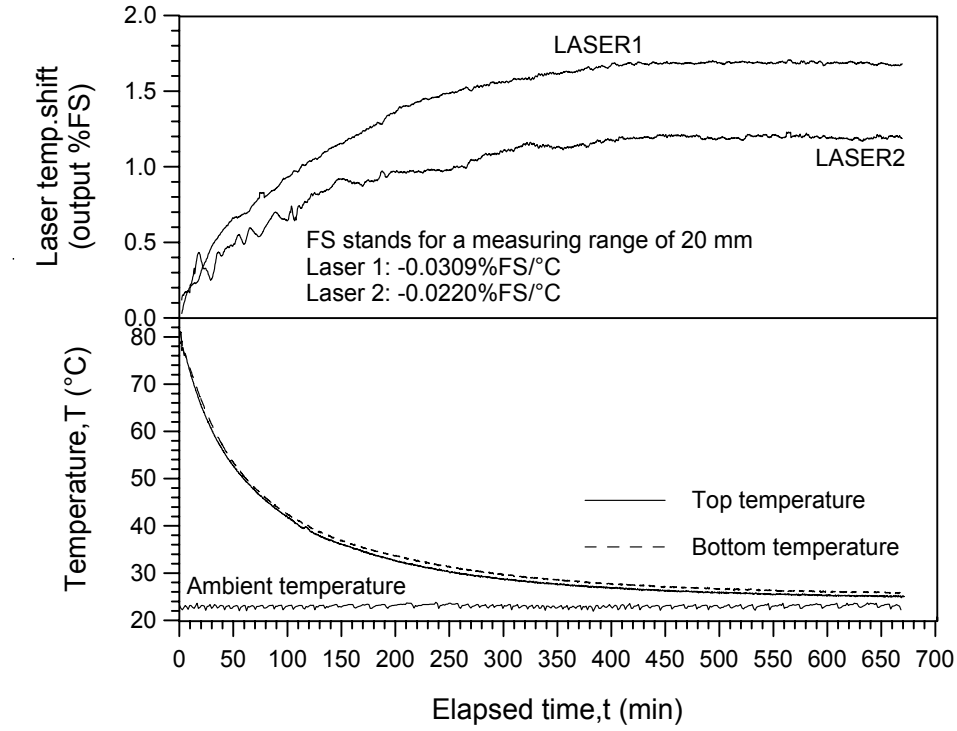

Figure 3.38 Cooling path and zero-shift on laser sensors (80°C to ambient temperature).